UNIVERSITY OF SÃO PAULO
ESCOLA POLITÉCNICA
POST-GRADUATION PROGRAM IN MECHANICAL ENGINEERING

DENIS RAMON DOS SANTOS PEIXOTO

CFD-based multi-objective aerodynamic optimization applies to car rear diffusers

São Paulo
2021

DENIS RAMON DOS SANTOS PEIXOTO

CFD-based multi-objective aerodynamic optimization applies to car rear diffusers

Revised Version

Dissertation presented to the Polytechnic School of the University of São Paulo as part of the requirements for obtaining the title of Master of Science in Engineering by the Post-graduate Program in Mechanical Engineering

Concentration Area: Energy and Fluids

Supervisor: Dr Bruno Souza Carmo

São Paulo
2021

Este exemplar foi revisado e corrigido em relação à versão original, sob responsabilidade única do autor e com a anuência de seu orientador.

São Paulo, ______ de ___________________ de __________

Assinatura do autor: _______________________

Assinatura do orientador: _______________________

Catalogação-na-publicação

Peixoto, Denis
CFD-based multi-objective aerodynamic optimization applies to car rear diffusers / D. Peixoto -- versão corr. -- São Paulo, 2021.
147 p.

Dissertação (Mestrado) - Escola Politécnica da Universidade de São Paulo. Departamento de Engenharia Mecânica.

1.Vehicle aerodynamics 2.Computational fluid dynamics I.Universidade de São Paulo. Escola Politécnica. Departamento de Engenharia Mecânica II.t.

Resumo.

Esta dissertação trata da otimização aerodinâmica da geometria de um carro com o objetivo de minimizar os coeficientes de arrasto e sustentação. O coeficiente de sustentação desempenha um importante papel nos carros de alto desempenho, como por exemplo carros de corrida, a fim de melhorar a força sustentação negativa, e consequentemente, maximizar a aderência do carro. Mais aderência pode proporcionar mais segurança quando se está dirigindo um carro e aumentar a aceleração lateral do carro nas curvas, o que é um fator que contribui decisivamente para a redução o tempo total da volta. Reduzindo o coeficiente de arrasto é possível atingir uma velocidade máxima mais alta, e melhorar a eficiência energética do carro.

O objetivo principal desta tese é otimizar a geometria do carro levando em conta o desempenho aerodinâmico através das simulações CFD. A proposta de otimização da geometria é a implementação de um difusor traseiro, por se tratar de um dispositivo aerodinâmico de alta eficiência. Devido ao efeito solo, o difusor traseiro pode gerar um grande aumento de força sustentação negativa sem penalidade excessiva de arrasto.

A pesquisa foi dividida em duas partes: Na primeira, todas as simulações foram feitas empregando o corpo de Ahmed, devido à sua simplicidade e características do escoamento. O corpo Ahmed foi usado como uma referência para validar a metodologia de simulação numérica, através da comparação com resultados experimentais disponíveis na literatura, e para desenvolver todo o processo de otimização. A segunda parte foi baseada na geometria de um carro usando as mesmas técnicas aplicadas no estudo do corpo de Ahmed.

A partir dos estudos realizados foi feito um loop de otimização integrando a Otimização Multi-Objetivo (MOO) com Simulações CFD para obter a melhor geometria a partir de um processo automatizado e confiável.

Palavra-chave: Aerodinâmica, CFD, Arrasto, Sustentação, Otimização Multiobjetivo.

Abstract.

This dissertation covers the aerodynamic optimization of a car geometry to minimize drag and lift coefficients. The lift coefficient plays an essential role in high-performance cars like race cars to improve the overall downforce and consequently maximize the car grip. More grip can provide more safety during car handling and increase the lateral acceleration of the vehicle during the corners, which is a factor that contributes decisively to reduce the overall lap time. By reducing the drag coefficient it is possible to achieve higher top speed and improve the car's fuel efficiency.

The main objective of this thesis is to optimize the car geometry with respect to the aerodynamic performance through the CFD simulations. The geometry optimization entails the implementation of a rear diffuser because it is a highly efficient aerodynamic device. Due to the ground effect, the rear diffuser can generate a high downforce level without a substantial drag penalty.

The research was divided into two parts. In the first one, simulations were performed using the Ahmed body model due to its simplicity and flow features. The Ahmed body was used as a benchmark to validate the numerical modeling and simulation methodology by comparing them with experimental results in the literature and developing all the optimization processes. The second part was based on a car geometry using the same techniques applied in the Ahmed body study.

An optimization loop was built from the studies performed, integrating the Multi-Objective Optimization (MOO) with CFD simulations to obtain the best geometry through an automated and reliable process.

Keywords: Vehicle aerodynamics, Computational fluid dynamics, Drag, Lift, Multi-Objective Optimization

Figure list

Tables list

List of Symbols

C_D	Drag coefficient
C_L	Lift coefficient
τ_{ij}	Stress tensor
ρ	Density
P	Static pressure
V	Flow velocity
v	Kinematic viscosity
v	Velocity in y-direction
u	Velocity in x-direction
w	Velocity in z-direction
U_∞	Freestream velocity
Re	Reynolds number
U_{min}	Minimum u velocity in wake
x, y, z	Coordinates
α	Angle of attack
μ	Molecular dynamic viscosity
ε	Dissipation rate of the kinetic energy
ω	Specific turbulent dissipation
k	Specific turbulence kinetic energy
S	Reference area
F_2	Force
R	Gas constant
σ_k	Tensor
g	Gravity
r	Refinement ratio for
p	Order of convergence
$f_{1,2,3}$	Results of the simulation
$f_{h=0}$	Result of interest at zero grid spacing
GCI_{12}	Grid convergence index for grids 1 and 2
GCI_{23}	Grid convergence index for grids 2 and 3
FS	Factor of safety

Contents

1 Introduction

1.1 Background

The study of the flow around a car is primarily concerned with the forces that the flow exerts on the body, that is, the lift, drag and side forces. The purpose of studying this flow during the automotive design process is to reduce the drag force and lift force, which are important for handling characteristics. Other factors affecting the external aerodynamics must also be considered, such as the requirements for cooling of the engine, transmission and brakes (Gillieron, 1999); the flow within the passenger compartment area; and the prevention of dirt build-up on the windows of the automobile (Raghu, 1999). These considerations, however, are more important to passenger cars. An additional branch of external automotive aerodynamics covers racing vehicles. Here, the main concern is to provide a large amount of downforce (negative lift) while not generating excessive drag.

The flow features around both passenger and racing cars are very complex, there are large regions of transition, separated flow, vortex and wake formation. Allowing considerations of such complex flow characteristics to be integrated into the design of a new vehicle requires the understanding of, and the ability to predict, the flow field early in the development program. This can be done using a variety of methods: wind tunnel or water tank tests using scale models, or Computational Fluid Dynamics (CFD). Scale models were expensive to build, in both time and cost, but recently, with the evolution of the 3d printing technology, the cost and prototyping time have become much smaller. The initial costs involved in building a wind tunnel are considerable and once built, they still require upkeep and maintenance costs. By contrast CFD requires a smaller initial financial outlay and, with the increasingly widespread use of CAD models, involves less work, time, and cost to produce a flow analysis for each vehicle. However, CFD is not simple to use and there are several problems like high computational cost, CAD model accuracy, turbulent models and boundary conditions, that can prevent engineers from using it as a reliable tool to develop new automobiles.

The main role of the aerodynamics applied to race cars is to generate a substantial level of downforce causing the minimum drag. In addition, the aerodynamic balance (relationship between front and rear axle downforce) is very important considering all speed conditions. The complex flow features associated to individual components are intertwined and difficult to separate. Therefore, a clear understanding of the physics of the flow associated to the aerodynamic components is a prerequisite to obtain a global understanding of the flow, and eventually a better vehicle geometry.

Race cars have many components that provide better aerodynamic performance for the vehicle, like inverted wings, diffuser, and vortex generators, each one with a specific feature. The components that are more efficient are those which generate ground effect and provide less drag. While drag reduction is a very important research field, the downforce generation also has an important role in lap time reduction, security and race car balance.

The main techniques to evaluate the aerodynamic performance a car are wind tunnel tests, track tests and computational fluid dynamics (CFD) simulations. The main difference between a CFD study and the other two techniques is that CFD does not require a real vehicle model. It consists in numerical simulations using a virtual model that reproduces the vehicle geometry and the flow conditions.

Numerical simulations have been widely used in the performance prediction because it has relatively low costs and does not need a real car model, so it can be used more easily during the design phase. However, a race car has a very complex geometry. So much physical insight can be gained by using a simplified vehicle geometry, like that proposed by Ahmed (1984), before using more realistic designs.

1.1.1 Downforce generation

The aerodynamic designer has two primary concerns. The first is the creation of the downforce in order to push the car's tyres onto the track and improve the cornering performance. The second is to minimise the drag caused which acts to slow the car down. The two main components of the racing car that can be used to create downforce when the car is travelling at racing speed are the shape of the body and the use of the aerofoils.

Downforce is referred to as "aerodynamic grip" and is distinguished from the "mechanical grip", which is a function of the car mass repartition, tyres and suspension. The shape of the body and reversed wings usually generate downforce. In the experiments of Zerihan and Zhang (2001), it was shown that the front wing generated around 25-30% of the total downforce of the race car, while the shape of the body with other components, such as the rear wing and the diffuser, created the rest of it.

Race car wings are basically inverted aircraft wings, so the physical principle that generates lift force is the same in both cases. Air flows at different speeds over the two sides of the wing and this creates a difference in pressure, a physical rule known as Bernoulli's Principle.

As this pressure tries to balance, the wing tries to move in the direction of the low pressure. The handling aspect was particularly important because by controlling the downforce distribution between the front and rear wheels, the vehicle stability could be altered (e.g., by relying on the tyres' increased performance rather than on aerodynamic effects of large stabilizing fins). Consequently, the improved cornering due to the use of aerodynamic downforce led to the dramatic increase in cornering speeds from the 1960s to the mid-1990s, as shown in Figure 1-1**.** In those years, cornering acceleration grew from less than the gravitational acceleration (*g*) to close to 4*g* due to the increased use of aerodynamic downforce (Katz, 2016).

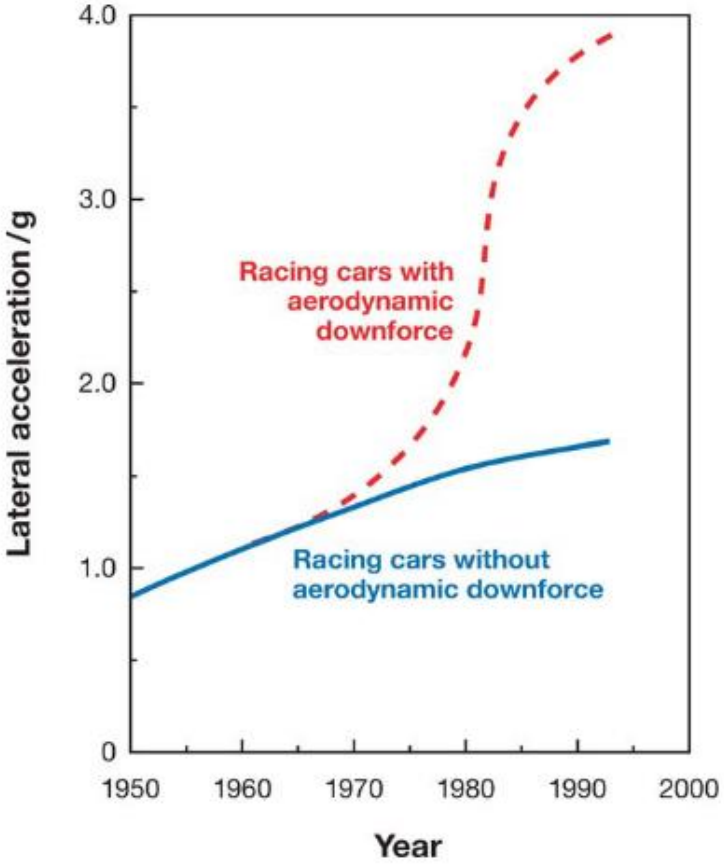

Figure 1-1Trends in maximum cornering acceleration during the past 50 years (Katz, 2006).

1.1.2 Ground effect

The ground effect started to be investigated originally because of the claims from pilots that in approaching the ground, a cushioning effect was observed. An early test (Zahm and Bear, 1921) using a fixed ground on a RAF6 aerofoil demonstrated that the presence of the ground makes the lift increases and the drag reduces for a given angle of attack. Other early tests (Raymond, 1921) also showed that lift slope increases can be expected. In addition, it is believed that the pressure on the pressure surface increases due to the image beneath the ground plane inducing a lower velocity in that region (Screbrinsky and Biachuev, 1946). Therefore, the lift of a wing increases when the wing is approaching to the ground. This effect works well for both airplane wings which generate lift and inverted wings which create downforce. Until very recently, however, studies of downforce which is produced by wings in ground effect were very much incomplete. Dominy (1992) firstly presented a short description of the aerodynamics of a wing close to the ground. He pointed out that the ground effect was effectively constraining the flow over the suction surface, hence generating an increase in suction. Dominy (1992) hypothesised that, in close proximity to the ground, the wing would stall due to the boundary layer separation because of the large suction and the related adverse pressure gradient. To increase the downforce, the basic idea is to create an area of low pressure underneath the car. Racing car designers have achieved low pressure by designing the underside of the car so that incoming air is accelerated through a narrow slot between the car and the ground to get lower pressure according to Bernoulli's principle. The first car which started the ground effect revolution in Formula One was the Lotus 78 “wing car” used in the 1977 and 1978 seasons (Nye and Doug, 1985). P. Wright (2001), one of the designers of this car, set about experimenting with F1 car body shapes using a wind tunnel and a rolling road, when accidently he began to get remarkable results in one of the models. Closer inspection showed that as the rolling road's speed increased, the shaped underbody was being drawn closer to the surface of the road. Wright tested with pieces of cardboard attached to the side of the model car body, and the level of perceived downforce produced was phenomenal. Figure 1-2 shows a schematic of those tests.

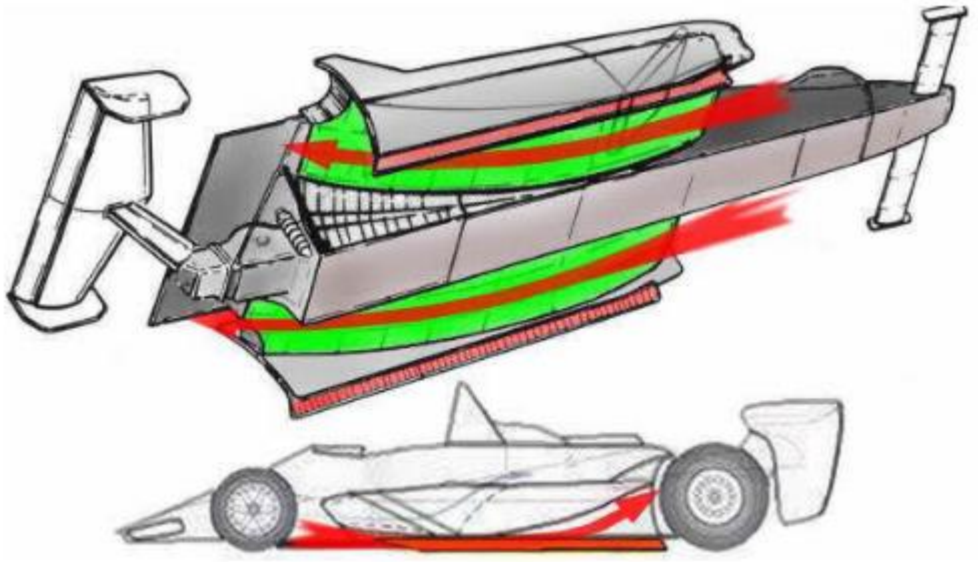

Figure 1-2 The ground effect Lotus 78 is shown. The side floors of the car can be seen acting like another rear wing (Liang, Chen, 2009).

1.1.3 Performance Cars Aerodynamic Devices

A good way to optimize the aerodynamic performance of a car is to use aerodynamic devices. If properly adapted to vehicles, aerodynamic add-on devices can provide more downforce and keep drag low, bringing benefits like fuel economy, stability in high speeds, or achieving greater performance. In this section, the operating principles behind some aerodynamic devices are briefly covered.

Front Wing

Front wings are exclusive of open-wheel single-seat race cars and are one of the most iconic complex parts of a F1 race car as they can generate a large amount of downforce, substantially increasing the grip of the front tires. They influence the airflow around the full length of the car and small changes on them can have huge impact on the overall performance. They are designed to function properly with clean undisturbed air and operate within strong ground effect due to its proximity to the surface of the track (Katz, 2006). Despite the increase of downforce with the ground proximity, as (Zerihan and Zang, 2001) showed in Figure 1-3, this effect has also undesirable consequences as a similar increase in drag was also experimentally measured.

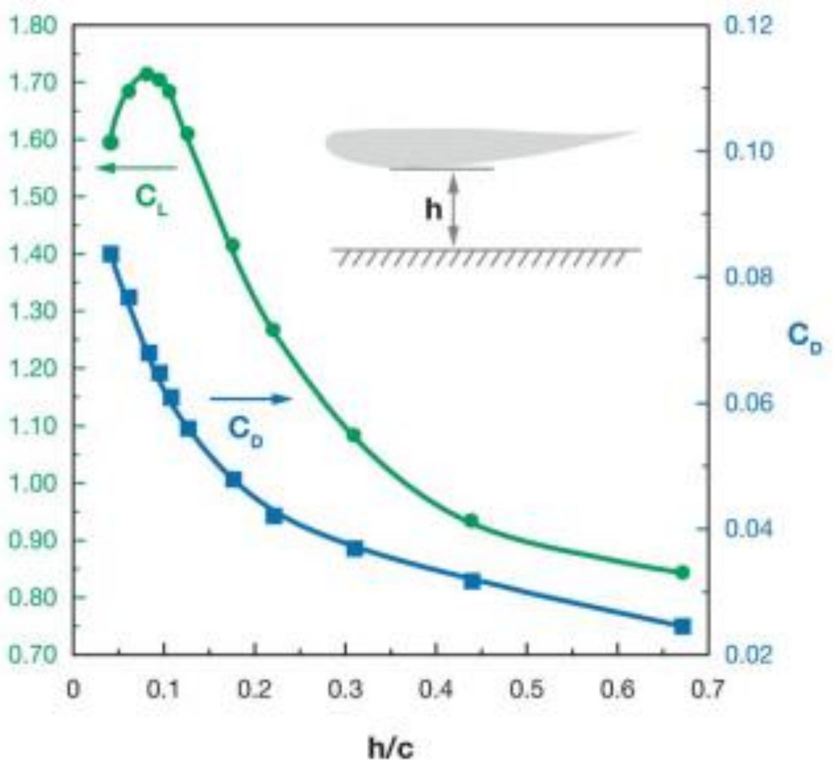

Figure 1-3 Downforce and drag coefficient versus ground clearance for an inverted LS(1)-0413 airfoil (Zerihan and Zang, 2001). [h: ground clearance, c: chord, $\alpha = -1 \circ$, $Re = 2 \times 10^6$, moving ground plane.]

Because of the very close proximity to the ground and the large magnitude of this effect, numerous studies have been focusing on this subject and the type of boundary conditions on the ground strongly affects both numerical and experimental results (Katz, 2006). Studies concluded that moving ground simulation is essential for such cases (Wiedemann, 1989). (Coulliette and Plotkin, 1995) Summarised the two-dimensional effects, including individual contributions of parameters such as thickness, camber, and the lift-to-angle of attack ratio of the aerofoil. Applying their studies for an inverted aerofoil, the positive effect of angle of attack and camber increases the downforce near the ground (Katz, 2006). (Katz, 1985) Also reported three-dimensional ground effect for finite-span rectangular wings and established that even in case of low aspect ratio (around 2) rectangular wings, this effect remains large.

Front Splitter and air dam combination

An air dam is usually a shaped part of the lower portion of the front bumper. It is sometimes called a "front lip" or "lip spoiler". It can be moulded as part of the front bumper, or it can be a separate part that is attached at the front-lower portion of the front bumper. Unlike the splitter, the lip is not a flat "sheet" of material. The functions of both are the same: to create lower and higher pressure on specific areas, but in case of air dam, in a less extreme way.

Figure 1-4 Race car air dam (http://www.formula1-dictionary.net/splitter.html).

The main purpose of an air-dam is to reduce the static pressure under the front of the car, blocking off the free-flow air that would otherwise enter beneath it. The efficiency of an air-dam can be further increased by using a horizontal extension at its bottom, called splitter. By trapping high static pressure air above it, and redirecting air away from this stagnation point, accelerating air below it to the underneath of the car, a downwards pressure differential is generated, thus creating downforce.

Canards and Dive Planes

Depending on the design intent, canards and dive planes have many different shapes. The standard canard is a small triangular flat or wing shaped wedge on the side of a car front bumper with the purposes of modifying the aerodynamic characteristics of the airflow through the length of the car. By redirecting the oncoming air’s momentum upwards, a downward reaction force is generated besides deflecting air away from the wheel, which is a place of high drag.

Figure 1-5 Race car dive planes (https://www.verus-engineering.com).

Vehicle’s under-body

The under-body of a typical passenger vehicle is one of the main sources of drag and lift forces due to the interference of airflow over exposed components such as the exhaust system, transmission, and drive shafts. On racing and performance cars, the flow under the vehicle must be considered and it is one of the secret weapons in an arsenal of aerodynamic features for generating downforce. Streamlining the under-body to generate lower pressures is one option, another is to create low pressure under the car by effects not directly related to the basic wing in ground effect model (Katz, 2006).

Sliding seals and skirts

One effective method to generate or maintain lower pressures under the car body is sealing the gap between the ground and the car, leaving only the rear portion open in a way that the low base pressure in this region will regulate the pressure under the car (Katz, 2006). In the past, two body concepts, the inverted wing (Figure 1-6) and the vacuum cleaner 1970 Chaparral 2J racing car (Figure 1-7), incorporated such seals, called by the generic name ‘skirts’, to prevent the airflow from penetrating the low-pressure area under the car, so maintaining a quasi-two-dimensional airflow there, generating very large lift-to-drag ratios. These devices have been banned by FIA (International Automobile Federation) due accidents.

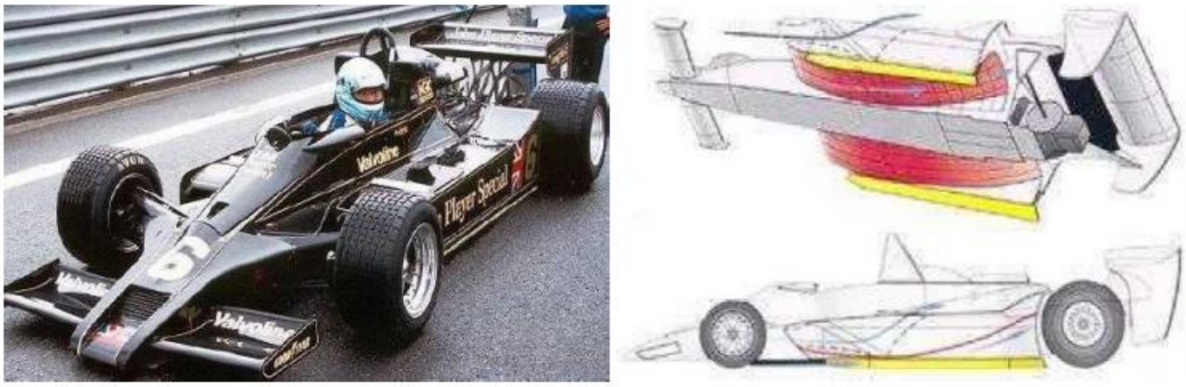

(a) 1977 Lotus 78 '*wingcar*'.

(b) 1977 Lotus 78 sidepods.

Figure 1-6 Introduction of ground effect by F1 Lotus team in 1977 (Casiraghi, 2010).

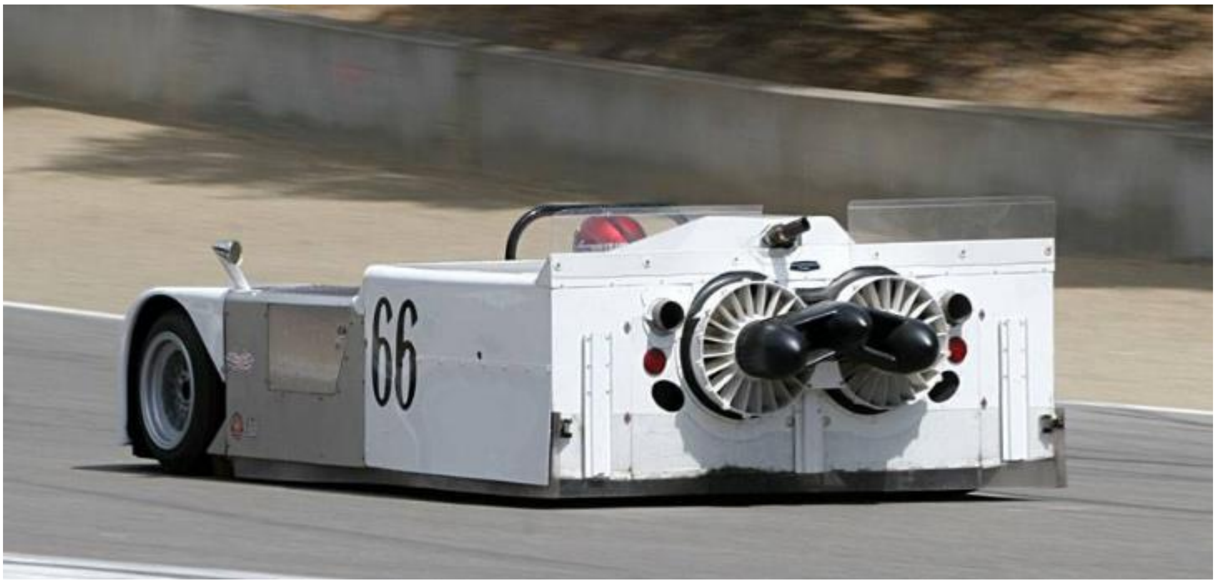

Figure 1-7 Chaparral 2J Body shape (Casiraghi, 2010).

Vortex generator

One of the simplest add-ons is the vortex generator, used mainly to control boundary-layer flows. These can be found in different parts of the vehicle and have a strong impact on the under-body airflow (Katz, 2006). They can be very useful in vehicles performance, both for the direct generation of downforce (positioned over the rear of the roof for example, it effectively helps to reduce drag and increase downforce on the rear wing) and to act as air curtains, sealing off the under-body low pressure area.

Figure 1-8 The vortex generators found on Toro Rosso F1 cars (https://www.carthrottle.com/post/vortex-generators-how-do-they-work/).

Rear diffuser

The diffuser, also known as under-body tunnel or venturi, is a part of the rear under-body of the car (example in Figure 1-9) operating with strong ground effect which improves under-body aerodynamic properties by controlling the transition between the low-pressure high-velocity airflow underneath the car and the slower free-stream airflow at atmospheric pressure by means of the Venturi effect. The fast air flowing from the front splitter is further accelerated at the converging section of the underbody tunnel (nozzle), reaching the lowest pressure at the narrowest flow passage (throat), creating substantial amounts of downforce. The diverging section (diffuser) aims to decelerate the airflow and increase static pressure to ambient conditions in order to correctly recover the kinetic energy of the airflow under the car as efficiently as possible, and therefore reduce drag. If properly designed, a diffuser is a very effective aerodynamic device and in a modern F1 car, for example, the diffuser alone can produce up to 40% of the total downforce considering *"wingcars"* (Figure 1-6) (Wright, 2001).

Figure 1-9 McLaren Senna GTR rear Diffuser (automais.autosport.pt).

Rear diffuser and undertray combination generate the highest amount of downforce of all components. Historically the undertray has been regulated by FIA. This is due to the great expenses used by race teams for the development of this specific part. This means that flat plates are now mandated, that is the car floor should be flat (Katz, 2016). The principle of creating downforce via the undertray and diffuser uses two primary principles: the wing in ground effect, and the venturi tube. A higher velocity below the vehicle will create a low static pressure, thereby “sucking” the car down on the road. The ground effects are complex and include both flow separation, vortex flow, and flow recirculation (Senior and Zhang, 2001). The investigation of these properties is often carried out on simple bluff bodies, such as variations of the Ahmed body illustrated in Figure 1-10.

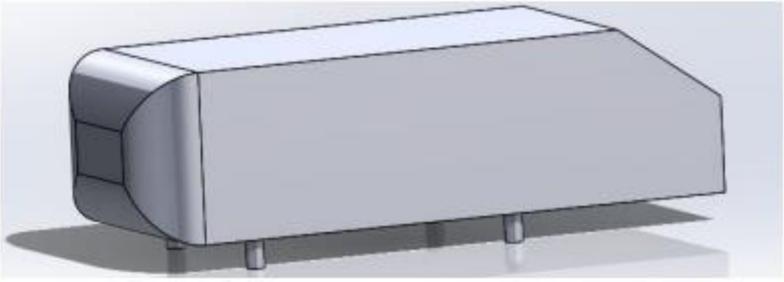

Figure 1-10 Ahmed body with 35◦ upper slant angle.

A diffuser with side plates can then added to the standard bluff body. This is typically investigated with an Ahmed body with 0◦ upper slant (Senior and X. Zhang, 2001) (Zhang, et. al. , 2006). Such a bluff body is used to evaluate the dependence of ride height on optimal diffuser angle, as well as finding the critical height, where the downforce decreases rapidly. The linkage between the generation of downforce and the venturi tube is illustrated in Figure 1-11.

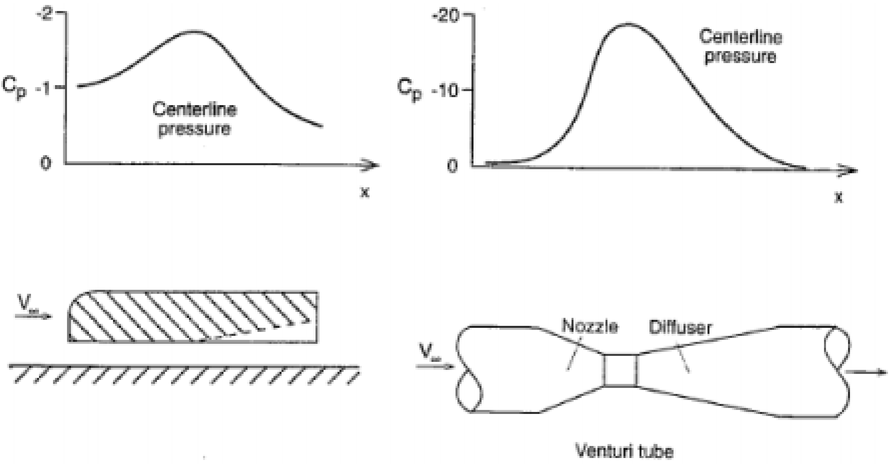

Figure 1-11 Pressure coefficient for modified Ahmed body and common venturi tube (Katz, 1995).

As the pressure coefficient plots illustrate, the behaviours are comparable. Though not as effective as the nozzle of the venturi tube, the undertray accelerates the flow. The highest negative pressure coefficient, and thereby downforce, is found just at the beginning edge of the diffuser. The diffuser then decreases the flow velocity, ideally enough to match the free stream velocity. This is to reduce the pressure gradient in the wake.

In order to avoid separation in an expanding rectangular duct, an equivalent conical section is calculated. This is based on identical length, and in- and outlet areas to the rectangular duct. These dimensions are illustrated in Figure 1-12. The conical equivalent expansion angle must then normally not exceed 7 in order to avoid flow separation (Discetti and Ianiro, 2017).

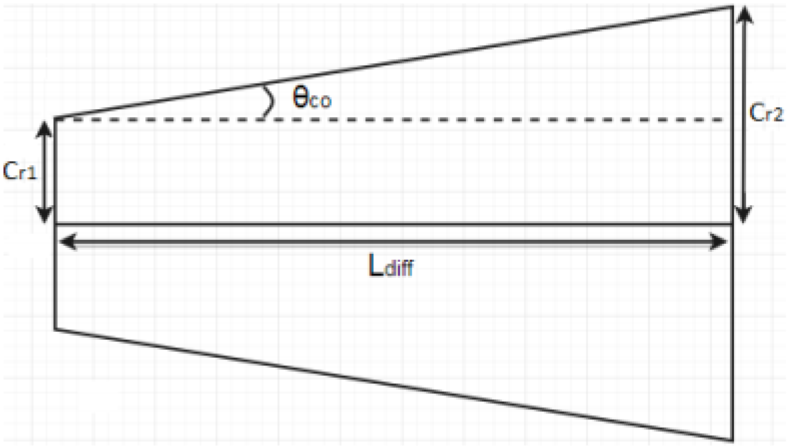

Figure 1-12 Illustration of equivalent conical angle for a rectangular duct.

Here C_{r1} is the cross section height of the diffuser inlet, and C_{r2} is the cross section height of the outlet. Ldiff is the diffuser length. However, racing diffusers can achieve attached flow with angles exceeding angles of 20° (Toet, 2018). The high angle diffusers are used for cars with high ride heights, while diffusers with lower angles are used for lower ride heights.

From Bernoulli equation it is clear that a higher velocity will result in a higher local dynamic pressure. Hence, the local static pressure must decrease. This also means that a lower ride height will increase the amount of downforce. This can be compared to a venturi tube with a decreasing cross sectional throat area. However, this coherence only holds up to a certain point, where the diffuser enters the downforce reducing zone.

Spoiler

Commonly interchanged with wings, spoilers are obstructions to undesirable airflow behaviour around the vehicle and can be found in almost every type of vehicle. They are usually mounted either on the front (called air-dams) or at the rear deck. On passenger vehicles, especially hatchbacks, the adverse pressure gradients created by the steep angle from the roof to the rear window contributes to the separation of the airflow in this area, generating wake turbulence (pushing the car up and down) that causes driving instability at high speeds and adds a lot of drag. By incorporating such devices in this region, airflow separation is delayed minimising turbulence (reducing drag) and improving fuel efficiency. Sharma and R. Bansal (2013) performed a CFD simulation for the flow over a passenger car incorporating such devices and observed a 3.87% reduction in the C_D and 16.62% reduction in the C_L, aiding the stability and fuel efficiency of passenger cars.

Rear Wing

Rear wings can be found on high-performance road legal vehicles as well as in almost every type of racing vehicle. They generate essential downforce to increase back wheels traction thus reducing rear axle lift (improving cornering speeds and high-speed braking), at the cost of adding drag, which places severe limits on the top speed of the car. In contrast to front wings, rear wings operate in the vehicle's wake (usually highly unsteady and turbulent) (Katz, 2006, E. L. Houghton and P. W. Carpenter 2003). Katz and R. Largman (1989) performed experimental studies of an enclosed wheel race car with and without a rear wing and stated that the aerodynamic downforce '*is strongly affected by the interaction between the rear wing and the flow beneath the vehicle*'. Later, Katz and Dykstra (1992) investigated the influence of rear-mount wings on the aerodynamics of two generic race car configurations and concluded that the downforce levels are larger with the coupled configuration than the combined contribution of the wing and the vehicle alone, and that its interaction also alters the pressure distribution and spanwise loading on the wing. Therefore, the three-dimensional flow field created by the body should always be taken into account in the design process of rear wings, and its placement (in the absence of beneficial under-body interaction) should be as high as possible so that little disturbed airflow reaches the wing, maximising downforce. Apart from the vehicle and rear wing interaction, there are other ways to improve its efficiency, such as the use of gurney flaps and endplates. The gurney flap is a short flat plate attached to the trailing edge, perpendicular to the chord line. It was used on race cars prior to aerospace applications as a small vertical reinforcement because of the high speed and structural considerations and to the surprise of aerodynamicists, a drag reduction was reported along with the increase in the overall efficiency (Katz, 2006). The effect of such devices on highly cambered wings is a result of the trailing edge boundary-layer reattachment as well as a change in the direction of the trailing edge flow, inducing larger circulation (Katz and R. Largman, 1989). Three-dimensional effects on airplane wings were conducted by Myose et al, 1998. (Myose et al, 1998) who measured a 13% increase in the maximum lift coefficient ($C_{L\max}$) for a small drag penalty compared with a clean wing, improving the L/D ratio. In three-dimensional wings (or finite wings) such as the front and rear wing, the flow around the side edge (tip) must be considered as the pressure difference between the upper and lower surfaces cannot be maintained, generating strong wing-tip vortices which reduce its effectiveness (Katz, 1995). In order to overcome this problem of leaking flow, endplates are used to separate both surfaces of the wing maintaining a two-dimensional effect at the wing tip and improving its efficiency. In general, increasing the endplate size increases the downforce generation and improves both vehicle yaw acceleration and steady state cornering (Wordley and Saunders, 2006).

1.2 Methods of evaluating aerodynamic forces

Alternatives to Computational Fluid Dynamics studies to evaluate forces on road vehicles are the wind tunnel and/or coast-down tests. These are discussed in turn here.

1.2.1 Wind tunnel

The wind tunnel is the most common tool of the aerodynamicist. It allows the most accurate control of the conditions of the flow over a body (Figure 1-13). The main disadvantage is that it is difficult to build a wind tunnel large enough or fast enough to model accurately the flow over the car at realistic Reynolds numbers. The models used for development are usually 30-50% scale models. The speeds of the cars are also scaled down to between 25% and 50% of those experienced on the road. The aim of scaled wind tunnel tests is to reduce overhead costs. The reduction of scale has the effect on the flow of lowering the test Reynolds number. For example, a 50% scale wind tunnel model, with a 40 m/s air speed (at atmospheric conditions) gives a Reynolds number (based on the car length) of 1/4 that of the full-scale body at 80 m/s. This raises the problem of removing the local Reynolds number effects from the model that would be seen on the full-scale vehicle. For example, small separations over the front of the car may not be present on the tunnel model but these can become important flow features at full scale.

The costs involved with tunnels, whilst low for 'steady state' operation (without the ground moving), must include the set-up costs of both the model and the tunnel itself, which are often considerable. In commercial wind tunnels, these costs are often integrated into the costs of tunnel usage over its expected working life. Cost is, therefore, a major contributory factor when manufacturers consider the continued prolonged use of wind tunnels for model development.

During the 1960s, just when the significance of aerodynamics for race car design was realized, wind tunnel methodology was already mature and widely used by the aerospace industry. It was only logical that wind tunnel testing became an integral part of all race car development projects as well. Small-scale tests helped in investigating basic ideas prior to design cars, and validations were performed later with the actual race car on the track. However, wind tunnel testing of a race car posed several difficulties when using traditional aeronautical wind tunnel facilities. The first major problem was due to the small clearance between the vehicle underbody and the stationary floor of the test section. The second problem was related to how to mount the rotating wheels.

As a result of the increased use of wind tunnels for race car development, customized facilities were rapidly developed, all with rolling ground simulation. Most of these facilities were planned for 30% to 50% scale models with rolling ground simulation capabilities near the 200-km/h range (Figure 1-14). Typically, the model is mounted on an internal six-component balance attached to the wind tunnel ceiling via an aerodynamic strut and the wheels are driven by the rotating belt. The wheels can be attached to the vehicle by using a soft suspension or mounted from the sides using separate balances. The main advantage of this setup is that both ground clearance and a body’s angle of attack could be changed easily.

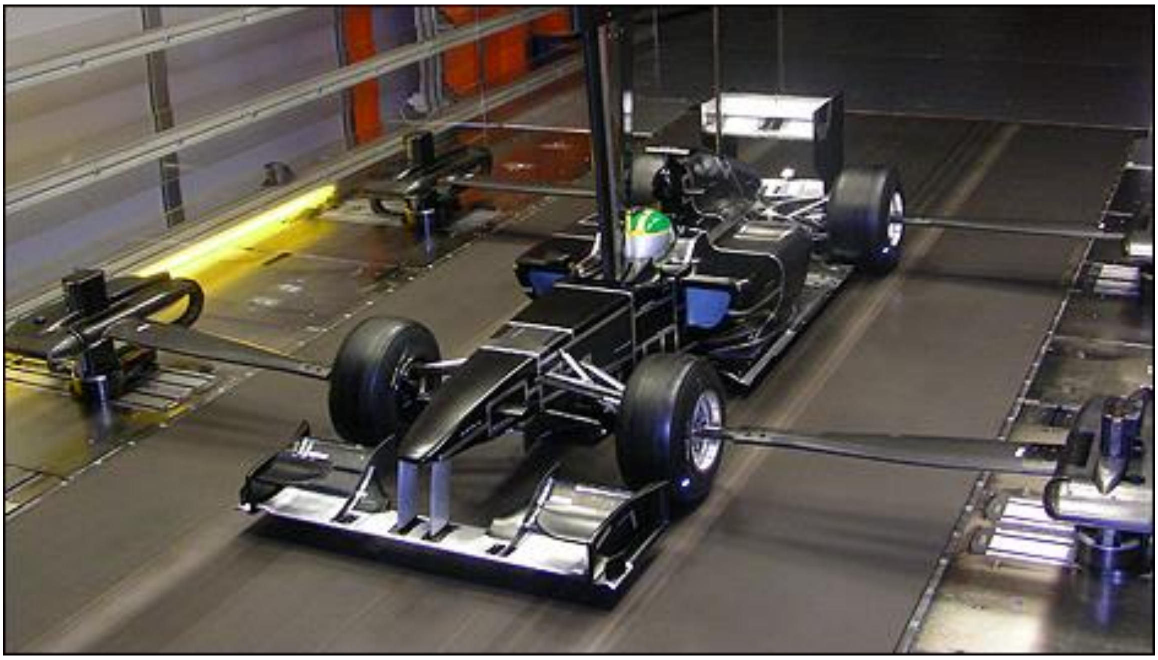

Figure 1-13 The model race car being tested in the wind tunnel (Katz, 2006).

Model size was also a major consideration while developing these facilities. On one hand, cost and space considerations lead to small models, but fabrication difficulties with a too-small model and Reynolds number effects require the largest model affordable. By the end of the millennium, a large number of race car wind tunnels were built, and Lis (2002) provides a comprehensive guide and description of these various wind tunnels. Some of these facilities can simulate full-scale race conditions. One option for full-scale simulation is to use large aeronautical wind tunnels such as the NASA Langley 30-by-60-feet tunnel (Lee et al. 2002).

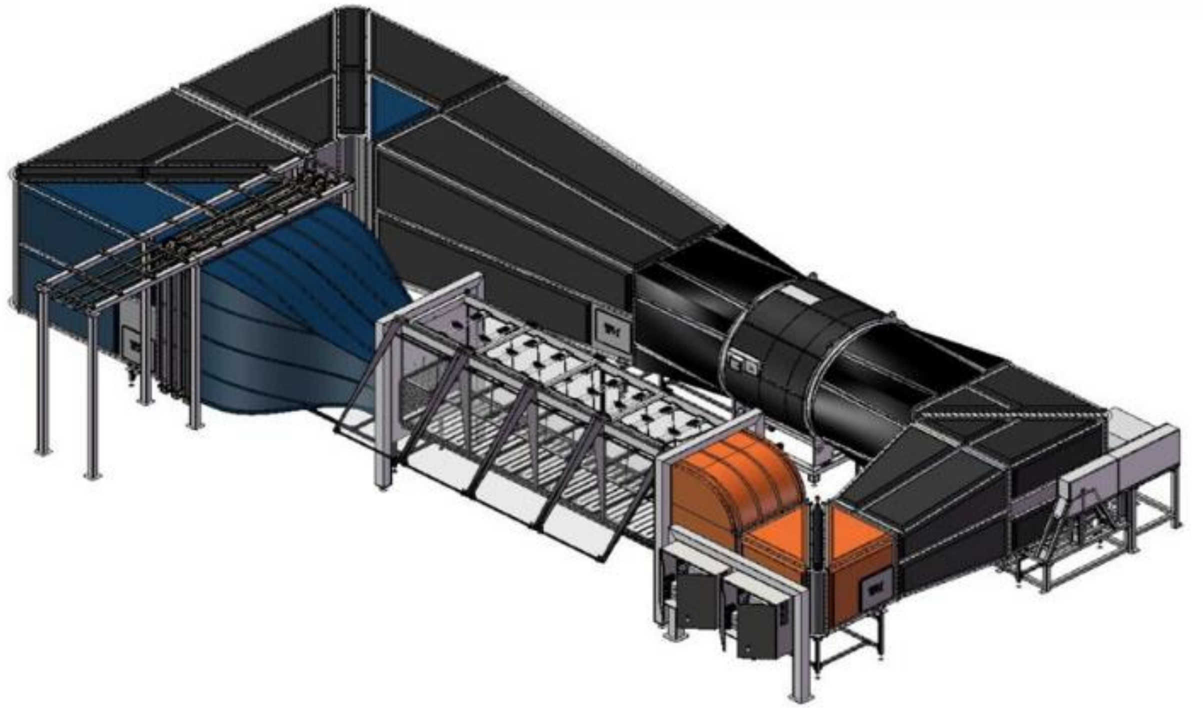

Figure 1-14 Wind tunnel example (Katz, 2006)

1.2.2 Track tests

Some difficulties inherent to wind tunnel testing are simply non-existent in full-scale aerodynamic testing on the racetrack. Rolling wheels, moving ground, the correct Reynolds number, and wind tunnel blockage correction are all resolved and there is no need to build an expensive, smaller-scale model. Of course, a vehicle must exist, the weather must cooperate, and the cost of renting a track and instrumenting a moving vehicle must not upset the budget. Because of the above-mentioned advantages, and despite the uncontrolled weather and cost issues, this form of aerodynamic testing has considerably improved in recent years. One of the earliest forms of testing was the coast down test to determine the drag of a vehicle (Figure 1-15).

The coast down method is a well-established technique, widely used throughout the automotive industry to measure total vehicle drag. In brief, the vehicle is driven up to a known speed and, with the drive disconnected, allowed to decelerate freely. The time rate of change of vehicle velocity is proportional to the total resistive force. Extending this method to isolate the various contributions to the resistive forces, tyres, transmission, aerodynamics, is more difficult. However, using the correct experimental approach and analytical techniques, this can be achieved. A detailed description of this type of analysis is beyond the scope of this study, but it can be found in Passmore (1994). The advantages of this technique are that it ensures the correct 'real world' simulation, and it may, with appropriate analysis, generate the most accurate results of all the methods outlined here.

However, as the technique cannot be applied until there is a running prototype, it is not readily applied to early aerodynamic shape development. The better solution is a combination of CFD analysis and wind tunnel tests.

Figure 1-15 Formula 1 during a track test (Katz, 2006).

1.2.3 Computational Fluid Dynamics (CFD)

The history of CFD can be traced back to the 1960's, when high speed computers became available along with developments in numerical methods. The initial calculations, it can reasonably be said, were very basic and, over time, the level of complexity that can be modelled by CFD has increased dramatically. It is only very recently that computers have developed far enough for complete systems to be modelled rather than small sub-systems of it. The numerical algorithms used in CFD have also developed substantially. The initial solutions were modelled using Euler's, equations with no account taken of the fluid viscosity. This is suitable for inviscid fluid flows, but most problems are viscous in nature.

CFD is the use of a computer simulation to model the flow in almost any scenario, specifically here, automobile aerodynamics. The computer uses the Navier-Stokes equations (usually in time averaged form) on the flow problem in question by separating the domain space into many smaller portions in which the flow is assumed constant. The interaction between these small portions (termed volume elements), governed by the Reynolds-averaged Navier-Stokes equations and a set of boundary and initial conditions, produces the solution of the flow over the whole domain.

With the pressure and velocity known at every point in the domain, including the surface, the forces on the body can be obtained. This is, however, a fraction of the information provided by CFD. The knowledge of the above variables, along with turbulence quantities, can be used to interrogate the flow to a level higher than ever before. CFD is currently used as a powerful tool for the aerodynamicist by reducing the time taken and the cost for developing an aerodynamically efficient car.

In conclusion, CFD is very useful in the preliminary design phase, before a wind tunnel model exists. It is almost the only approach for effective wing aerofoil shape developments because of the detailed pressure and skin friction information. It is a powerful tool for calculating vortex flows and for providing valuable flow visualizations (to explain other experimental observations). Its advantage also lies in the fact that the results can be viewed over and over again and new aspects of the solution can be investigated. As most of the recent studies indicate, CFD is an excellent complementary tool along with other methods such as wind tunnel testing. Its weakness is rooted in scaling issues such as the prediction of transition from laminar to turbulent flows or the calculation of separated flow and unsteady wakes (Figure 1-16).

The bottom line is that CFD solutions depend on user-defined elements such as turbulence modelling and grid generation, which many people view as the next hurdle facing code developers. Because the large-scale flow regimes over most vehicles depend on the predictability of the aforementioned transition and turbulence, the complete flow field cannot yet be modelled economically.

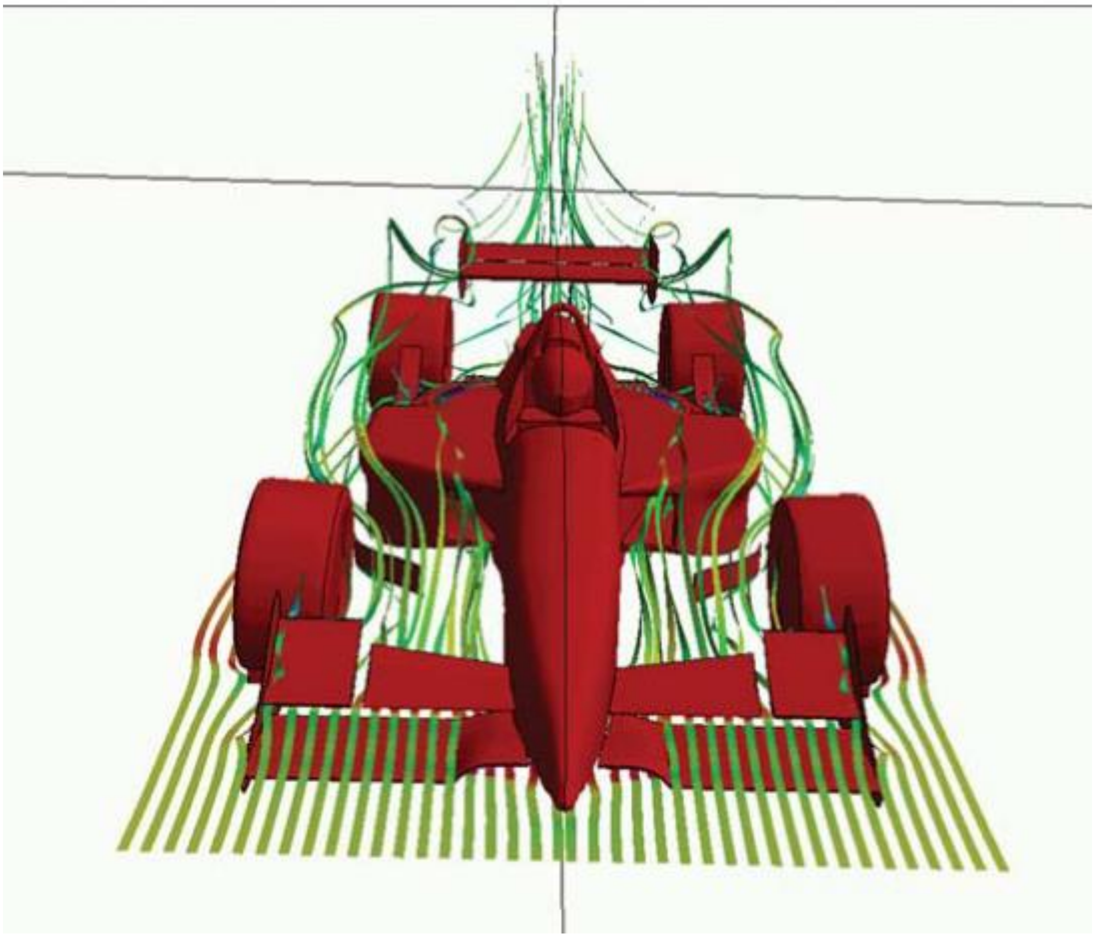

Figure 1-16 Streamline traces released ahead of the front wing of an Indy-type race car (Katz, 2006)

1.3 Bluff bodies

Bluff bodies refer to bodies with blunt bases that cause leading-edge flow separation and the formation of recirculation regions in the near wake of the bluff body (Cooper, 1993). This results in a lower pressure on the back surface of the body and sets up a large difference between the relatively high pressure acting on the front of the bluff body and the lower base pressure. Automotive bodies are considered as bluff bodies moving in close proximity to the ground. It has been established that the pressure drag is a direct consequence of flow separation which occurs primarily at the rear end of the body (Ahmed, 1984). More recently, Morelli (2000) mentioned that pressure drag can contribute to approximately 75% to 85 % of total drag.

1.4 Ahmed body

The important features of the flow around a bluff body are the regions of flow separation and recirculation in the wake. Even the simple shapes produce complex flow structures. These structures are formed in the vehicle wake, which is the main flow separation region, governing the drag experienced by the body (Hucho, 1998). To achieve the qualitative understanding of the relation between wake structure, pressure distribution, drag and geometric configuration, Ahmed et al. (1984) proposed a simplified car model which could generate the main flow features of real vehicles without their geometric details.

In the early 1980s, the experimental research performed by Ahmed became a milestone in automotive aerodynamics. In 1981, Ahmed published the analysis of wake structure over typical automobile shapes. Later, Ahmed et al. (1984) perform the experimental analysis of aerodynamics over a simplified, ground vehicle geometry with a bluff-body shape. The author provided pressure and force distributions over the model. In addition, the turbulent wake was investigated as function of rear slant angle, which vaguely represents the rear window surface of a realistic vehicle model. Ahmed et al. (1984) concluded thar roughly 85% of the drag on a vehicle body would be consequence of the pressure drag only.

The simplified vehicle shape employed by Ahmed et al. (1984) generates fully three-dimensional regions of separated flow which may enable a better understanding of such flows. Ahmed's body, shown in Figure 1-17, is 1044 mm long (L), 288 mm high and 389 mm wide. The slant part is 222 mm long, whatever the angle. The bottom surface of the Ahmed body is located 50 mm above the ground.

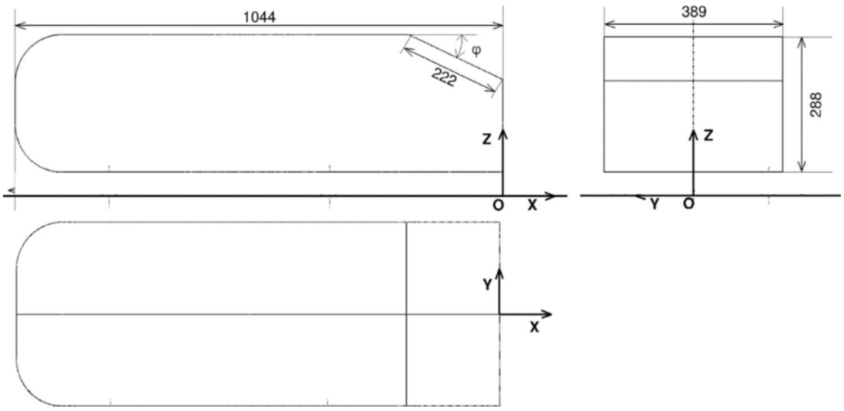

Figure 1-17 Ahmed body model dimensions

1.5 Literature Review

To attain a good performance of race cars, an appropriate combination among all elements such as engine, tyres, suspension, road and aerodynamics is required. Nowadays, aerodynamics has gained an increased attention in motorsports with regards to the maximization of the race car performance and passengers car efficiency.

In the last decades, many studies on race car aerodynamics devices started. As of today, multiple studies of race car aerodynamics exist about various devices and parameter, with and without ground effect and considering different wind profiles.

This chapter is an overview of other academic pieces of research about reference car models, CFD analysis of vehicles, turbulence models and meshing model in automotive aerodynamics.

1.5.1 **General Aerodynamics studies**

Studies on aerodynamics have originated from aeronautics and marine applications, (Hucho 1998). According to (Barnard, 1996) at the turn of World War Two, substantial progress on aircraft aerodynamics was obtained due to the amount of research and analysis being done. Study of vehicle aerodynamics first began to surface during the earlier part of the 20th century and has continued up until the present day. During the earlier part of the 20th century, vehicle aerodynamics study was associated with vehicle performance (Hucho, 1998). Aerodynamicists during that time carried out vehicle aerodynamics research with the aim to produce vehicles that can achieve a high speed to power ratio. To achieve high vehicle performance, much of the attention focused on lowering the vehicle drag coefficient (C_D), which accounted for about 75% to 80% of total motion resistance at 100 km/h (Hucho, 1998). However, in the later part of the 20th century, during the oil crisis of 1973-1974, the focus on vehicle aerodynamics study shifted towards lowering the drag coefficient in order to produce vehicles with better fuel economy, (Hucho, 1998).

The trend shifted again in the early 1990’s especially in North America where a low fuel price coupled with the increased popularity of light trucks and sport utility vehicles (which have drag coefficient of around 0.45), have reduced the importance the need on research to reduce drag coefficient, (George, 1997). Aerodynamicists then shifted their focus towards designing vehicle that provides maximum comfort to its occupants. Vehicle comfort consists of finetuning areas such as ventilation, heating, air conditioning and minimising wind noise inside the vehicle (Hucho, 1998).

1.5.2 **Airflow Around a Ground Vehicle**

Analysis of flows around a ground vehicle however, presented a different problem. As opposed to a streamline body of an aircraft, ground vehicle exists as a bluff body. The streamline feature of an aircraft results in airflow around the aircraft to be fully attached over most of its surface (Barnard, 1996). On ground vehicles, the flows are strongly turbulent and three dimensional with steep pressure gradients, (Ahmed, 1998). According to (Alam, 2000), ground vehicles operate in the surrounding ambient turbulent wind. This is different from aircraft since they travel above the turbulent atmospheric boundary layer. Furthermore, road vehicles can also travel at various high yaw angles depending on the nature of cross wind. Traveling at various yaw angles causes increased separated flow on the leeward side of the vehicle, adding more complexity to the flow field.

Airflow movement around the vehicle starts from the front. According to (Barnard, 1996), the airflow movement will cause the development of a boundary layer close to the vehicle wall surface. The boundary layer thickness will increase as the airflow movement progresses around the vehicle. (Barnard, 1996) classified the boundary layer generation on the vehicle wall surface into two stages; laminar and turbulent. During the initial stage, boundary layer flow exists in a laminar form. Near the front edge of the vehicle, the laminar effect will cause airflow layers to slide over each other. Minimum skin friction drag formed between layers of airflow with the vehicle wall surface will cause the outer air layer moving faster than the inner one. This will slow down the flow. The slowing effect spreads outwards and the boundary later gradually becomes thicker. According to Barnard (1996), on most ground vehicles, the laminar boundary layer does not extend for much more than about 30 cm from the front. Further downstream, instabilities develop and transition to turbulent flow takes place. In the turbulent boundary layer, the flow is still streamlined in the sense that it follows the contours of the body. The turbulent motions are still of very small scale. In the turbulent boundary layer, eddies are formed (groups of air molecules) resulting in rapid mixing of fast- and slow-moving masses of air (turbulent diffusion). The turbulent mixing will then move further outwards from the surface. However, very close to the surface within a turbulent boundary layer flow, a thin sub layer of laminar flow still exists. The two distinct differences between the flow mechanisms in the laminar and turbulent flow is that in laminar flow, the influence of the surface is transmitted outward mainly by a process of molecular impacts, whereas in the turbulent flow the influence is spread by turbulent mixing. In the turbulent boundary layer, some of the energy is dissipated in friction, slowing airflow velocity, resulting in a pressure increase. If the increase in pressure is gradual, the process of turbulent mixing will cause a transfer of energy from the fast-moving eddies in the turbulent boundary layer. If the rate of change in pressure is too great, for example in sharp corners, the mixing process will be too slow to push the slower air molecules moving. When this happens, the boundary layer flow stops following the contours of the surface, resulting in separation. Air particles downstream of the separation region will then move towards the lower pressure region in the reverse direction to the main flow. This is known as an adverse pressure gradient. Further downstream, the flow may reattach. The point between the region of separation and reattachment, where air is circulating is called the ‘separation bubble’. Separation will normally occur if the resultant flow encounters a sharp edge. It is always important for ground vehicles to have smoothly rounded edges everywhere. Each type of separation can form a separation bubble zone either by reattaching itself downstream to the flow or it can be transformed into a wake, which recirculate frequently. (Hucho, 1998) named this frequent circulation as “dead water” zone, a term used in naval architecture. (Farabee, 1986) examined that the length of the separation bubble can be up to 100 times its height. Separation bubble zone happens normally on a region in front of the windshield and on the side of the fenders while “dead water” zone normally happens on the rear surface of the ground vehicle.

The effect of separation and reattachment dominates most of the ground vehicle surface region. According to Ahmed (1998), vehicle aerodynamics operates mainly in the Reynolds number region in excess of 10^6. Typical areas around the vehicle that exhibit small separated regions are the body appendages such as the mirrors, headlights, windshield wipers, door handles and windshield junction (Figure 1-18). Larger flow separation regions around the vehicle include the A-pillar, body underside, rear body of the vehicle and in the wheel wells, (Hucho, 1998).

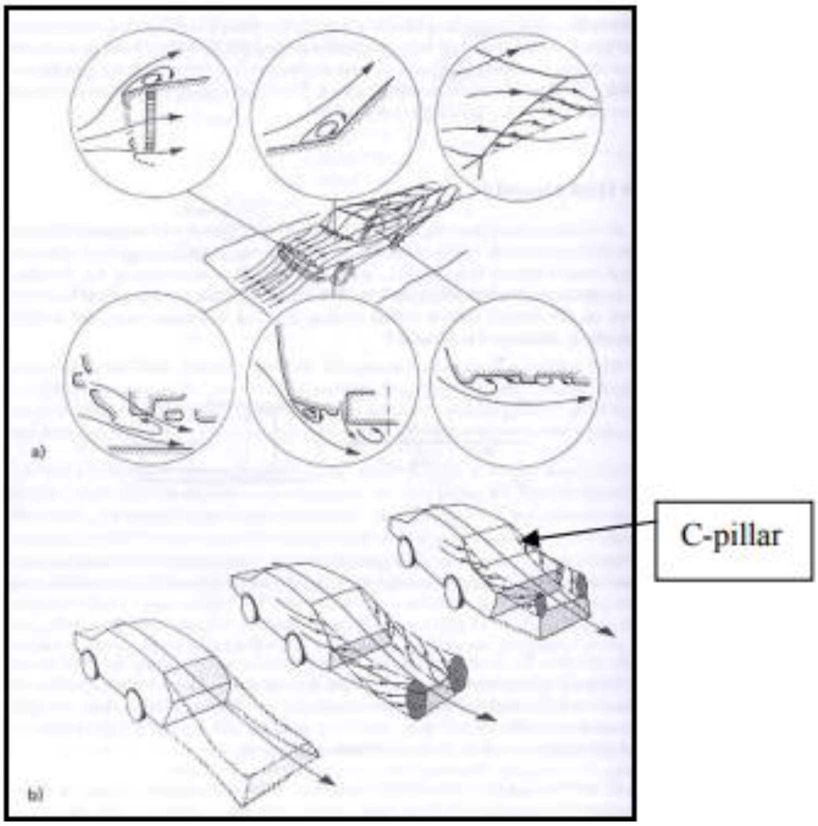

Figure 1-18 Areas of Separation around a Vehicle (Hucho, 1998)

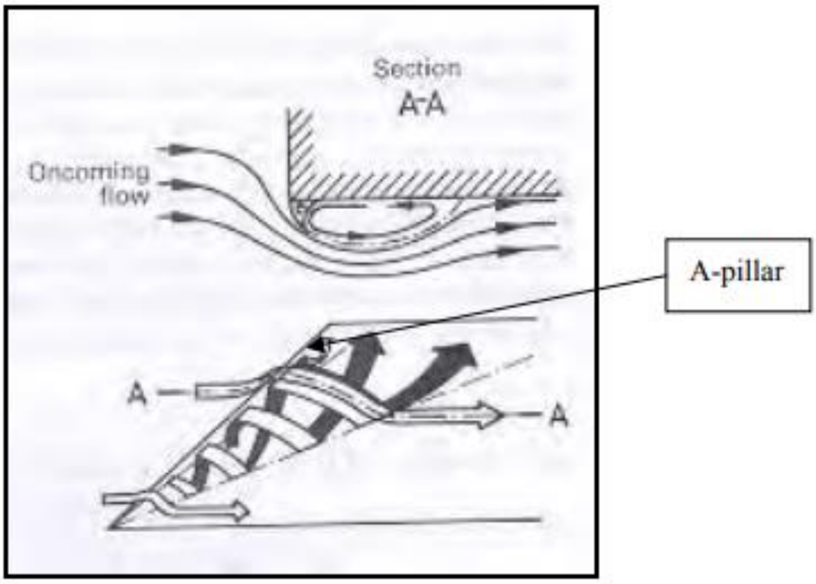

Figure 1-19 Slanted A-pillar Vortex flow (Hucho, 1998)

Although airflow around a ground vehicle exists predominantly in three-dimensional form, (Hucho, 1998) indicated that a quasi-two-dimensional flow types also exist. The quasi-two-dimensional type flow separates on the edge running perpendicular to the local direction of flow. The separation causes vortices to roll up with their axes almost parallel to the separation line. Turbulent mixing dissipates most of their kinetic energy making their development as continuing free trailing vortices, often weak and even untraceable. The quasi-two-dimensional flow often occurs around areas such as the hood front edge and the front part of the vehicle windshield. Furthermore, according to (Hucho, 1998), the second type of separation normally happens at edges around which air flows at some angle. According to (Hucho, 1998) the air stream then forms a cone-shaped helical vortex. The regions where these vortices tend to be generated on a car are behind the A and C pillars (Figure 1-18 and Figure 1-19). The axes of these vortices run essentially in the streamwise direction. The three-dimensional vortices are very rich in kinetic energy and this containment in kinetic energy is determined by the ground vehicle geometrical conditions, mainly by the inclination of the A and C pillar angle at which they separate.

1.5.3 Numerical Studies with Ground Influence

Ground influence is highlighted all over as a major parameter for race car aerodynamics. The significant results include the pressure distribution underneath a front wing and the effect of downforce and drag. (Kiffer et al. 16, 2004) studied the influence of angle of attack and ground effect on a Formula Mazda wing. It is reported that the ground clearance has significant influence on the downforce production. In dependency of angle of attack, it is shown that the downforce increases about 20 % from an angle of attack of 0° to 12°. The Mazda race car wing starts with stall conditions at about 12° angle of attack. The drag is increasing by about 50% at 12° compared to 0°. (Ranzenbach and Barlow, 1994) used Reynolds Averaged Navier Stokes to study the NACA0015 profile as a numerical study in addition to their experimental study. Their findings include that downforce is a function of ground clearance and increases with decreasing ground clearance. Further, the drag increases with decreasing ground clearance. They also found that large separation occurs on the suction surface of the wing at small ground clearance. (Mokhtar, 2005) studied the influence of ground clearance on four aerofoil sections, the S1223, E423, LNV109A, and NACA9315. All aerofoil sections have a similar behaviour for downforce and drag. Large ground clearance does not detect most of the effect on the aerofoil. The downforce increases with decreasing ground clearance, and the downforce remains more or less constant for a ground clearance larger than height to chord ratio $H/c = 0.6$ (Mokhtar, 2005). The drag increases with decreasing ground clearance. However, the drag is way more influenced by the ground clearance than the downforce. The effect weakens with increasing ground clearance; however, it never gets steady like the downforce. The effective range of ground clearance does not get influenced by endplates. (Mokhtar and Lane, 2008) analysed the flow around a wing and showed the changes of pressure and velocity which are the reason for the downforce and drag increase. A study of a symmetric aerofoil, the NACA0012, shows that the generated downforce reaches its maximum at a ground clearance of 10% of the wings' chord length. With decreasing ground clearance under 10% the downforce decreases significantly. The reduction from 0.1 to 0.09 is observed to be 3.8% whereas the decrease between 0.06 and 0.05 is 57%. The drag increases at an almost constant rate as the ground clearance decreases with its peak at 0.08. The lift over drag ratio increases as the H/c increases. Although the lift over drag ratio increases, it is not a ratio which race car designers are very interested in; it is more the magnitude of the actual forces. The study showed the influence in terms of flow characteristics and pressure distribution. For both, the upper surface of the wing is less influenced by the ground clearance than the lower surface (Mokhtar and Lane, 2008).

(Price, 2011) simulated a FC 63-137 front wing on a SAE race car. He reported that the suction peak moves backwards in ground effect compared to free stream case. The suction peak at ground clearance $H/c = 0.1$ is for the pressure coefficient 278% higher than in free stream. Besides that, (Price, 2011) showed that the vortices on the wing tips have a negative influence. His study did not include endplates. He reported a negative effect of the wake on the wheels and pointed out that endplates were used to redirect the air around the tire.

1.5.4 Experimental Studies with moving Ground Influence

Zhang and Zerihan, 2003, studied a multiple element wing in ground influence with a moving ground. The main element was a modified General Aviation-Whitcomb (GAW) airfoil. The study showed that the main characteristic of a double element wing was similar to the single element wing. A high and a low flap angle were tested for the second element. The maximum downforce occurred at a ground clearance of H/c=0.066 for the low flap angle and at H/c = 0.079 for the high flap angle. Figure 1-20 shows the behaviour of the downforce for high and low flap angle. Region c shows the region for ground clearance smaller as the maximum occurrence. Both flap angles show a transition from region a to region b. Where in region a, the downforce curve has a high gradient which turns into a small gradient at the beginning of region b. The high flap angle produces significantly greater downforce at larger ground clearance than the low flap angle. With decreasing ground clearance, the difference gets smaller.

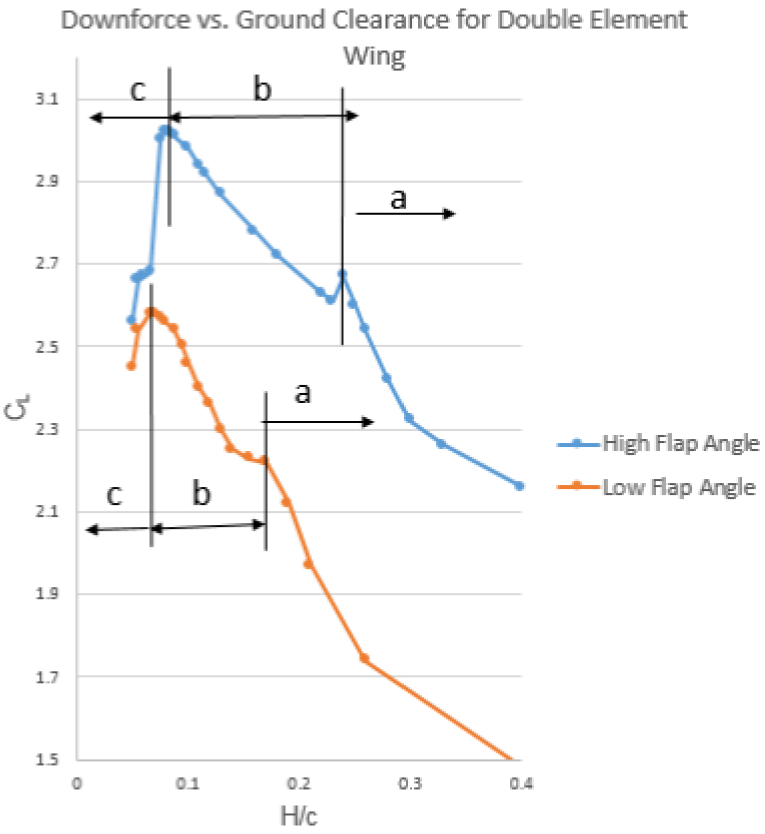

Figure 1-20 Downforce vs. ground clearance for double-element wing (Zhang and Zerihan, 2003)

The study shows that the main element produces most of the downforce and dominates the turbulent wake development. The high flap angle case shows a sharp reduction after reaching the maximum downforce because of the boundary layer separation. It can be seen that the maximum downforce point in terms of ground clearance is lower for the low angle flap than at a single element wing. The high angle flap maximum occurs just slightly lower since single element wings reach their maximum at a ground clearance of approximately *H*/*c* = 0.08 to 0.09.

1.5.5 **Experimental Studies of Diffuser in Ground Effect**

The fact that diffusers placed in ground effect are capable of generating negative pressures, hence downforce, was recognized some time ago. Several studies has been conducted of 3D underbody diffuser flows. (Cooper et al., 1998) conducted the most comprehensive test so far. Test parameters include height and angle. The width of the diffuser, L/W= 1.86, is wider than that normally found on an open wheel race car, however it is still relevant. A summary of the fluid dynamic mechanisms which combine to produce downforce on a 3D diffuser equipped model is given by (Cooper et al. 1998). The force enhancement with ride height reduction, maximum force, and downforce reduction at lower ride heights were identified. They surmised that, at a critical height, the boundary layers under the body and above the ground merge and become a substantial fraction of the ride height. They also documented a difference in the downforce curves between smaller and larger angles of diffuser below a certain ride height, the latter showing a reversal in the consistent trend in downforce seen in all the curves above this ride height. No explanation was given for this finding.

George (1981) observed a leeside vortex pair on the upsweep surface of his model which appeared to keep the flow attached to the diffuser surface at angles where it would be expected to detach, and thus maintain downforce. In later tests on a venturi-type model (George and Donis, 1983) found that flow entrainment underneath the side-skirts resulted in a separated shear layer from which a vortex pair formed. They observed loss of downforce and asymmetric diffuser surface patterns when the model skirts were sealed to the fixed ground plane, attributing the phenomena to the absence of the vortices originating from the skirt edges. At low ride heights, an unsteady vertical oscillation of the model led to their suspicion of either vortex breakdown inside the diffuser or an association with a small separated region of fluid found on the ground plane. This was thought to be a flow away from the ground up towards the model, induced by the vortices. Due to the broad nature of the study, these findings were not probed further. Both of these tests were conducted using a fixed ground plane. The work by (Senior et al., 2001), employed a wide range of test methods including pressures, force, LDA, PIV, and surface flow visualization. The role of force enhancement vortices is identified and classification of force regimes given. It was found that, for a bluff body with a 17 deg diffuser, the rapid reduction in downforce was not due to the increased influence of the boundary layers, as changes in the Reynolds number did not influence the critical ride height (Senior et al., 2001). It was also found that one of the two counter-rotating vortices that form in the diffuser disappears below the critical ride height, resulting in an asymmetric flow pattern with flow reversal on one side. Four different types of force behaviour were identified through a range of ride heights.

1.5.6 Computational Studies of Diffuser in Ground Effect

Computational simulation of diffuser flow in ground effect was conducted as part of the research of (Cooper et al. 1998). The 3D model with 9.17 and 13.5 deg diffusers was simulated as a symmetric half-model and without the side plates. RANS simulation was performed and the $k-\omega$ turbulence model used. Fine near-wall grid spacing allowed resolution to the diverging wall. Adequate lift and pressure predictions were obtained for the 9.17 deg diffuser; however, the simulation was less successful for the 13.5 deg diffuser. The simulated flow field was not presented. The results of these and similar computations for different diffuser lengths were conducted for use in their analytical model (Cooper at al. 2000). Details of the solutions were not presented; however, the results were utilized in providing certain input data for the model. The model calculated the total underbody mean-effective pressure coefficient from a correlation based upon the CFD data for different diffuser lengths and on the experimental data. Predictions of the underbody mean-effective pressure coefficient calculated for diffusers of various lengths in proportion to model length were given for several area ratio parameters. The authors provided a useful insight into the design of underbody diffusers, concluding an optimum area ratio parameter of approximately (AR=)1–2 and a diffuser of approximately half the length of the vehicle itself.

1.6 Motivation and Objective

As mentioned before external aerodynamics is of utmost importance in the automotive industry. Engineers in the field of aerodynamics have been using CFD for a long time. Traditionally, CFD is used to optimize car shapes in terms of lift and drag, and study salient flow features. External flow analysis over car geometry is always an interesting part of research in aerodynamic field. The study is usually performed employing experiments in wind tunnels as well as computational simulations. Due to the cost of experimental studies, and the evolution of computational power in the last years, CFD has been gradually becoming a viable tool in vehicle design and in aerodynamic fields, particularly when the results are validated against wind tunnel tests. The aerodynamics forces on road vehicles are the result of complex interactions between flow separation and the dynamic behaviour of the released vortex wake. Drag is caused due to the pressure difference between the frontal and the rear end of the vehicle. It can be reduced by modifying the design of the vehicle, leading to a change of the air flow around it.

Automotive aerodynamics comprises the study of aerodynamics of road vehicles. Its main goals are the drag reduction, noise minimization, fuel economy improvement, elimination of undesired lift forces and minimization of other causes of aerodynamic instability at high speeds. We also look into design and aerodynamics of a vehicle in order to maintain better control for steering and braking. It is very often necessary to generate downforce to improve traction and thus cornering abilities. Lift can be dangerous for an automobile, especially at high speeds. So, in order to maintain control for steering and braking, cars are designed so that the automobile exerts a downward force as its speed increases. However, increasing this downward force increases drag, which in turn, limits the top speed and increases fuel consumption. Hence, these two forces must be carefully balanced.

The main objective of the present work is to propose a geometry optimization of the model in order to improve the aerodynamic efficiency, that is minimize drag and lift. The Ahmed model is used for a preliminary 3D numerical simulation. These preliminary simulations are used to develop the optimization loop as well to validate all techniques and procedures. After that the same techniques are used to optimize a Car geometry through the design of a rear diffuser. The three-dimensional simulations are conducted for a symmetrical half model, the ground effect is considered in the boundary conditions. The URANS (Unsteady Reynolds Averaged Navier-Stokes) approach was chosen, employing the $k - \omega$ SST model.

2 Fundamentals

The topics in this chapter covers the main aerodynamic concepts of a car body, including forces. The discussions are made considering that the main area that will be covered is CFD simulation.

2.1 Aerodynamic Forces

2.1.1 Drag force

When the fluid flows over a surface, the surface will resist its motion. In aerodynamics, drag is the fluid drag force that acts on any moving solid body in the direction of the fluid freestream flow. Aerodynamic drag on a race car is the sum of friction, form and pressure drag.

Friction drag is due to the shear stress resulting from the friction between air and the body surface for a small element. This type of drag only happens due to the effect of viscosity at the surface of the car. It occurs as air particles pass over a car surface and the layers of particles closest to the surface adhere. Skin friction drag is caused by the actual contact of the air particles against the surface of the moving object. The layer above these attached particles slides over them but is consequently slowed down by the non-moving particles on the surface. The layers above this slowed layer move faster. As the layers get further away from the surface, they slow less and less until they flow at the freestream speed. The area of slow speed, called the boundary layer, appears on every surface, and causes one of the three types of drag. The amount of surface drag that is created per square metre of surface area is relatively small. However, as the boundary layer covers much of the surface of the vehicle.

Turbulent flow creates more surface drag than laminar flow due to its greater interaction with the surface of the car. Rough surfaces accelerate the transition of boundary layer airflow from laminar to turbulent which, in turn, increases the thickness of and the airflow disruption within the boundary layer. These increases result in more air molecules being affected by the movement of the car and a corresponding increase in surface drag.

The force required to shift the molecules of air out of the way creates a second type of drag, form drag. Due to this phenomenon, the smaller the frontal area of a vehicle, the smaller the area of molecules that must be shifted, and thus the less energy required to push through the air. With less engine effort being taken up in the moving air, more will go into moving the car along the track, and for a given engine power, the car will travel faster. Form drag and pressure drag are virtually the same type of drag. The separation of air creates turbulence and results in pockets of low and high pressure that leave a wake behind the car. This opposes forward motion and is a component of the total drag.

Pressure drag is the component which is identified on the external surface of the car generated by normal surface forces. As when the vehicle moves with the forward direction of the air then the surface of the car experience the pressure which varies over the different points of the car as shown in **Error! Reference source not found.**.

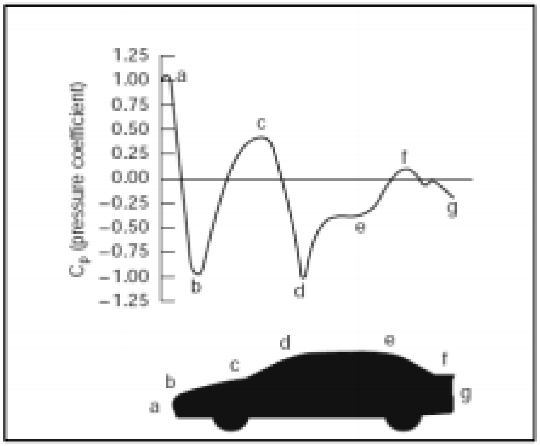

Figure 2-1 Pressure distribution over a car body (Happian-Smith, J., 2004).

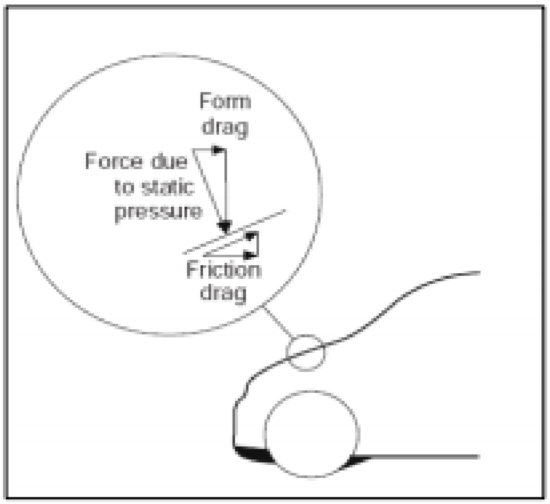

Figure 2-2 Force acting on one surface element (Happian-Smith, J., 2004).

2.1.2 Lift Force

When an object travels through air, it often creates either a lift force or a downforce. A wing can make a plane to take off, but if we put it upside down, it can make a high-speed race car stay to the ground. The same principle that allows an airplane to rise off the ground by creating lift from its wings is used in reverse to apply force that presses the race car against the surface of the track. Typically, the term "lift" is used when talking about any kind of aerodynamically induced force acting on a surface, along a line perpendicular to the freestream. This is then given an indicator, either "positive lift" (up) or "negative lift" (down) as to its direction, since most aerodynamic devices were invented for aircraft and were designed to lift them into the air.

In race car aerodynamics, the vertical downward force provided by aerodynamic devices mounted on a race car pushes the tires onto the track surface to provide more grip, which in turn enables higher cornering speeds and faster braking. The grip between tires and track pavement provided entirely by aerodynamical forces is called "aerodynamical grip" and is distinguished from "mechanical grip" which is a function of the car mass repartition, tires and suspension. The creation of downforce by passive devices such as wings, bodywork, diffusers etc. can almost always only be achieved at the cost of increased aerodynamic drag (or friction), and the optimum setup is almost always a compromise between the two. Because it is a function of the flow of air over and under the car, and because aerodynamic forces increase with the square of velocity, downforce increases with the square of the car's speed and requires a certain minimum speed in order to produce a significant effect.

2.2 General concepts in fluid mechanics

2.2.1 Streamline flows

Streamline flow is a kind of flow which at any point over the car surface remains constant with the same pattern, that is defined as the flow in which the fluids flow in parallel layers such that there is no disruption or intermixing of the layers and at a given point, the velocity of each fluid particle passing by remains constant with time. On the other hand, if the flow follows the outline of the vehicle body which is streamlined. In this case the flow can be say that it is attached. (Barnard, 1996).

2.2.2 Stagnation regions

When the air strikes a vehicle body, it is divided into different flow lines over the body. The divided flow goes over and under the body. The point where the air strikes and then stays stationary at the position or the part where this occurs is known as the stagnation region. (Barnard, 1996)

2.2.3 Separation bubbles

When the air touches the surface of the car at some points and is not able to follow the geometry contour, it detaches. So, the separation bubbles are formed in the area between the point where the boundary layer flows separates and the point when the flow reattaches. (Barnard, 1996). Figure 2-3 **Error! Reference source not found.**shows the separation and the reattachment of the flow.

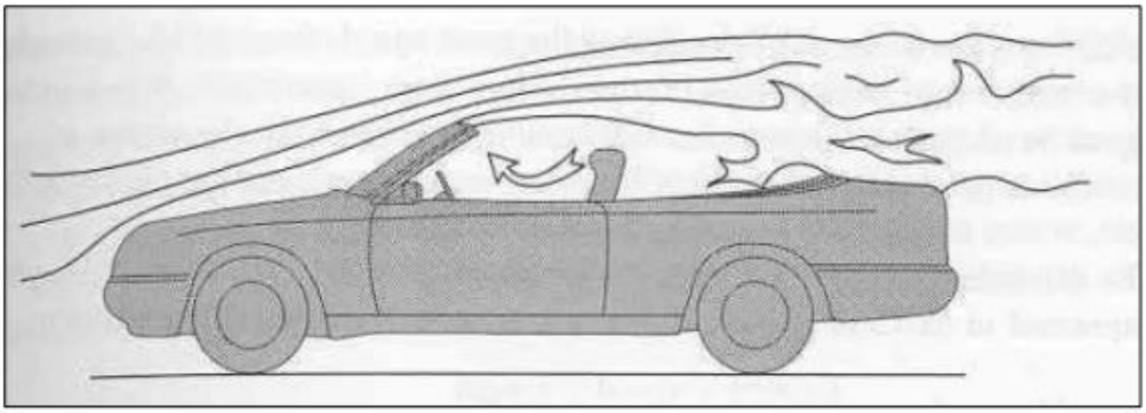

Figure 2-3Separation and reattachment of the flow (Barnard, 1996).

2.2.4 Reynolds number

The boundary layer and the thickness of the layer affect the friction on the surface, flow separation etc. The flow patterns depend on the length of the body, viscosity, speed and the density which can also be grouped as the one quantity known as the Reynolds Number. It can be expressed as follows: (Barnard, 1996)

$$Reynolds\ Number = \frac{Density\ X\ Speed\ X\ Length}{Viscosity} \qquad (1.1)$$

This has the same value in any system of units, as this is a nondimensional quantity. If the speed of the car increases the Reynolds number also increases, which results in thinner boundary layers. Therefore, it is clear that this number is very important in determining the type of flow over the surface of the car.

2.2.5 Vortices

In the flow regions there are some parts which often knows as the vortices which is mostly formed by the swirling flow structures, which mostly occurs with the whirlwinds. This is given based on the backlight angle of the car so the vortices which formed at the back of the car are knows as the trailing vortices. These vortices also affect the lift of the car. They do not remain for a long time, and are not observed anymore after a fairly small length downstream of the vehicle (Barnard, 1996).

2.2.6 Kármán vortices

These types of vortices are formed mostly in the flow over the bluff bodies like buses, trucks, or the simple car body shapes like the Ahmed body. These vortices show an alternating pattern at a regular frequency, known as the Strouhal frequency. (Barnard, 1996)

2.3 Vehicle body and its concepts

The saloon cars are described in different theory books. Cars are bluff bodies with the drag coefficient of 0.3-0.4. (Watkins and Vino, 2008) There are multiple theories behind the vehicle body and its concepts. When the solid body moves in a fluid, either gas or liquid, the fluid resists the motion of the object in the opposite direction. The large effect on the aerodynamics of the body is dependent on the geometry of the object. Drag and lift depend mainly on the size and shape of the solid object. (National Aeronautics and Space Administration, 2012)

2.3.1 Height from the ground level

This includes in the increase of downforce acting on the car which helps it to stick it to the ground. If the space between the cross-sectional area of the vehicle body and the ground is reduced, then the flow of the air under the body of the vehicle will increase which results in lower pressure underneath the car and it means it will result in more downforce, which helps to maintain stability while the vehicle body is in motion in the fluid. This downforce is also known as ground effect. It can be increased with the smaller ground clearance. In addition, the downforce values can be increased by adding skirts alongside of the vehicle body. (Hall, 2013) Figure 2-4 shows lift and the drag versus ground clearance for a model with the generic underbody tunnel.

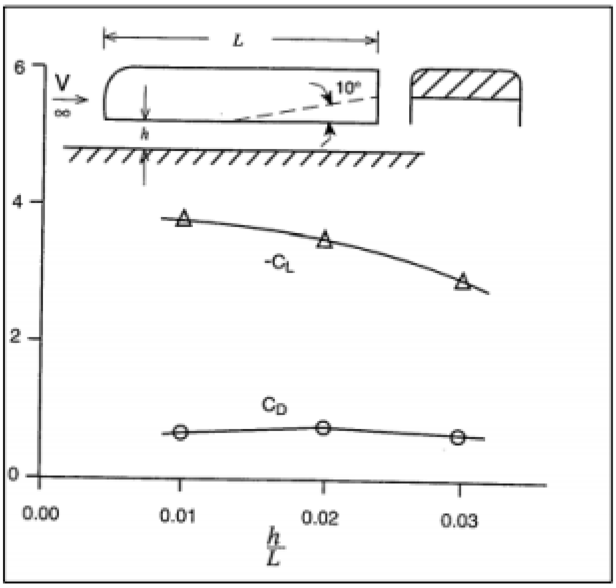

Figure 2-4 Velocity against the ratio height over length (Hall, 2013)

2.4 Important equations in fluid mechanics

2.4.1 Navier-Stokes equations

The relationship between the pressure, viscous and momentum forces in a fluid flow can be expressed by the Navier-stroke equations. Air is known as a Newtonian fluid and its motion is governed by the Navier-Strokes equations as follows:

$$\frac{\partial}{\partial t}\left(\rho\vec{V}\right) + \nabla\left(\rho\vec{V}\vec{V}\right) = \rho\vec{g} - \nabla \mathrm{P} + \mu\nabla^2\vec{V} \tag{1.2}$$

ρ = Density

$\vec{V}$ = Velocity

$\vec{g}$ = Gravity

P = Pressure

μ = Viscosity

In the low-speed aerodynamics applications (less than 130m/s) the density is effectively constant, to which will give rise to the incompressibility conditions. This can be expressed by the following equation:

$$\nabla\vec{V} = \frac{\partial u}{\partial x} + \frac{\partial v}{\partial y} + \frac{\partial w}{\partial z} = 0 \tag{1.3}$$

So on the basis of that the equation number (1.1) can be written as:

$$\rho\vec{V}.\nabla\vec{V} = \rho\vec{g} - \nabla\mathrm{P} + \mu\nabla^2\vec{V}, \nabla\vec{V} = 0 \tag{1.3}$$

2.4.2 Bernoulli equation

One of the most important equations in aerodynamics analysis is the Bernoulli equation. This equation is used to compare the values of velocities and the pressure difference between the two points in the flow. Figure 2-5 shows an example of Bernoulli equation application.

The Bernoulli equation should be used taking into account several assumptions, one of the most significant being that air density does not change with pressure (air remains incompressible). Therefore, it can only be applied to subsonic situations.

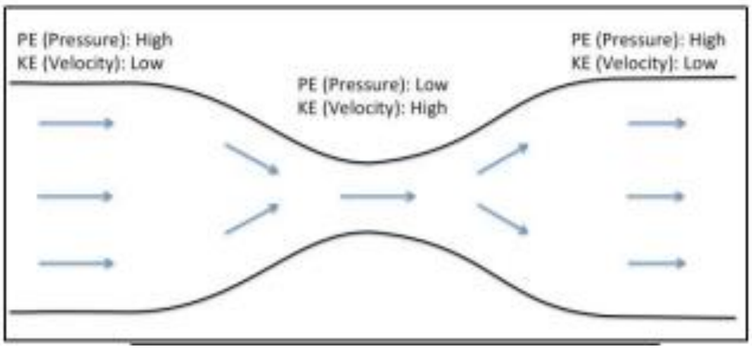

Figure 2-5 The venture meter

$$P_1 + \frac{1}{2}\rho V_1^2 + \rho g h_1 = P_2 + \frac{1}{2}\rho V_2^2 + \rho g h_2 \tag{1.4}$$

ρ = Density

V = Velocity

g = Gravity

h = height

So, on the **usual** car speed the air density is constant which is at the usual car speed for example below than 133 m/s. The last equation number can be written as follows:

$$\frac{P_1}{\rho}+\frac{V_1^2}{2}=\frac{P_2}{\rho}+\frac{V_2^2}{2} \tag{1.5}$$

This equation explains the pressure difference on the two points of the fluid. So as a result

$$\frac{P}{\rho}+\frac{V^2}{2}= Constant \tag{1.4}$$

2.5 Turbulence models for automotive applications

In another research, (Tastan, 2011) compared the reliability and performance of turbulence models used in CFD software to determine the aerodynamic feature over passenger cars. The geometry adopted in the simulations were based on a BMW 3-series passenger car, in 1/6 scale. The Catia CAD software was employed to generate the vehicle in IGES format. Afterwards, the geometry was imported into Gambit software and the surface meshing was created. The Tgrid Software concluded the volume meshing process. The same geometry had been studied in wind tunnel by (Aka, 2003), and his results were the experimental reference for (Tastan, 2011).

The researcher ran the CFD simulations in the ANSYS fluent software, where the reliability and performance of seven turbulence models were tested: (i) Spalart-Allmaras, (ii) Standard $k-\varepsilon$, (iii) RNG $k-\varepsilon$, (iv) realizable $k-\varepsilon$, (v) Standard $k-\omega$, (vi) SST $k-\omega$, and (vii) Reynolds Stress Model. The results were expressed by drag and pressure coefficients, streamlines, velocity and pressure distributions in different positions in the symmetry plane.

2.5.1 Standard $k-\varepsilon$ model

Drag results were not acceptable. The C_D was overestimated for 5 m/s and 9m/s about 35% and 10%, respectively, and it was underestimated for high velocities (21 m/s and 25 m/s) about 5% and 9% respectively. Pressure coefficient results are on the average of the other models except for one tested point, where it presented the most inaccurate C_p result obtained among other models: difference of 66% from experimental reference. General flow pattern around the car is predicted unrealistically. In the wake region, no vortex was fully observed, neither separation or vortex formation were observed at the sides of the car. Computing time and memory usage of this model was good. In fact, in terms of computational cost, this model was very economical compared to other models.

2.5.2 RNG $k - \varepsilon$ model

Drag results were on the average of the other models. This model was the most accurate in terms of general trend of $C_p$variation. Pressure coefficients at challenging points were relatively accurate. The general flow pattern around the car was predicted realistically. Two counter rotating vortices were observed at the wake region, which are typical for fastback/notchback car models. Likewise, two local separation and reattachment zones were observed at the sides of the car. Furthermore, separated flow on the rear window was detected at lower velocities. This model was one of the most economical models with regards to computational cost.

2.5.3 Realizable $k - \varepsilon$ Model

The accuracy of drag prediction was under the average of the other models. Pressure coefficient results were on the average of other models. Like other models, pressure is not detected. The general flow pattern around the car was predicted realistically. Computational cost of this model was a bit higher than those of the other $k - \varepsilon$ models. Despite higher computational cost, this model does not excel RNG $k - \varepsilon$ model.

2.5.4 Standard $k - \omega$ model

Regarding drag force, this model gives the most accurate results. For velocities between 13 and 25 m/s, the error in C_D was under 2%. Pressure distribution was relatively accurate. When compared to the other models, this turbulence model predicted the most accurate pressure coefficient at the rear-end edge. However, the wake vortex predicted was much stronger and the recirculation region at the wake was larger. A tiny vortex formation was observed at the beginning of the windshield due to local separation bubble. Flow at the sides was predicted as similar to other models, computational cost was higher than $k-\varepsilon$ models, but this model outshines $k-\varepsilon$ models in terms of overall results

2.5.5 SST $\boldsymbol{k-\omega}$ model

Drag results are on average of the other models similarly to the pressure coefficient results. The prediction of the general flow pattern around the car was realistic. Contribution of side flow separation to recirculation region at wake was predicted as much stronger compared to other models. In the view of computational effort, this model was the most expensive two-equation turbulence model. Nevertheless, the computational time was not very different from the average value of other two-equation models.

2.5.6 Reynolds stress model

The drag results were on the average of the other models, as well as the pressure coefficient results. The general flow pattern around the car was predicted realistically. A little vortex formation inside separation bubble was observed at the beginning of the windshield. Also, separated flow on the rear window was observed at lower velocities. The separation at the rear side edge of the car was predicted to happen earlier, in contrast to standard $k-\omega$, Spalart-Allmaras and $k-\varepsilon$ models. The RSM turbulence model was the most time and memory consuming. However, it has no clear advantage over $k-\omega$ models.

2.5.7 Spallart-Almaras Model

The most inaccurate drag results were obtained with this turbulence model. The general flow pattern around the car was predicted unrealistically. The prediction of the wake region was very poor, and it did not capture any vortex. In addition, no separation bubble was noticed at the sides of the car. This was the most economical turbulence model tested in this study, and the computational time is much less than the average of other models

2.6 Meshing

The meshing process has a significant impact on the CFD simulation, especially in drag and lift prediction. In the automotive perspective, there are many options to perform a good investigation of mesh optimization, aiming at better accuracy in drag prediction of ground vehicle shapes.

In this research the meshing convergence is be made by means of a GCI study.

2.6.1 Grid Convergence Index (GCI)

The examination of the spatial convergence of a simulation is a straight-forward method for determining the ordered discretization error in a CFD simulation (Roache, 1998). The method involves performing the simulation on two or more successively finer grids. The term grid convergence study is equivalent to the commonly used term grid refinement study.

As the grid is refined (grid cells become smaller and the number of cells in the flow domain increase) and the time step is refined (reduced) the spatial and temporal discretization errors, respectively, should asymptotically approaches zero, excluding computer round-off error.

The process consists in the following steps:

Firstly, should be create three successively finer grids, each one should have the half of the space cells compared with the other (that is r = 2, r is the refinement ratio)). This analysis is very difficult considering unstructured meshes, is necessary to know what regions are more relevant to the flow and prioritise the refinement at this region. A CFD simulation should be performed for each mesh to obtain the result.

Through the normalized grid space and the result of interest (for example drag coefficient), the order of convergence can be found by:

$$p = \frac{ln\left(\frac{f_3 - f_2}{f_2 - f_1}\right)}{\ln\text{ (r)}} \tag{1.5}$$

$f_{1,2,3}$ = Are the resultd of three simulations

r = refinement ratio

After that Richardson extrapolation should be applied using the two finest grids to obtain an estimate of the result of interest at zero grid spacing, by the following equation:

$$f_{h=0} = f_2 + \frac{(f_1 - f_2)r^p}{r^p - 1} \tag{1.6}$$

The grid convergence index for the fine grid solution can now be computed. A factor of safety of **FS=1.25** is used since three grids were used to estimate **p**. The GCI for grids 1 and 2 is:

$$GCI_{12} = FS\frac{\left|\frac{(f_1 - f_2)}{f_1}\right|}{(r^p - 1)} * 100\% \tag{1.7}$$

The GCI for grids 2 and 3 is:

$$GCI_{23} = FS\frac{\left|\frac{(f_2 - f_3)}{f_2}\right|}{(r^p - 1)} * 100\% \tag{1.8}$$

After that, it is recommended to check if the solutions were in the asymptotic range of convergence, this can be made by:

$$\frac{GCI_{23}}{r^p * GCI_{12}} \tag{1.8}$$

which is approximately one and indicates that the solutions are well within the asymptotic range of convergence.

2.7 Multi-Objective Optimization (MOO)

Multi-objective optimization is an area of multiple criteria decision making hat is concerned with mathematical optimization problems involving more than one objective function to be optimized simultaneously. Multi-objective optimization has been applied in many fields of science, including engineering, economics and logistics where optimal decisions need to be taken in the presence of trade-offs between two or more conflicting objectives. Minimizing cost while maximizing comfort while buying a car and maximizing performance whilst minimizing fuel consumption and emission of pollutants of a vehicle are examples of multi-objective optimization problems involving two and three objectives, respectively. In practical problems, there can be more than three objectives

For a nontrivial multi-objective optimization problem, no single solution exists that simultaneously optimizes each objective. In that case, the objective functions are said to be conflicting, and there exists a (possibly infinite) number of Pareto optimal solutions. A solution is called nondominated, if none of the objective functions can be improved in value without degrading some of the other objective values. Without additional subjective preference information, all Pareto optimal solutions are considered equally good.

Figure 2-6**Error! Reference source not found.** shows an example of a Pareto frontier (in red), the set of Pareto optimal solutions (those that are not dominated by any other feasible solutions). The boxed points represent feasible choices, and smaller values are preferred to larger ones. Point C is not on the Pareto frontier because it is dominated by both point A and point B. Points A and B are not strictly dominated by any other, and hence do lie on the frontier.

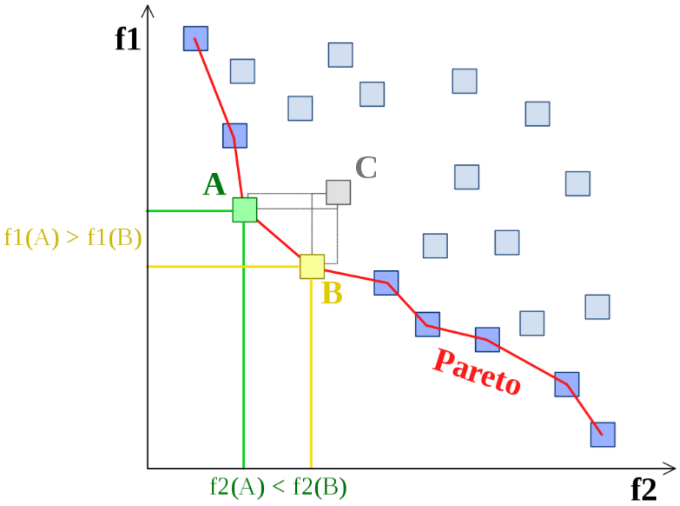

Figure 2-6 Example of Pareto frontier, in a Multi-objective optimization (https://en.wikipedia.org/wiki/Multi-objective_optimization)

In a Multi-Objective optimization analysis, there are some options of algorithms that can be used to find the best solution. Some of these algorithms will be presented in this dissertation.

2.7.1 NSGA-II

Non-dominated sorting algorithms (NSGA-II) are in general computationally demanding, especially in case of very large populations, since the identification of individuals belonging to the first non-dominated front requires the comparison of each solution with every other solution. However, NSGA-II implements a smart non-dominated sorting strategy which requires much less computations (Deb et al, 2000). A domination count is computed for each solution: those with domination count 0 belong to the first front. Then the domination count of all remaining dominated solution is reduced by 1 and those resulting with domination count 0 are classified to the second front. This procedure is repeated until all designs are sorted.

Maintaining population diversity is an important prerogative of genetic algorithms. The classic sharing function approach is essentially based on the calculation of the proximity measure between pairs of individuals in a population. This requires significant computational effort and its performance is highly dependent on the value of sharing parameters that must be set by the user. NSGA-II implements the crowding distance approach, which guarantees the diversity and spread of solutions on the Pareto front with a suitable parameter-less niching technique. This approach estimates the density of solutions in the objective space and uses a crowded-comparison operator, which guides the selection process towards a uniformly spread-out Pareto front.

2.7.2 FAST

FAST is an optimization algorithm combining real and Response Surface Method (RSM) based (virtual) optimization strategies. Both real and virtual optimization are performed by one of the evolutionary or heuristic algorithms for solving single and multi-objective problems (Rigone, 2014).

Designs generated by the FAST algorithm are exchanged between its real and virtual optimizers at each generation, increasing their robustness and improving convergence. The new designs added to the FAST database, whether coming from the real or the virtual optimization, are actively used both to improve the accuracy of the trained RSMs and to enrich the population of the real optimizer.

The Fast optimization algorithm performs in parallel both the real and the virtual optimization the mostly common algorithms used are MOGA-II, NSGA-II, ES, MOSA, ARMOGA, MOPSO and Simplex.

2.7.3 MOGA

MOGA-II is a version of the multi-objective genetic algorithm hat uses a smart and efficient multi-search elitism which can preserve excellent (Pareto or non-dominated) solutions without converging prematurely to a local optimum. Elitism improves the convergence of the algorithm and ensures that the fitness of each new generation is greater than the fitness of the parent generation (Aittokoski and Miettinen, 2008).

If elitism is not used, each next generation is computed only using the designs from the parent generation. However, in this case the probability that a design is subject to the Selection and the Classical Cross-Over operations is proportional to its fitness function value, for example the higher the fitness of a design, the greater the probability that it will be selected for these operations.

2.7.4 MOGT

The Multi-Objective Game Theory (MOGT) optimization algorithm is based on the Game Theory, which was mathematically formulated by J. F. Nash in the early 50s and found its first application in economics, in particular to solve problems concerning the decisions that have some effect on different and often competitive fields. MOGT is particularly efficient with highly constrained and non-linear problems (Clarich et. al., 2004).

This algorithm is based on a competitive game between players. There are as many players as optimization problem objectives and each player has the task of optimizing the objective assigned to them. The number of objectives cannot be greater than the number of input variables.

Even though the Nash equilibrium does not necessarily lie on the Pareto front, the convergence rate of MOGT is quite high. It can be therefore used to find a good set of not-dominated solutions with a low number of computations (if compared to other multi-objective algorithms), and use those solutions to initialize, for example, a genetic algorithm accelerating the search of the true Pareto.

3 Methodology

To achieve the aim proposed for this research, appropriate mathematical and computational techniques are needed. In this chapter, the description of such tools (numerical models) used to perform the CFD simulations and geometry optimisation, as well as the CAD geometry generation and parametrisation, are presented. The specific modelling techniques adopted are discussed with respect to both reliability and quality of the numerical solutions. These methods are also used to develop an understanding of the rear diffuser performance.

3.1 Governing equations and turbulence modelling

The physics of fluid flow can be described by using a set of equations which are the governing equations. These equations are regarded as the Navier-Stokes (N-S) equations (shown in section 2.4.1). To solve the complex flow phenomenon by using the N-S equations, a mathematical transformation is needed, starting from the basic continuity and momentum equations. Further details about the RANS models and the turbulence treatment, which are used in this project, will also be introduced.

3.1.1 Nature of turbulence

As a very common phenomenon in the natural world, turbulence has become the focus of many observers, from the outer space nebulae to the atmospheric clouds, from the terrible hurricane to the smoke rising from a cigarette. In engineering, engineers concentrate on the influence of turbulent flow which is generated by man-made applications, such as boundary layers over wings and wakes from transportation.

Turbulence is widely believed as a flow which is characterized by apparently random and chaotic three-dimensional vortices. In fact, there are usually three distinct regimes for most of the external fluid motions: laminar flow, transitional flow and fully developed turbulent flow. Turbulence occurs when the inertial energy is much greater than the viscous dampening forces in a small or a larger transition region which usually comes after the laminar flow. There are three essential aspects of turbulence: Initial perturbation, vortex stretching and instability. Turbulence is initiated by wave like instabilities in shear layers. Random fluctuations are amplified by inertial forces, they become unstable and interact to become three-dimensional. There is then a mutual interaction of many vortices leading to entanglement and deformation.

3.1.2 Approximate techniques for solving the Navier Stokes Equation

As all fluid dynamics is based on the universal law which is the Navier-Stokes Equations, the key issue of CFD is to solve it with the minimum of complexity while describing the information of physical phenomena as accurately as possible.

To achieve this main aim, Ferziger (1999) classified the flow simulation into follow categories:

1. Direct Numerical Simulation (DNS);
2. Large Eddy Simulation (LES);
3. Detached Eddy Simulation (DES);
4. Reynolds-Averaged Navier-Stokes Equations (RANS).

Considering the Reynolds Number (around $3x10^6$) order involved in this case, flow features, and the low computational cost considering that will be made many numerical simulations during optimization process, the RANS is precise enough to solve the flow with a cheap computational cost compering with other techniques. In this research project, we will employ Reynolds- Averaged Navier-Stokes Equations (RANS) simulations. Therefore, the RANS equations will be described in detail in the following sections.

3.1.3 Direct Numerical Simulation (DNS)

DNS is a direct approach that solves the N-S equations only by numerical discretisation. This means the results from DNS will be the closest to the real physics flow phenomena, because the whole range of scales of turbulence is resolved directly without any turbulence models. However, this brings a great challenge too. All of the scales including the smallest dissipation, which is well-known as Kolmogorov scale would be resolved in the finest level of mesh. In fact, there is proof that a three- dimensional DNS requires the mesh points that scales with the 9/4 power of Reynolds Number. Additionally, the time steps required is also a power of Reynolds Number because the N-S equations must be integrated in time. As a result, the whole computational operation for DNS goes proportionally to the third power of Reynolds number.

For these reasons, even at low Reynolds Number cases, the requirements of the computational cost would be beyond the capability of the most powerful computers. This has limited the DNS to very simple geometries such as flat a plate at low Reynolds Numbers.

3.1.4 Large Eddy Simulation (LES)

As DNS aims to resolve the full range of physical scales in the flow filed, LES only focuses on representing the largest resolved scales, where the grid size is considerably larger than the Kolmogorov scale. For those unresolved small scales, the so-called subgrid scale (SGS) is often taken into account by using a subgrid scale model. Although the computational cost is significantly lower than DNS, LES is still expensive and relies highly on high computer performance.

3.1.5 Detached Eddy Simulation (DES)

To tackle the difficulties of using the standard LES in near boundary region, a modification of RANS model was introduced as SGS model until the grid is fine enough for LES. This hybrid technique is so-called DES and combines the best aspects of both RANS and DES methodologies into a single strategy.

3.1.6 Reynolds averaged Navier-Stokes Equation (RANS)

A very widely used approach for turbulent flow simulation in industry for engineers is a set of time-averaged equations, which is called Reynolds-Averaged Navier-Stokes (RANS) equations. The time-averaged solution for turbulent flow was introduced by Reynolds. This concept is based on replacing all the fluctuant variables such as velocity and pressure with time-averaged part and a fluctuating part. As presented in the following equation:

$$u_i = \overline{u_\iota} + u_i' \tag{2.14}$$

By applying the time average on the Navier-Stokes equations, the Reynolds-averaged Navier-Stokes equations (RANS) (Ferziger, 1997) can be derived as:

$$\rho\frac{\partial\overline{u_i}}{\partial t}+\rho\frac{\partial\overline{u_i u_j}}{\partial x_j}=\frac{\partial P}{\partial x_i}+\rho v\frac{\partial^2\overline{u_i}}{\partial {x_j}^2}-\rho\frac{\partial\tau_{ij}}{\partial x_j} \tag{2.15}$$

In the equation 2.16, the additional stresses$\tau_{i,j}$, which are called the Reynolds Stress Tensor are inducted to get rid of the cancellation of the random fluctuations.

$$\tau_{ij}=-\rho\overline{u_i u_j}=\begin{pmatrix}-\rho\overline{u'^2} & -\rho\overline{u'v'} & -\rho\overline{u'w'}\\ -\rho\overline{v'u'} & -\rho\overline{v'^2} & -\rho\overline{v'w'}\\ -\rho\overline{w'u'} & -\rho\overline{w'v'} & -\rho\overline{w'^2}\end{pmatrix} \tag{2.16}$$

A set of unknown variables are introduced for solving the cancellation of the fluctuations, which is the well-known closure problem. In order to collect sufficient equations for the closure problem, some different turbulence models are used as a connection between the time-averaged and the fluctuating part. In this dissertation, only the SST k-ω model is used.

The RANS equations are not as powerful as other approaching simulations such as the Large Eddy Simulation (LES) for the large-scale turbulent motions or the Direct Numerical Simulation (DNS), which solves the equations directly for all turbulence scales. However, the users can get a fast, reasonable solution via the RANS equations. Depending on the Reynolds number of the applications this approach is accurate enough and the computational cost of the simulation is much lower when compared to the other approaches.

According to Guilmineau (2007), The prediction of massively separated flows, such as flows encountered in stall control, is a difficult task. Although large eddy simulation (LES) approaches may be more suitable for such flows, the present approach relies on solving Unsteady Reynolds averaged Navier-Stokes (URANS) equations. Indeed, the computational cost of LES approaches is still prohibitive for high Reynolds numbers, and the URANS approach of greatly reduces the computational effort. If the mean flow is steady, the governing equations will not contain time derivatives and a steady-state solution can be not too expensively obtained (Kalyan and Paul, 2013). The URANS equations are as follows:

$$\frac{\partial(\rho u_i)}{\partial x_i}=0 \tag{2.17}$$

$$\rho\frac{\partial(u_i)}{\partial t}+\rho\frac{\partial(u_i u_j)}{\partial x_j}=\frac{\partial p}{\partial x_j}+A+B \tag{2.18}$$

$$A=\frac{\partial\left[\mu\left(\frac{\partial u_i}{\partial x_j}+\frac{\partial u_j}{\partial x_i}-\frac{2\delta_{ij}}{3}\frac{\partial u_i}{\partial x_i}\right)\right]}{\partial x_j} \tag{2.19}$$

$$B = -\rho \frac{\partial\left(u_i u_j\right)}{\partial x_j} \tag{2.20}$$

This approach is generally adopted for all practical engineering calculations and is used with turbulence models.

3.2 Turbulence models based on RANS

There is not a universal model that could successfully model all the turbulent flow. So choosing an appropriate turbulence model becomes a key issue in most CFD simulations. Depending on the turbulence, the grid size and the computational performance, different turbulence models present diverse results. Some models are presented below:

- Spalart-Allmaras (S-A) Turbulence Model
- Wilcox k-ω Model
- Shear Stress Transport (SST) k-ω Model

This thesis uses only one model, we will focus only on k-ω SST Model. This model was chosen because the formulation is very consistent. Considering the use of a *k-ω* formulation in the inner parts of the boundary layer makes the model directly usable all the way down to the wall through the viscous sub-layer, hence the SST *k-ω* model can be used as a Low-Re turbulence model without any extra damping functions. SST *k-ω* model has a good behaviour in adverse pressure gradients and separating flow (Karim et al. 2009).

3.2.1 Shear Stress Transport (SST) *k-ω* Model

By pointing out the importance of turbulent shear stress, Menter (1994) refined the original Wilcox *k-ω* model. Two transport equations for the kinetic turbulent energy *k* and specific dissipation rate *ω* are introduced in the SST model. However, based on Bradshaw's shear stress transport assumption, the eddy viscosity was redefined as:

Kinematic eddy viscosity

$$v_t = \frac{a_1 k}{\max\left(a_1 \omega, S F_2\right)} \tag{2.17}$$

Turbulence kinetic energy

$$\frac{\partial k}{\partial t} + U_j \frac{\partial k}{\partial x_j} = P_k - \beta^* k\omega + \frac{\partial}{\partial x_j}\left[(\nu + \sigma_k \nu_T)\frac{\partial k}{\partial x_j}\right] \tag{2.18}$$

Specific dissipation rate

$$\frac{\partial \omega}{\partial t} + U_j \frac{\partial \omega}{\partial x_j} = \alpha S^2 - \beta\omega^2 + \frac{\partial}{\partial x_j}\left[(\nu + \sigma_{\omega_1}\nu_T)\frac{\partial \omega}{\partial x_j}\right] + 2(1 - F_1)\sigma_{\omega_2}\frac{1}{\omega}\frac{\partial k}{\partial x_i}\frac{\partial \omega}{\partial x_i} \tag{2.19}$$

Where the closure coefficients and auxiliary relations are:

$$F_2 = tanh\left[\left[max\left(\frac{2\sqrt{k}}{\beta^*\omega y}, \frac{500\nu}{y^2\omega}\right)\right]^2\right] \tag{2.20}$$

$$P_k = min\left(\tau_{ij}\frac{\partial U_i}{\partial x_j}, 10\beta^* k\omega\right) \tag{2.21}$$

$$F_1 = tanh\left\{\left[min\left[max\left(\frac{\sqrt{k}}{\beta^*\omega y}, \frac{500\nu}{y^2\omega}\right), \frac{4\sigma_{\omega_2}k}{CD_{k\omega}y^2}\right]\right]^4\right\} \tag{2.22}$$

$$CD_{k\omega} = max\left(2\rho\sigma_{\omega_2}\frac{1}{\omega}\frac{\partial k}{\partial x_i}\frac{\partial \omega}{\partial x_i}, 10^{-10}\right) \tag{2.23}$$

$$\alpha = \frac{5}{9}, \beta = \frac{3}{40}, \beta = \frac{9}{100}, \sigma_k = 0.85, \sigma_{\omega_1} = 0.5, \sigma_{\omega_2} = 0.856 \tag{2.24}$$

The SST k-ω model is closely related to the standard Wilcox k-ω model but has an improved predictive accuracy for flows with an adverse pressure gradient. It is, thus, suitable for flows with strong separation and has proven to allow maximum lift prediction. However, since the model depends on global minimum wall distances, computations for complex topologies may become very expensive.

3.3 Finite volume method (FV method)

The Finite Volume Method (FVM) is one of the most versatile discretization techniques used in CFD. Based on the control volume formulation of analytical fluid dynamics, the first step in the FVM is to divide the domain into several control volumes. The variables of interest are located at the centroid of each control volume. The next step is to integrate the differential form of the governing equations over each control volume. Interpolation profiles are then assumed in order to describe the variation of the concerned variable between cell centroids. The resulting equation is called the discretized or discretization equation. In this manner, the discretization equation expresses the conservation principle for the variable inside the control volume.

The most compelling feature of the FVM is that the resulting solution satisfies the conservation of quantities such as mass, momentum, energy, and species. This is exactly satisfied for any control volume as well as for the whole computational domain and for any number of control volumes. Even a coarse grid solution exhibits exact integral balances.

Consider a single partial differential equation in conservation form,

$$\frac{\partial u}{\partial t} + \nabla \cdot f(u) = 0 \tag{2.27}$$

where u is a conserved quantity and

$$f(u) = [f_1(u), \dots, f_d(u)] \tag{2.28}$$

is the flux integrating this over any volume V in R^{d}. If we integrate this equation, we get the integral form of the conservation law,

$$\frac{\partial}{\partial t}\int_V udV + \oint_{\partial V} f_i\, n_i ds \tag{2.29}$$

where the divergence theorem has been used to convert the divergence term to a surface integral over the surface $\partial\mathrm{S}$ and $(\mathrm{n}_1, \dots, \mathrm{n}_\mathrm{d})$ is the unit normal outward vector to $\partial\mathrm{S}$ the Equation (2.29) is the starting point for the finite volume method.

3.4 Optimization algorithm

A very important step in this thesis is the Multi-Objective Optimization of the car geometry. This analysis should be robust, accurate and unexpensive enough to make it possible to achieve a satisfactory result in a viable time, considering the CFD simulation time spent to simulate a car. As presented in section 1.1 there are different kinds of optimization algorithms. During the preliminary simulations (Ahmed body), we tested the four algorithms presented, to understanding which one is more indicated for the case. The FAST NSGA-II achieved a satisfactory result quicker and needed less simulations to form a Pareto frontier; because of that, this method was chosen to be used in the Car geometry optimization process.

FAST optimizers progress toward better solutions in an iterative way. FAST starts from the initial population definition. When Self-Initializing configuration mode is selected, the algorithm defines an internal DOE size, which corresponds to the initial population size. If no

DOE Table is provided, the algorithm automatically generates new designs as a DOE and evaluates them. If the DOE Table contains some designs, the algorithm evaluates them. If the provided DOE Table size is less than the internal DOE size, the algorithm generates new designs until the internal DOE size is reached. FAST evaluates the designs in the DOE Table which form the initial population. After the evaluation of DOE, the main loop of algorithm starts.

NSGA-II is a multi-objective optimization algorithm: it implements a fast and clever non-dominated sorting procedure and elitism for multi-objective search. Elitism is introduced storing all non-dominated solutions discovered so far, beginning from the initial population. A parameterless diversity preservation mechanism is adopted. Diversity and spread of solutions are guaranteed without the use of sharing parameters, since NSGA-II adopts a suitable parameterless niching approach. The crowding distance criteria is defined and used to rank the population in the objective space: a point having a higher average distance to other points in the set has a higher ranking. NSGA-II works with both discrete variables coded in binary format (as MOGAII) and continuous. For the last case a particular crossover and mutation operation for reproduction is performed based on a Deb probability function: a random value accordingly to this distribution defines the result, so a lower distribution index raises the probability to have a point different from the parents, and a higher value gives more probability to find parents.

3.5 CFD Analysis methodology

In order to accomplish the objectives proposed for this thesis, appropriate computational tools had to be chosen, taking into account the computational resources available and the synergy of the different disciplines involved. In this chapter, the methodology to use these tools in an accurate way will be presented. To achieve the goals, it was necessary to perform CFD and Optimization analysis, as well as the CAD geometry generation and parametrization. The software suites used were SolidWorks 2019 for CAD design and geometry treatment of the car model; ANSYS DesignModeler to prepare the CAD model for CFD simulation; ANSYS Meshing as integrated tool in the workbench was choose to create an accurate mesh; for the CFD simulation ANSYS Fluent was used; finally modeFRONTIER was chosen to work integrated with ANSYS Fluent to automate the CFD analyses and perform the optimization studies.

Specific modelling techniques, settings and simplifications adopted regarding both reliability and quality of the numerical solutions will be presented in this section. Firstly, it was necessary ensure the robustness of the overall features chosen and validate the CAD model, geometry treatment, numerical domain, mesh features, numerical setup (Turbulent model, solve method) and optimization method. To verify these features, the Ahmed body was used for a preliminary analysis and validation due to its low geometric complexity, and easiness to compare the numerical results witch experimental results.

Figure 3-1 shows the interaction between the pieces of software. It consists of an optimization loop where the modeFRONTIER controls the ANSYS Workbench, changing the geometric characteristics of the car (rear diffuser dimensions) to achieve the best performance (Minimize Lift and Drag).

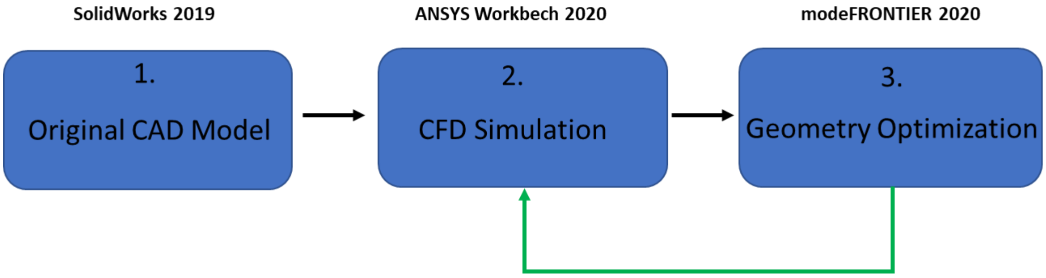

Figure 3-1 Loop of optimization diagram (Software's interaction)

3.5.1 CAD model from Solid works 2019

Solid Works was mainly used to create and prepare the geometries due the easiness in creating 3D CAD models. The car geometry that was analysed is close to the production shape, highly detailed within all areas. During the CFD treatment the necessary simplifications should be as few as possible. Their creation was predominantly carried out by surface-based CAD systems due to their complexity. Unfortunately, these do not guarantee closed surfaces.

On the other hand, volume-based modelling systems have the advantage of the outer surfaces being inherently closed. The eventual goal of expanding the typical vehicle model so that it includes such features as wipers, aerials, detailed underbody, and all under-hood components is a limitation of such systems. During the preparation for a flow simulation, a consistent definition of fully connected geometry has to be ensured. This first step comprises a cleaning-up of the CAD model and is totally independent of the subsequent method of simulation.

3.5.2 CFD Analysis in ANSYS Workbench 2020

The aerodynamic design of a car is an engineering problem where almost every car brand in automotive industry, and every team in automotive racing are challenged by, and the use of Computer-Aided Engineering (CAE) software has been the primarily choice in order to obtain reliable and efficient products as quick as possible.

ANSYS has been a widely known CAE software of virtual-prototyping and modular simulation system and was used to perform the CFD analyses presented in this thesis. Its advantages for this work relied on the fact that ANSYS Workbench platform offers specific modules to solve CFD very quick. Furthermore, it allowed the user to choose the level of analysis complexity, for each individual problem, with extensive settings variety. In Figure 3-2, an example project schematic process of a CFD parametrized analysis in ANSYS Workbench 2020 is shown.

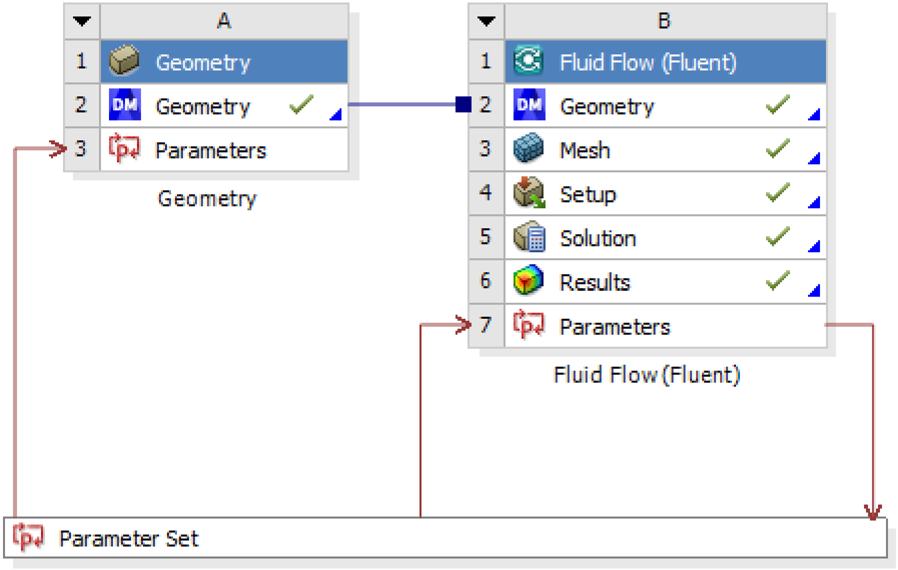

Figure 3-2 Project schematic in ANSYS Workbench.

ANSYS DesignModeler

The ANSYS DesignModeler application/module was designed to be used as a geometry editor of existing CAD models. The first geometries (CFD and CSM models) were done using SOLIDWORKS and imported to ANSYS DesignModeler as there was a specific Geometry Interface between them.

DesignModeler have specific resources necessaries to export a CAD model ready for CFD simulation. Basically, all domain features (virtual Wind tunnel) were designed in

DesignModeler, as well as the geometry parametrisation to make possible modeFRONTIER control the optimization loop, reducing drastically the time to achieve the best geometry.

ANSYS Meshing

ANSYS Meshing is an integrated module in Workbench, that provides general propose, high-performance, automated, intelligent meshing software which produces the most appropriate mesh for accurate, from easy, automatic meshing to highly crafted mesh. Methods available cover the meshing spectrum of high order to linear elements and fast tetrahedral and polyhedral to high-quality hexahedral and Mosaic.

For a typical car like shape, pressure or form drag is dominant over skin friction, so the accuracy of the drag and lift predictions are largely determined by the accuracy of the predicted static pressure distribution on the body. This pressure distribution is strongly affected by the locations of flow separation and reattachment. Therefore, it is important that the surface mesh resolves all relevant details of the geometry and satisfies the requirements of the physical models used in the simulation.

ANSYS Fluent

ANSYS Fluent is a commercial powerful CFD software tool, with well validated physical modelling capabilities that include all the fluid flow numerical simulation advantages. It provides numerical solutions using algorithms to solve fluid flow governing equations (Navier-Stokes equations), in order to simulate determined physical conditions. Motorsport was one of the first professional sports to adopt commercial CFD tools for competitive advantage because of its relative cheapness and scalable knowledge, relative to building further wind tunnels.

Combining both CAD and CFD tools, engineers could quickly evaluate and develop new design ideas without the requirement of costly prototype testing. However, such instrument has its own weaknesses. It is only a simulation of what could happen in the real world, and the numerical solution strongly depends on user-defined elements (mesh generation and turbulence modelling). Such modelling techniques have an important effect on the quality of the numerical solution, in particular for the prediction of flow separation (in smooth curved surfaces) and for the transition from laminar to turbulent flow at high-Reynolds number.

It is used across a wide range of CFD and multiphysics applications (model flow, turbulence, heat transfer and reactions) and in particular for air flow simulation over racing and passenger cars.

3.5.3 Geometry optimization modeFRONTIER

Improving product performance, quality and reliability while reducing time-to-market costs is a hard task. modeFRONTIER is software that provides engineering design process automation, optimization solutions and statistical analysis.

In this study modeFRONTIER was used to control the CFD simulation (Fluent) as from as automated process to guarantee the best result. CFD-based optimization refers to the computer-based optimization relying on evaluations obtained by computational fluid dynamics (CFD). Although the concept of CFD-based optimization is not new, the extremely high computational costs typically associated with the process still limit its applicability. CFD optimization typically starts from a fairly good design, which is achieved through an experience-based cut-and-try approach. Most published instances of CFD-O involve only regional optimization, without parameterizing the geometry.

One major challenge of CFD optimization is the automatic and robust looping, involving all steps shown in Figure 3-3 without human interference. In various published works, part of the optimization remained a manual process. For instance, the geometry was parameterized and updated in an automatic manner, but the grid was generated manually. In this thesis the optimization loop is made fully automatic using genetic algorithms to converge optimal solutions as quantified by objective functions.

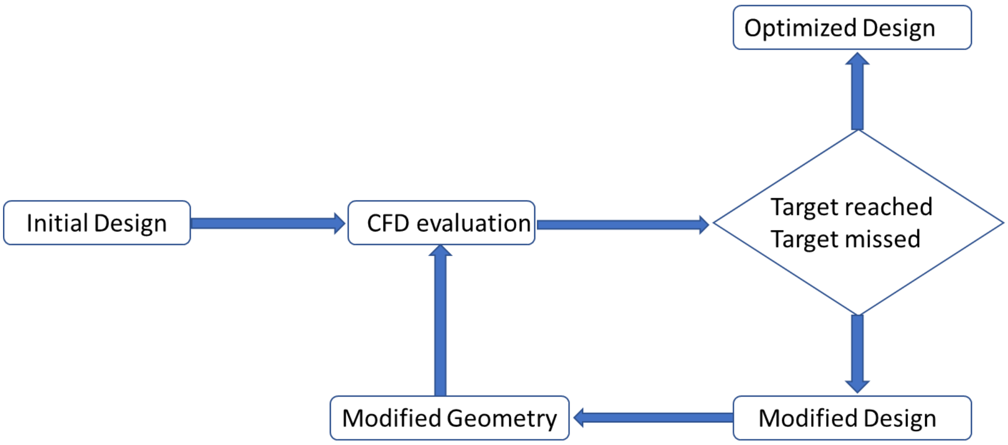

Figure 3-3 CFD-Based design process

3.5.4 Numerical simulation Set-up

In this section will presented a brief description of the main features associated with the set-up used in the numerical simulation like geometry, computational flow domain, turbulence model and boundary conditions.

3.6 Ahmed body

3.6.1 Numerical modelling

To develop the CFD simulation we considered an Ahmed Body model with the following geometric features: 1044 mm long, 327 mm wide and 288 mm high, 35° rear slant, ground distance of 50 mm (Figure 3-1). A single body domain of air was created surrounding the Ahmed body walls after subtracting it from the air enclosure, the body was suspended 50mm to the ground. The domain size was of $10L\times2L\times1.5L$ in the streamwise (y), spanwise (x) and normal (z) directions respectively, with L being the model length. The coordinate system adopted positive *"x"* in the longitudinal direction of the body, positive *"y"* in vertical direction (pointing to top the body) and positive *"z"* in the lateral direction (pointing to opposite side of the *xy* symmetrical plane). The center of the coordinate system was placed at the end of Ahmed body ($x = 0$ end of the model, $y = 0$ symmetry plane, $z = 0$ ground plane). As the body and flow are symmetrical, we considered only half model and created a symmetry plane (*xy* plane) that cuts through the entire domain. Figure 3-5 shows the entire domain.

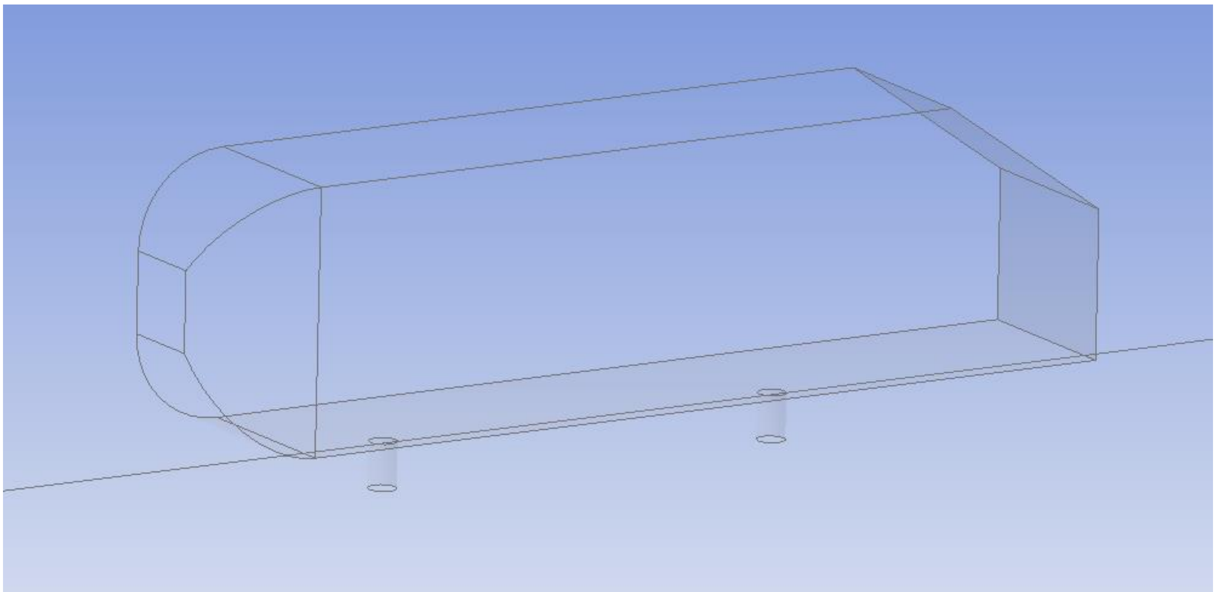

Figure 3-4 Ahmed body geometry

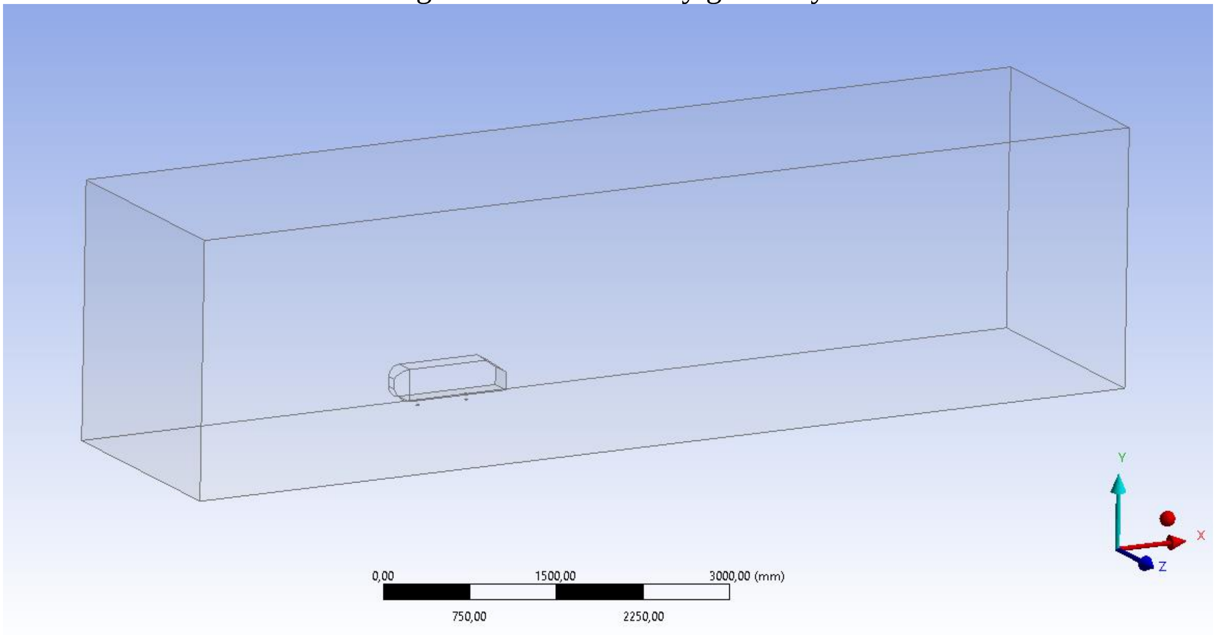

Figure 3-5 Computational domain of Ahmed body numerical simulation

For the grid refinement, we used a boxes strategy. This strategy is based on internal boxes created around the vehicle and in the wake region to explicitly control mesh size. This approach is a little bit more time consuming than other strategies like adaptation, but very accurate. A constant size of surface elements is applied to the box walls. It is possible to see the refinement zones in Figure 3-6

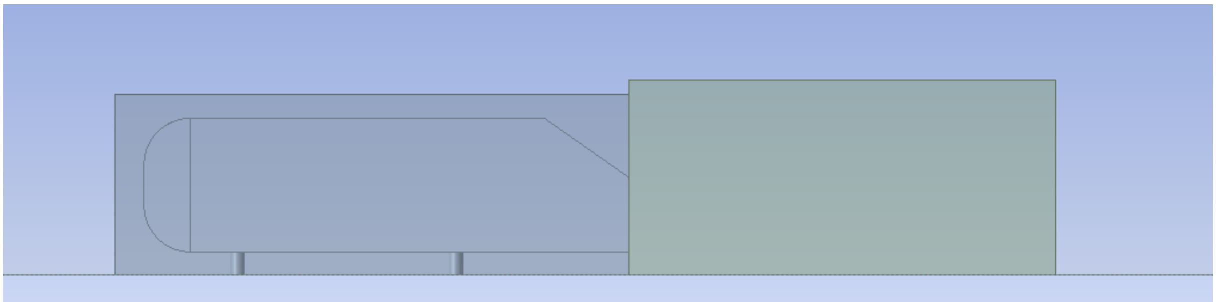

Figure 3-6 Refinement boxes for local grid refining (Ahmed body)

The grid hexahedral elements were used in the grid on order to capture the high gradients at the boundary layers. Layered elements provide good alignment with the flow near wall boundaries.

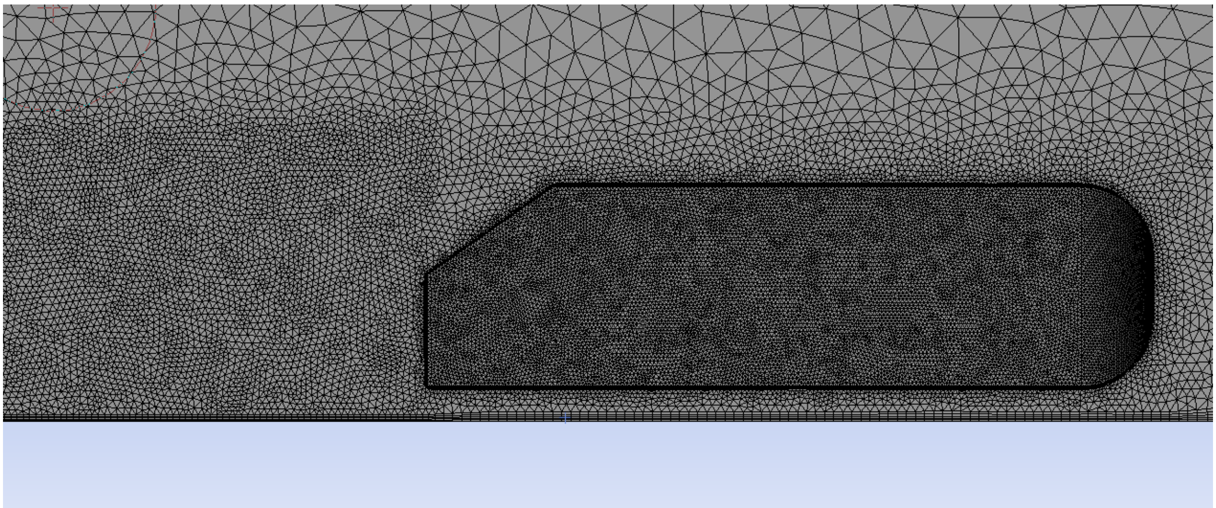

Figure 3-7 Ahmed body mesh discretization

Details of the unstructured mesh are as follows:

- Relevance centre; coarse,
- Smoothing; high,
- Transition; slow,
- Initial size seed; Active assembly,
- Min. Size; 5 mm,
- Max. Size; 100 mm,
- Advanced Size function; Proximity and Curvature.
- Inflation Layer method of first aspect ratio of 5, growth rate of 20% of 5 layers was used.

With respect to the Fluent solution methods the pressure-velocity coupling scheme selected was the Coupled algorithm. The spatial discretization schemes employed are summarized in Table 3-1. Numerical simulations were performed to check the influence of different spatial discretization's schemes on the numerical solution, and changes were insignificant. The final selection was based on specific recommendations from literature (Lanfrit, 2005). Solver settings and solutions methods presented here were applied in all CFD simulations performed for this dissertation. The turbulence model adopted was k-ω SST.

Table 3-1 Spatial discretization schemes selected for the numerical analyses.

Gradient	Least Squares Cell Based
Pressure	Second Order
Momentum	Second Order Upwind
Turbulent Kinetic Energy	Second Order Upwind
Specific Dissipation Rate	Second Order Upwind
Transient Formulation	Second Order Implicit

Imposing boundary conditions to the numerical wind tunnel walls and Ahmed body boundaries is an important step and should be done with care. Fluent offers a wide variety of boundary conditions, and its specification, in general, should be geared as close as possible to the measurement conditions in the wind tunnel. In the majority of cases, flow velocity and turbulent intensity of the wind tunnel are known. The boundary conditions assigned are indicated in Table 3-2.

Table 3-2 Boundary conditions settings for the numerical analyses (** just to compare the results of Ahmed body simulation with experimental data, Wall boundary condition was employed at the Wind tunnel down.)

Wind tunnel inlet	Velocity inlet (40 m/s)
Wind tunnel outlet	Pressure outlet
Wind tunnel top and side	Symmetry
Wind tunnel down	Velocity inlet (40 m/s) **
Wind tunnel interior	Interior
Ahmed Body	Wall (no-slip condition)
Specification Method	Intensity and Viscosity Ratio
Turbulent Intensity (%)	5
Turbulent Viscosity Ratio	10

3.6.2 Mesh convergence

To establish the accuracy of the CFD solution, and to keep the computational costs low, the Grid refinement was defined by a GCI study. The grid convergence study was performed by developing three different meshes: a coarse, a medium, and a fine grid. For all three different meshes of the Ahmed body, the drag and lift coefficients were calculated and employed in the GCI study. The refinement ratio used was r=2; that is, each mesh should have the half of grid space the other coarser mesh. Details of the process are show in section 4.2.

This approach is very good way to understand what level of refinement is needed to achieve a good result in terms of accuracy and computational time. The correct mesh refinement is so important due the number of simulations made during the optimization process.

3.6.3 Geometry optimization

To establish a loop of geometry optimization it was necessary to create a parametrized version of the Ahmed body geometry. The parametric geometry was created in the ANSYS Design Modeler.

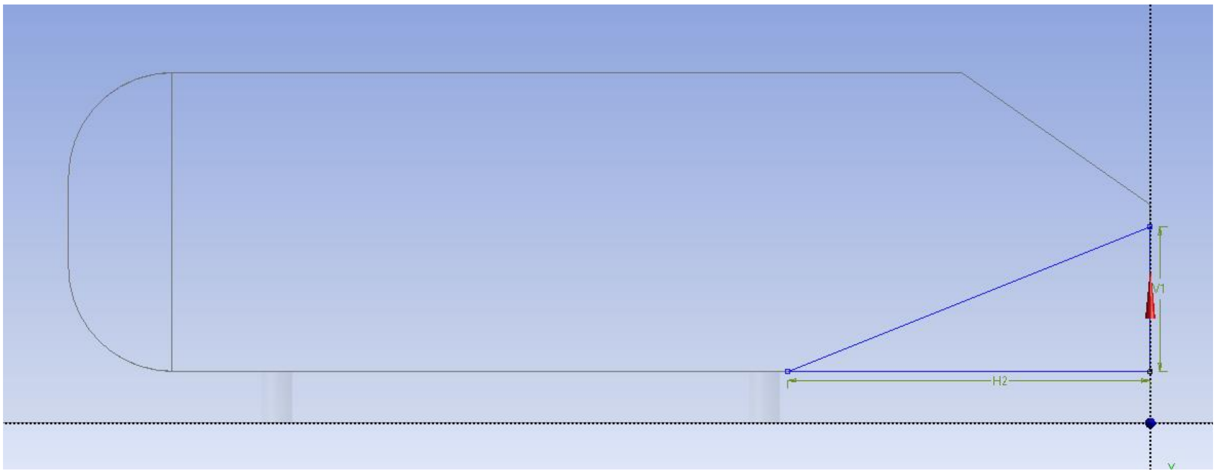

Figure 3-8 Ahmed body parametric geometry

The input parameters that will used during the optimization process was Height and Length of the rear diffuser (Figure 3-8). This geometry was used in the optimization loop, with the same numerical simulation features, that is, mesh density, boundary conditions, spatial discretization, turbulence model and etc.

The structure of the optimization loop is presented in Figure 3-9. The two green icons at top represent the input parameters (Height and Length), the central node contain the ANSYS Workbench project. The node at the left-hand side represents the optimization algorithm setup. The node at the right-hand side is the logic end it indicates respectively successful and unsuccessful design evaluations according to a given condition. The two blue nodes below the ANSYS project represent the output parameters (drag coefficient and lift coefficient), Connected below these are the nodes responsible to determine the objective, in this case the objective is to minimize the output parameters.

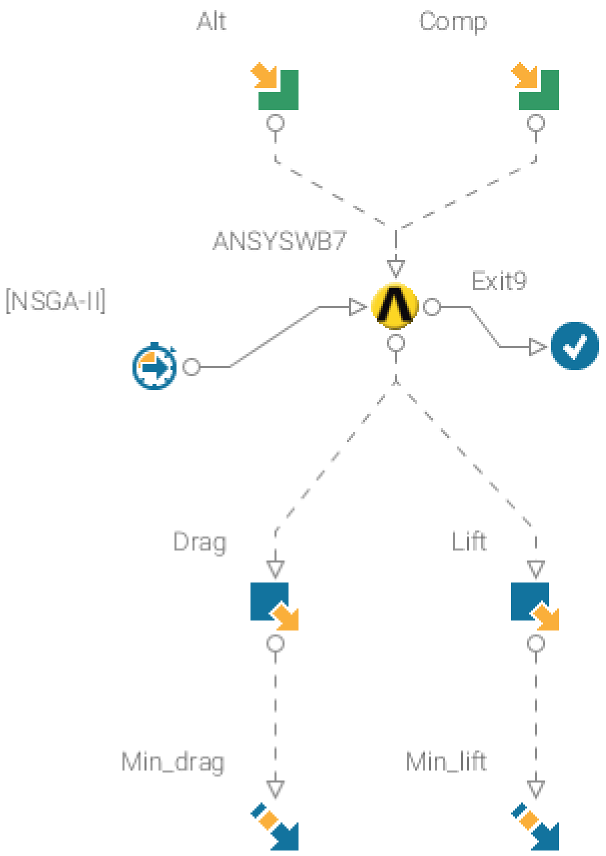

Figure 3-9 Loop of optimization scheme

3.7 Car Geometry

3.7.1 Numerical modelling

To perform a CFD simulation with a Car we used a “smooth” car geometry, the 3d cad model was obtained from a site that provides 3d model for download (https://grabcad.com/).

Due to the need to perform a quicker and accurate simulation during the optimization, some simplifications were made, like removing wheel and mirrors. This is a full-scale model with the following geometric features: 4710 mm long, 909 mm wide and 1247 mm high. A single body domain of air was created surrounding the Car walls. After subtracting it from the air enclosure, the body was suspended 60 mm to the ground. In rear diffuser studies the distance to the ground play a very important role, so many studies were made to test different distances to the ground, as the focus of this dissertation is to optimize the car geometry, we just used 60 mm for the ground clearance (Figure 3-10). The domain dimensions were $8L$x$3L$x$2.5L$ in the streamwise (y), spanwise (x) and stream-normal (z) directions, with L being the car length. This domain was chosen to make time simulation time not so long, without loosing accuracy. The coordinate system adopted positive *"x"* in the longitudinal direction of the car, positive *"y"* in vertical direction (pointing to the top of the body) and positive *"z"* in the lateral direction (pointing to opposite side of the *xy* symmetrical plane). The center of the coordinate system was placed at the middle of the Car model ($x = 0$ middle of the model, $y = 0$ symmetry plane, $z = 0$ ground plane). As the Car and flow are symmetrical, we considered only a half model and created a symmetry plane (*xy* plane) that cuts through the entire domain. Figure 3-11 shows the entire domain.

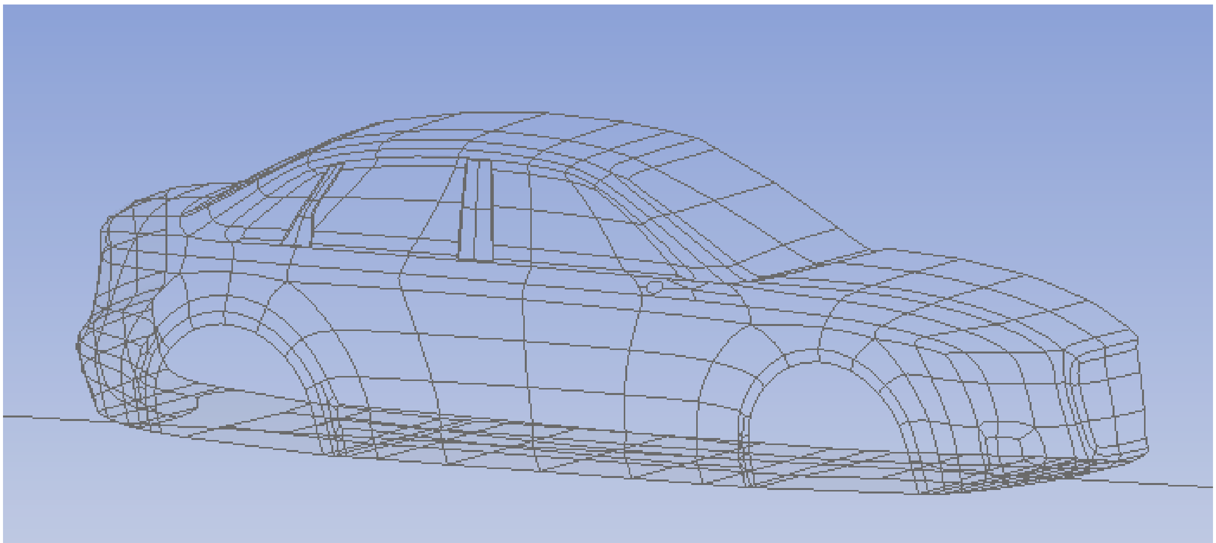

Figure 3-10 Full-scale car model.

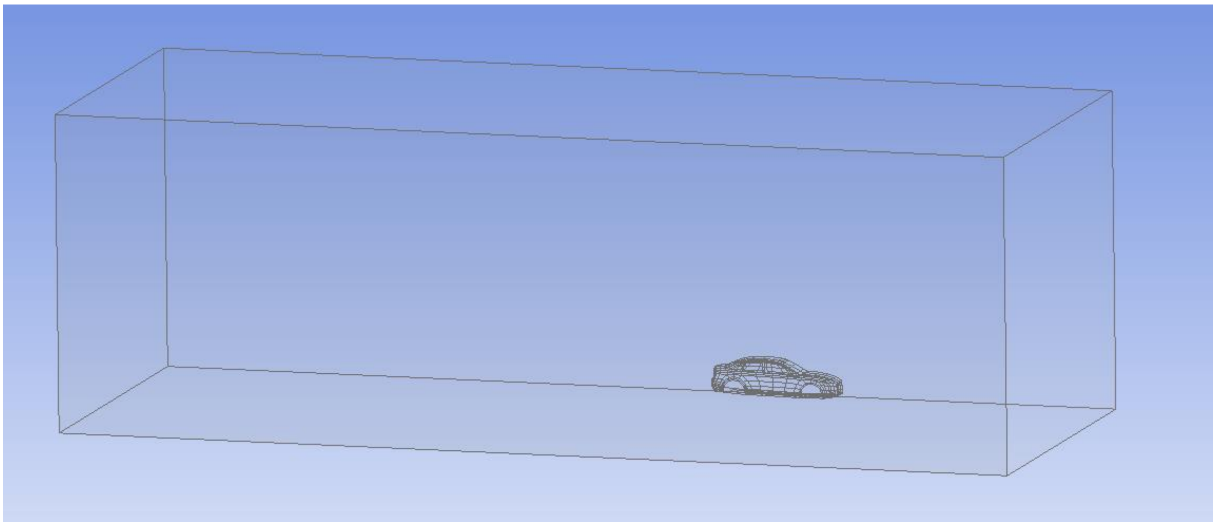

Figure 3-11 Car numerical simulation domain.

For the grid refinement, we used the same strategy that we employed for the Ahmed body simulation (Section 3.6). This strategy is based on internal boxes created around the vehicle and in the wake region to explicitly control mesh size (Figure 3-12)

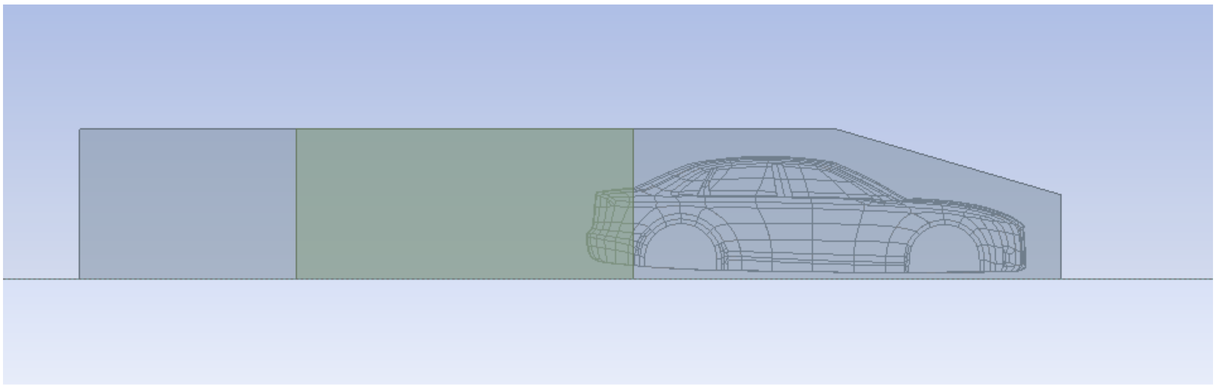

Figure 3-12 Refinement boxes for local grid refining (Car model).

The grid presents hexahedral elements close to the Car walls to capture the high normal gradients at the boundary layers, like we did for the Ahmed body (Section 3.6). The number of mesh elements are presented in section 4.5 during the GCI study. Some mesh features can be seen in Figure 3-13 and Figure 3-14.

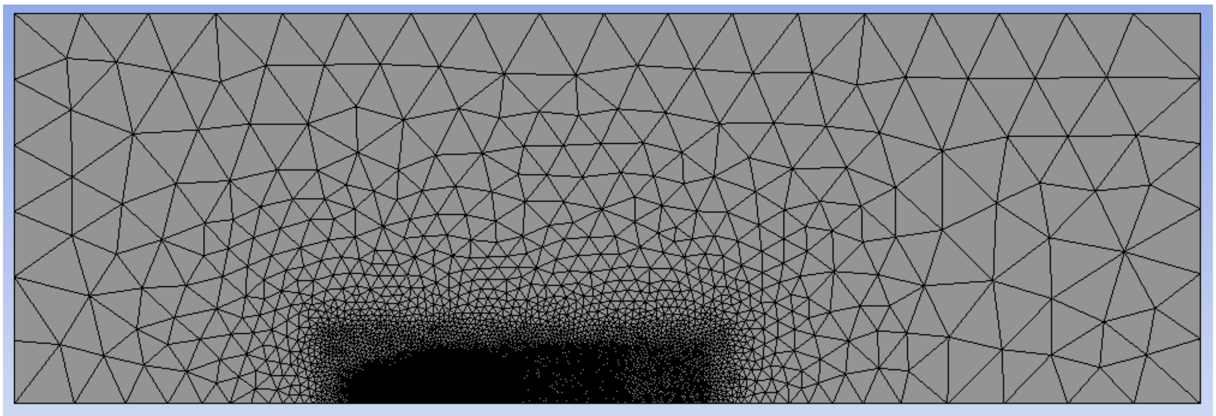

Figure 3-13 Car model mesh features.

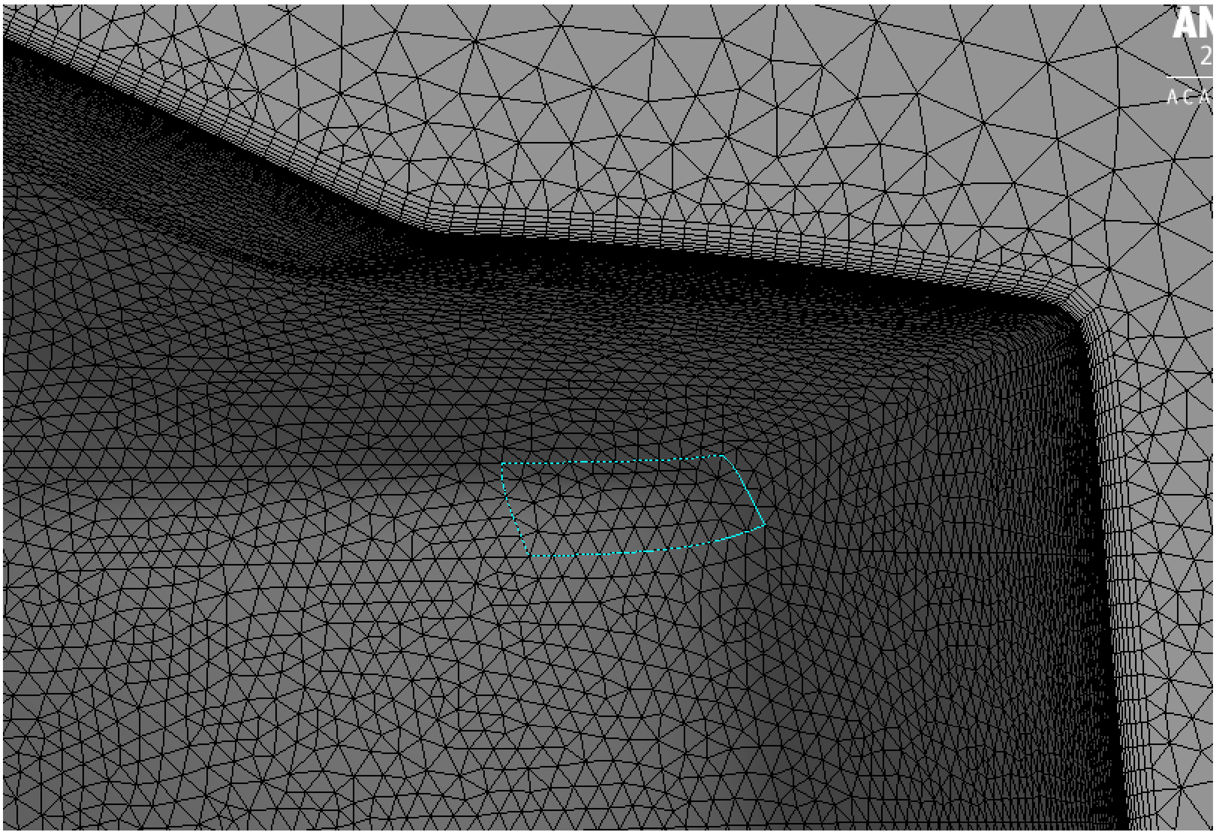

Figure 3-14 Car model mesh features (Boundary layer)

Details of the unstructured mesh are as follows:

- Relevance centre: coarse,
- Smoothing: high,
- Transition: slow,
- Initial size seed: Active assembly,
- Min. size: 10 mm,
- Max. Size: 1000 mm,

- Advanced size function: Proximity and Curvature.
- Inflation layer method of first aspect ratio of 5, growth rate of 20% of 5 layers was used.

With respect to the Fluent solution methods, turbulence model, discretization schemes and boundary condition all of them were the same as those used in Ahmed body simulation (Section 3.6).

3.7.2 Mesh convergence

To establish the accuracy of the CFD solution, and to keep the computational costs low, the Grid refinement was defined by a GCI study. This study had the same features used in the Ahmed body study (Section 3.6). More details about the calculation structure and results of Car model GCI study can be found in Section 4.5.

3.7.3 Geometry optimization

It was necessary to create a parametrized geometry to establish the optimization loop. The parametrized geometry was created in ANSYS DesignModeler. The parametrized dimensions are show in Figure 3-15, these dimensions are the height and length of the rear diffuser. For this case one vertical fin was added to avoid vortex generation, and tridimensional turbulent flow across the diffuser, keeping the streamlines in rear car direction increasing the rear diffuser efficiency (Figure 3-16).

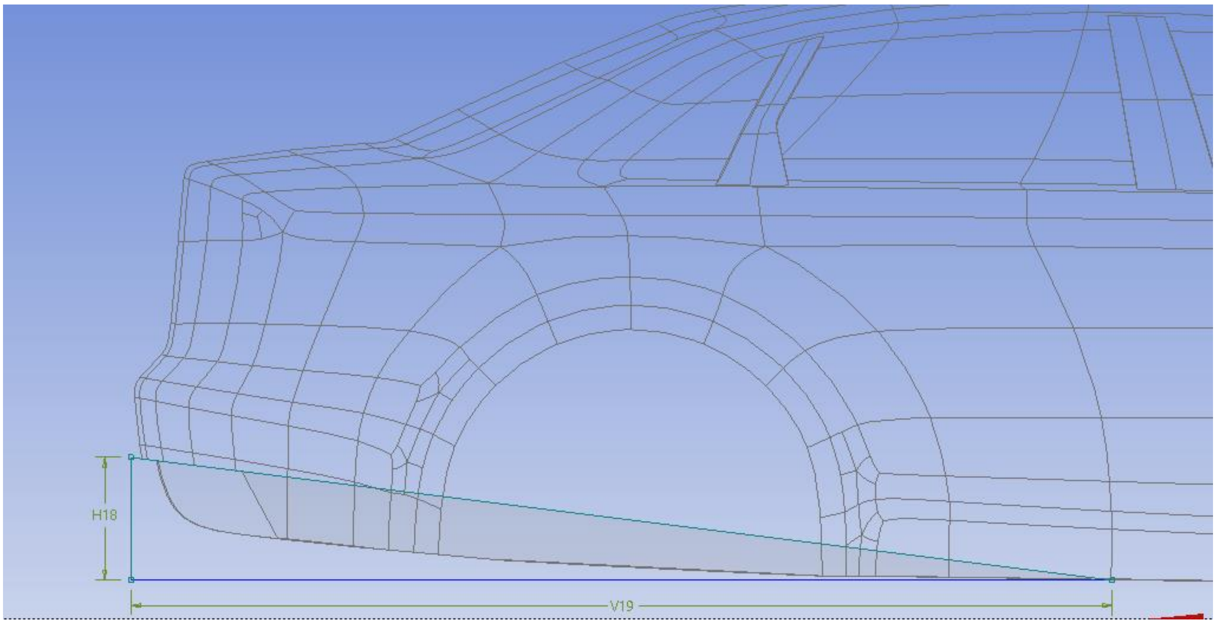

Figure 3-15 Car parametrized dimensions

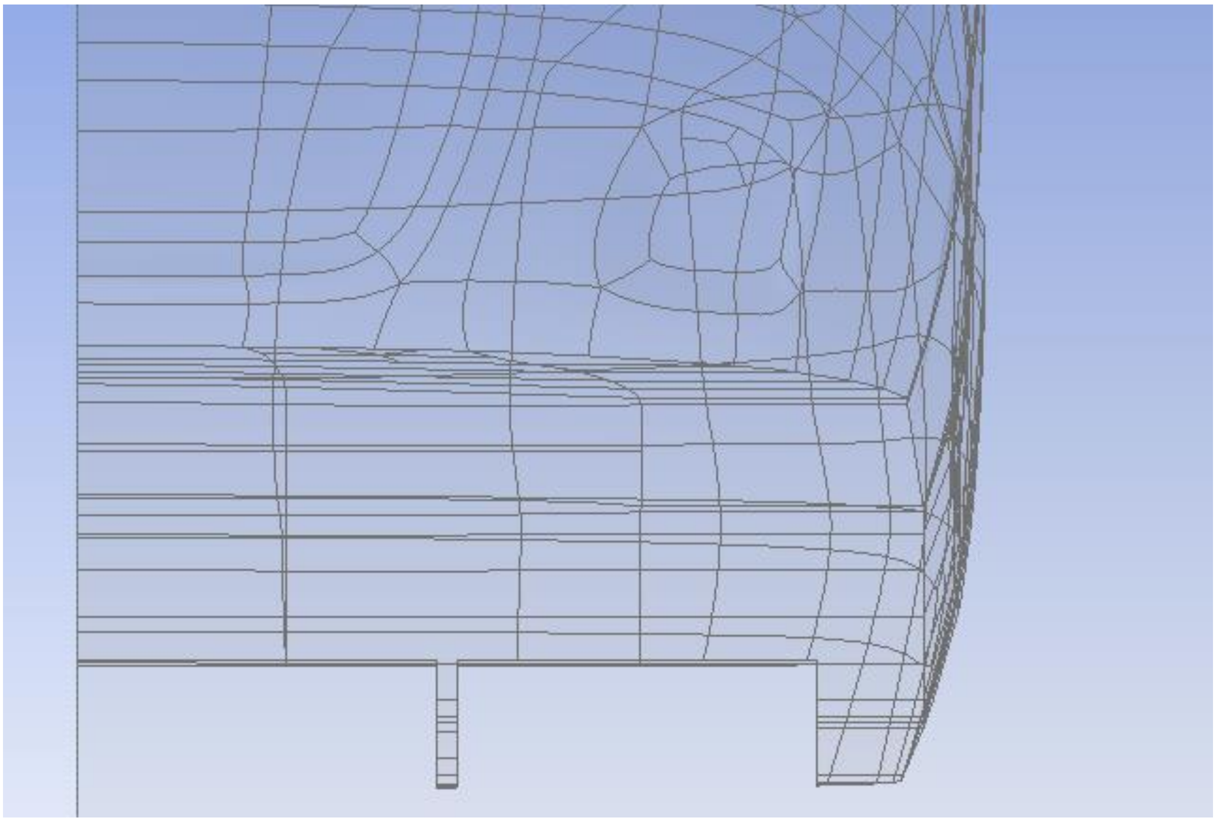

Figure 3-16 Vertical fin added to the rear diffuser surface

The structure of the optimization loop was exactly the same as that used in the Ahmed body optimization process (Section 3.6). Figure 3-9 shows a workflow of the optimization process.

4 Results

This section covers all the results from the simulations. An initial simulation was made to define the optimal mesh density to Ahmed body, for this a grid convergence index (GCI) study was applied (Nazar Baker et al., 2019). The setup and all conditions for this simulation were presented in section 3.6.

After defining the best mesh refinement, the results of this numerical simulation were used to compare against experimental results (Ahmed, 1984). The aim of this step was to validate the numerical model, so we could be confident about the turbulence model and other parameters of the simulation setup to be used posteriorly in the car geometry simulation.

We employed the Ahmed body due its simplicity to calibrate the optimization loop using modeFRONTIER. From this simulation, we defined the loop setup and the best optimization algorithms for this case.

After generating all results and validations obtained from Ahmed body simulation, we proceeded with the simulation of the flow around the Car model. Firstly, we carried out a GCI study to define an appropriate mesh in terms of accuracy and computational time. Based on the mesh obtained in the GCI study, we ran a CFD simulation with the standard configuration of the car geometry to be compared later with geometry optimization case. Finally, we employed an optimization loop to determine the best geometry for rear diffuser of the car. These results were then compared to the standard geometry case and the main differences are discussed from the flow point of view.

4.1 Ahmed body GCI study

The first goal of the numerical simulations was to perform a grid convergence analysis to define an adequate mesh considering accuracy and computation time. For this initial simulation the Ahmed body was used due its simplicity.

For this procedure, we carried out three different CFD studies using three successively finer grids. Table 4-1 shows the results of the three simulations, for C_D and C_L coefficients associated to each grid size. The third column show the grid size normalized to be used for the GCI study.

Table 4-1 Ahmed body GCI study results

Grid	N° Elements	Grid Spacing (normalized)	C_D results	C_L results
A	$20\text{x}10^5$	1	0.298	0.030
B	$10\text{x}10^5$	2	0.300	0.035
C	$5\text{x}10^5$	4	0.330	0.065

The results from Table 4-1 were used to make two different studies, one considering C_D results and another considering C_L results. The two results are compared, so we could assess the accuracy for both parameters.

4.1.1 GCI study from C_D results

Firstly, we determine the order of convergence:

$$P = 3.906$$

We now can apply Richardson extrapolation using the two finest grids to obtain an estimate of the value of the Cd at zero grid spacing:

$$Cd_{h=0} = 0.297$$

The grid convergence index for the fine grid solution can now be computed. A safety factor of **FS**=1.25 was used since three grids were used to estimate **p**. The **GCI** for grids 1 and 2 is:

$$GCI_{12} = 0.893$$

The **GCI** for grids 2 and 3 is:

$$GCI_{23} = 0.058$$

We can now check that the solutions were in the asymptotic range of convergence

$$\frac{GCI_{23}}{r^p * GCI_{12}} = 0.993$$

which is approximately one and indicates that the solutions are well within the asymptotic range of convergence. Based on this study we could say that the Cd (drag coefficient) for the Ahmed body case is estimated to be ***C***

The result for Richardson extrapolation using the two finest grids to obtain an estimate of the value of the Cl at zero grid spacing is:

$$Cl_{h=0} = 0.029$$

The grid convergence index for the fine grid solution, grids 1 and 2, is (Considering **FS**=1,25)

$$GCI_{12} = 21.42$$

The **GCI** for grids 2 and 3 is:

$$GCI_{23} = 4.166$$

The solution is in asymptotic range of convergence following by:

$$\frac{GCI_{23}}{r^{p} * GCI_{12}} = 0.857$$

Based on this study we could say that the Cl (lift coefficient) for the Ahmed body case is estimated to be **Cl = 0.029** with an error band of **4.166%**.

In these cases the GCI applied to lift coefficient had an error value greater than the GCI applied to drag coefficient.

In the view of the results obtained from the GCI study we considered grid 2 the best option.

4.2 Ahmed body CFD Validation

It is very important to validate numerical models against experimental data. We chose to compare our results to the experimental data obtained by (Ahmed, 1984) to validate the model, mesh and setup simulation. Even though slight differences were present in the model geometry (edge radii, overall dimensions, stilt positions etc.), the same ground clearance (50 mm) was used in the test setup, the total drag values obtained are almost same to those of Ahmed (1984) (Table 4-2).

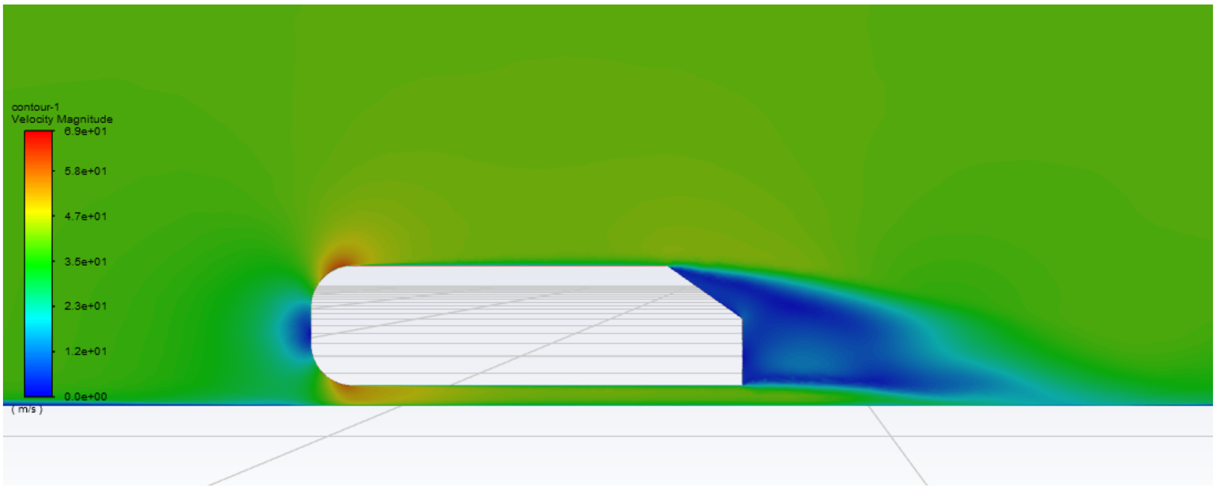

Figure 4-1 Velocity contour of Ahmed body

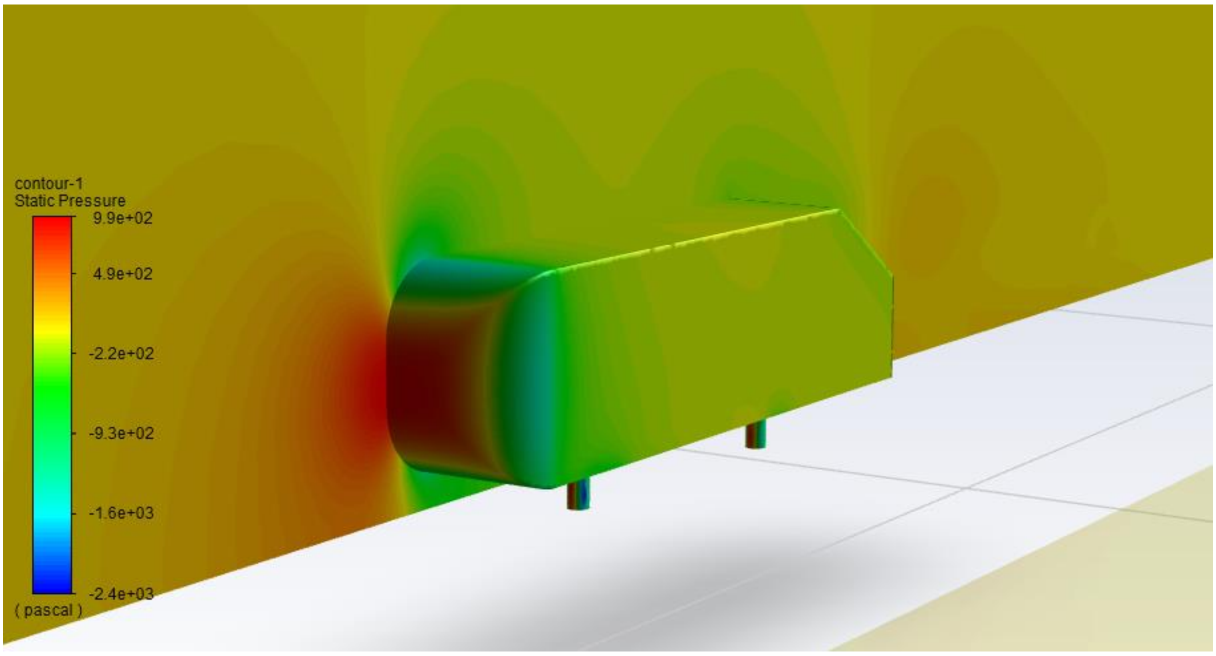

Figure 4-2 Pressure contour of Ahmed body (front view)

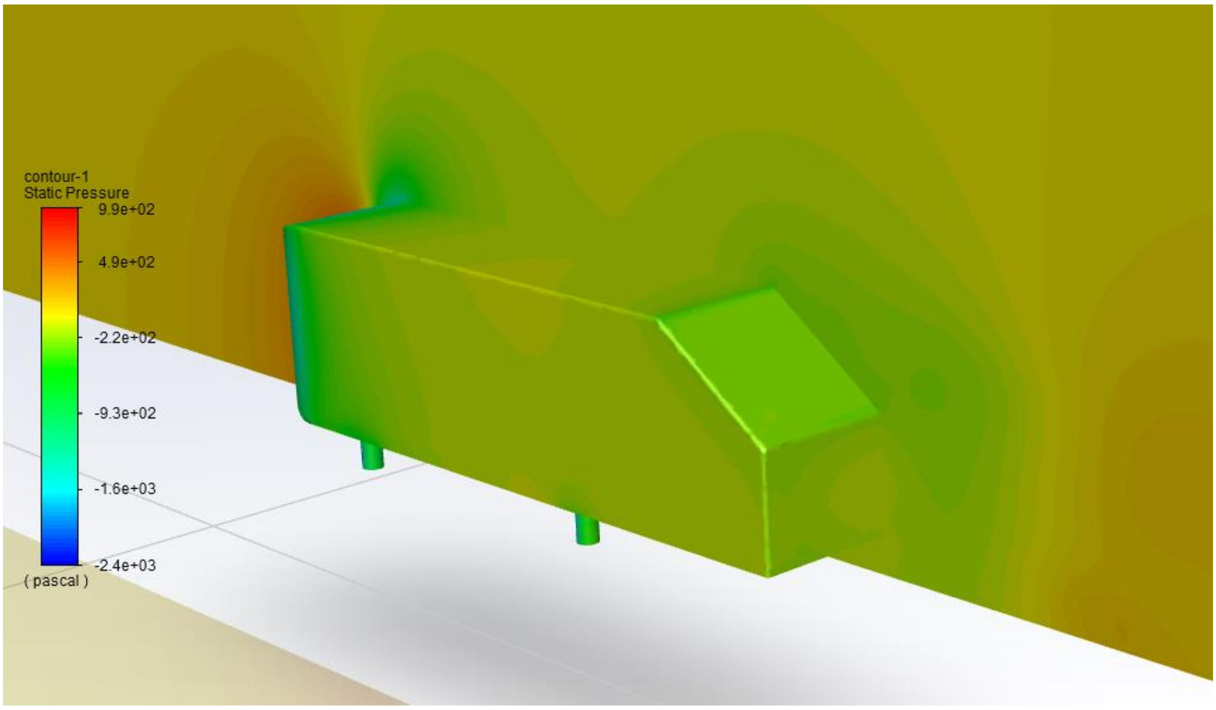

Figure 4-3	Pressure contour of Ahmed body (Rear view)

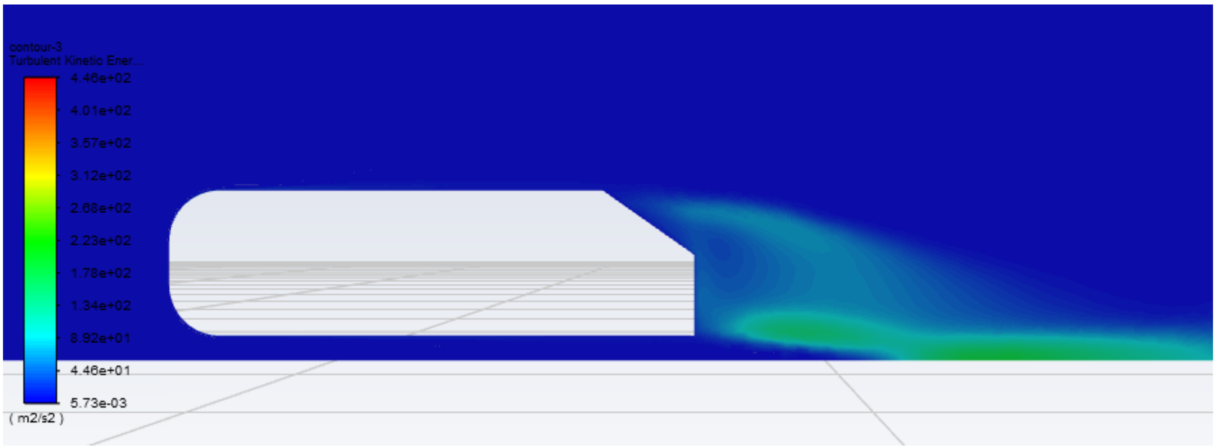

Figure 4-4 Turbulent Kinetic Energy contour of Ahmed body

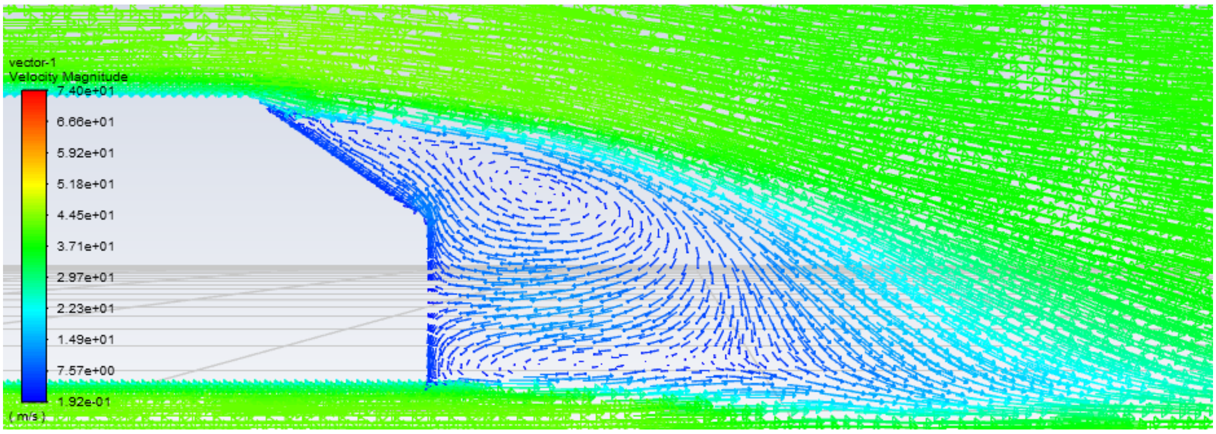

Figure 4-5 Velocity vector around Ahmed body

In Figures Figure 4-1, Figure 4-2Figure 4-3 , the static pressure contours help to understand the sudden deceleration of the flow. The red colour indicates that static pressure raises at the lower half of the nose section. At the top of the nose part the flow is accelerated and create a suction zone. The velocity then gradually decreases at the top surface of the body. The contour of turbulent kinetic energy (Figure 4-4) shows that a vortex pattern is created behind the Ahmed body, showing that the flow separation occurs in this regime. Back flow happens and, as a result, vortices are created. The velocity contours clearly show the velocity reduction behind the body due the flow separation, it generates a recirculation zone (Figure 4-5). The size and intensity of the recirculation zone gives an idea about the strength of form drag or pressure drag. The results of mean drag coefficient are shown in Table 4-2.

Table 4-2 Comparison of drag coefficients between CFD and experimental case.

	C_D
CFD	0.268
Experimental data	0.260

Comparing the drag coefficient (No ground effect) with Ahmed (1984) experimental data we found 3.1% of difference considering Low Drag case (Slant angle = 30º), and 29.1% of difference considering the High Drag Case (Slant angle = 30º). "The low drag flow for Slant angle = 30° was realised by fixing a splitter plate vertically on the ground board in the plane of symmetry behind the model. Between the upstream edge of the splitter plate and the model base, a gap of about 25 rom was left free" (Ahmed, 1984). As CFD simulation was made considering half model leading in count the symmetry it resembles more the low drag case.

4.3 Ahmed body geometry optimization

We employed modeFRONTIER and Ansys Workbench to build a geometry optimization loop as showed before in section 3.5.3. The aim of this simulation was to test different combinations of height and length of the rear diffuser in the way to get the minimum values of C_D and C_L. Based on this loop we got some generations of results for each algorithm, so we could assess the efficiency of each one.

The interval of height was 0.01 – 0.14 m and length 0.05 – 0.35 m. We started the simulation with 3 DOE (Design of experiments). Each algorithm was applied under the same initial DOE, and we set a total of 13 generations, and each generation had 3 individuals.

Totalizing 39 simulations per algorithm. Four algorithms were used: FAST, MOGT, NSGA and MOGA, all of them starting with the same DOE. The goal was to evaluate which one converged before and created a Pareto frontier to minimize both parameters.

4.3.1 FAST

This algorithm was used combined with NSGA-II algorithm and was the fastest to achieve convergence and create a well-defined pareto frontier. In Figure 4-6 it is possible to notice the Pareto frontier for C_D and C_L results.

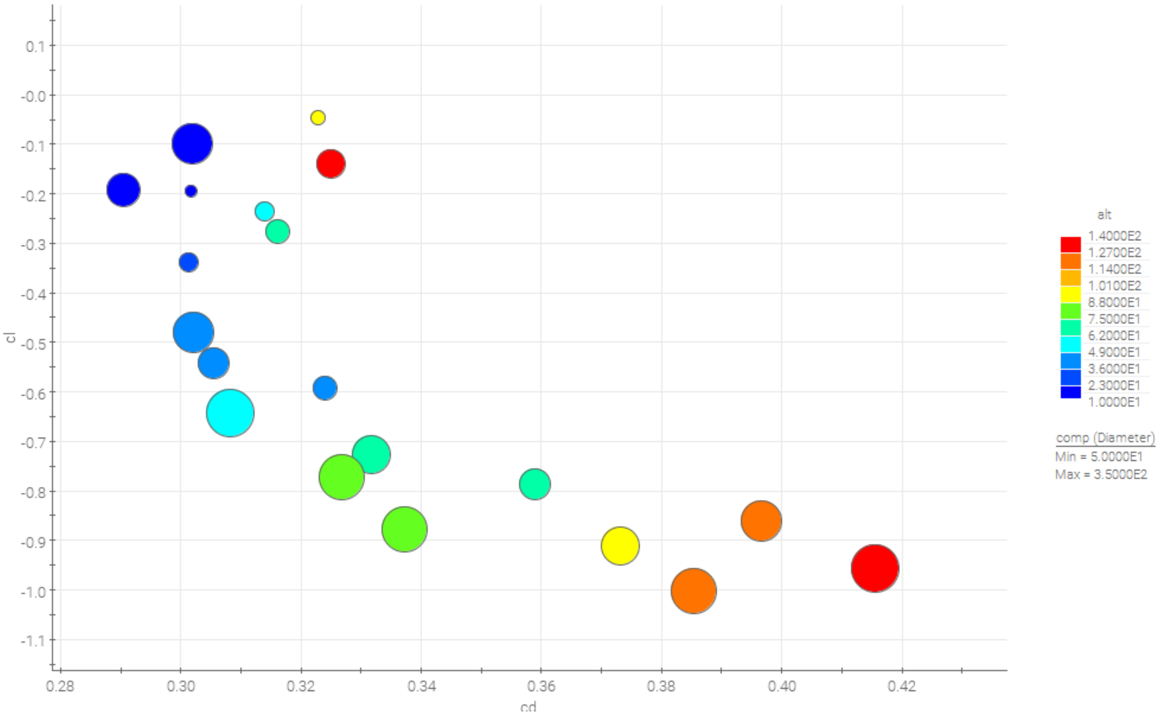

Figure 4-6 Shows the results of FAST optimizer algorithm applied to rear diffuser dimensions of Ahmed body. This is a 4D bubble chart, vertical axis represents lift coefficient, horizontal axis represents drag coefficient, the bubble diameter refers to diffuser length and bubble color refers to diffuser height.

4.3.2 MOGT

The MOGT algorithm did not perform well. This is a multi-objective optimization case, the aim was minimizing both parameters (C_D and C_L) at same time. However, the algorithm optimized just one parameter: only C_D was minimized considering the same generations and individual (Figure 4-7). Perhaps if we tried more generations and individuals it could form a Pareto frontier, but the time spent would be larger than the other algorithms, so not being very efficient like the other algorithms for this case.

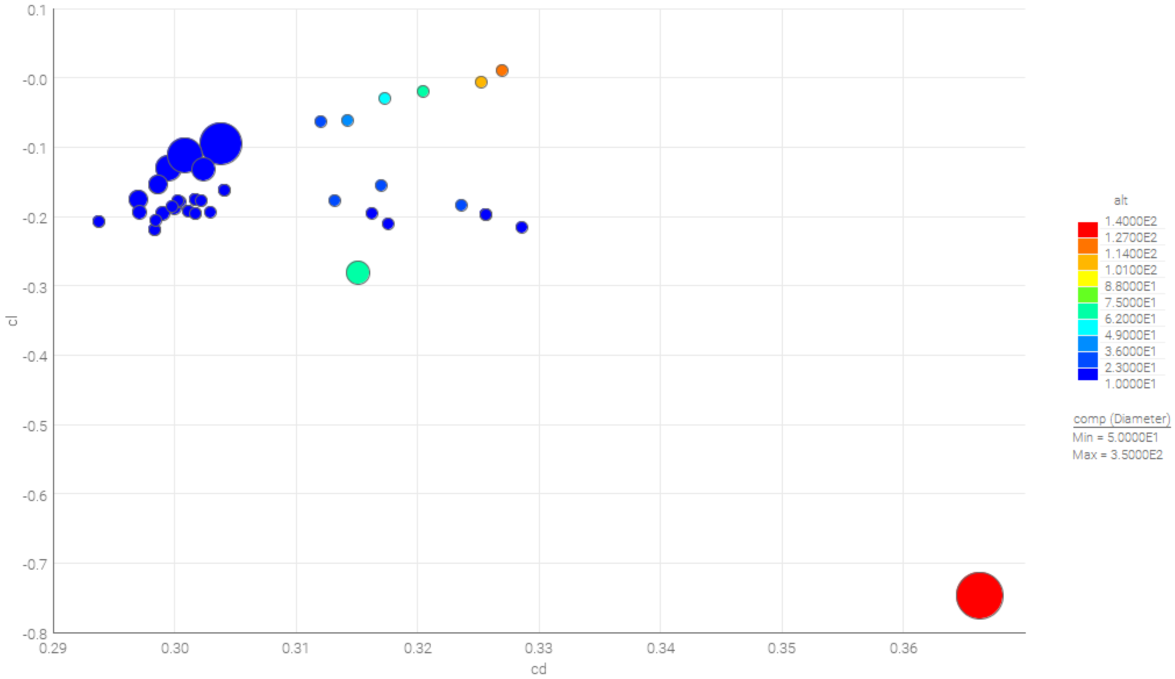

Figure 4-7 Shows the results of MOGT optimizer algorithm applied to rear diffuser dimensions of Ahmed body. This is a 4D bubble chart, vertical axis represents lift coefficient, horizontal axis represents drag coefficient, the bubble diameter refers to diffuser length and bubble color refers to diffuser height

4.3.3 NSGA-II

This algorithm performed very well creating a well-defined pareto frontier, but the time spent to do that was higher than FAST. This one needed 3 generations more to create a well-defined Pareto frontier like FAST as we can see in Figure 4-8.

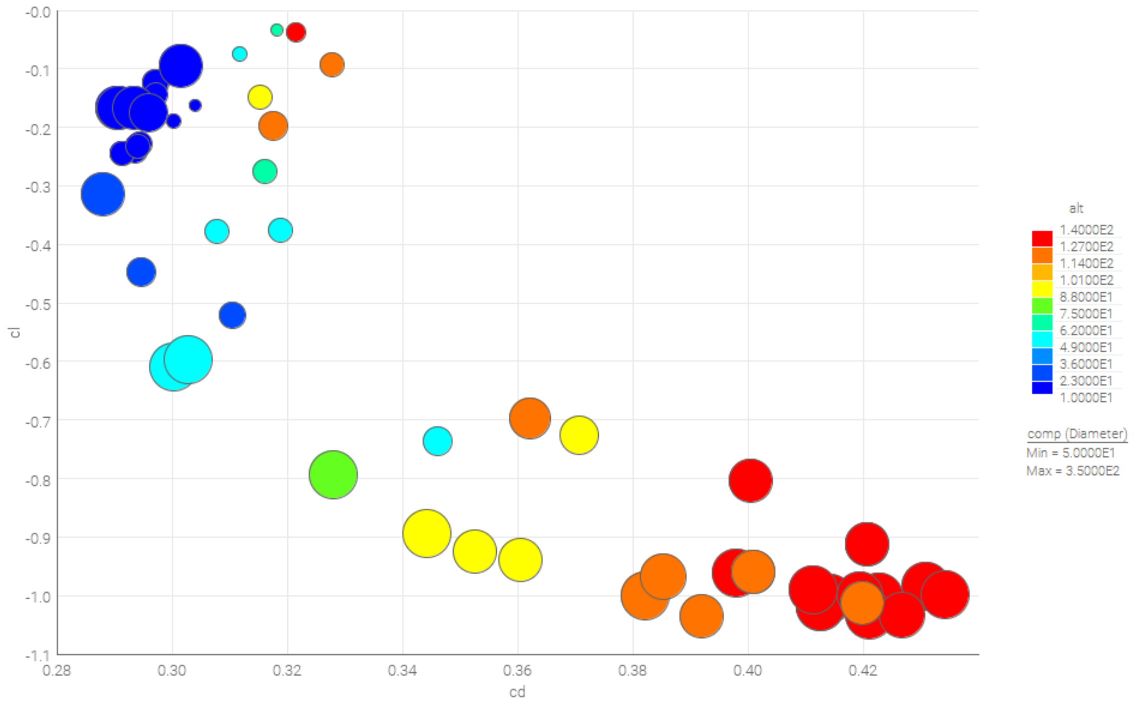

Figure 4-8 Shows the results of NSGA-II optimizer algorithm applied to rear diffuser dimensions of Ahmed body. This is a 4D bubble chart, vertical axis represents lift coefficient, horizontal axis represents drag coefficient, the bubble diameter refers to diffuser length and bubble color refers to diffuser height.

4.3.4 MOGA-II

MOGA-II did not perform well, starting with the same number of generations and individuals it did not converge. In this case the algorithm looked very efficient to minimize just one parameter, but in the case of a multi-objective approach it did not exhibited good performance (Figure 4-9).

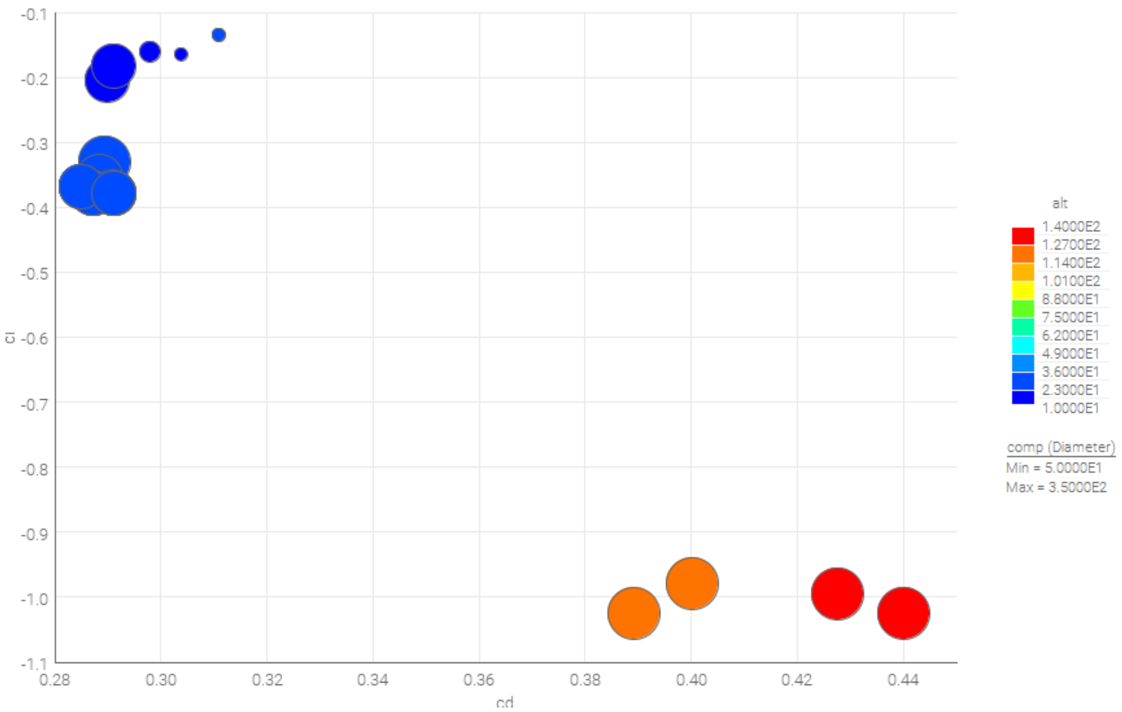

Figure 4-9 Shows the results of MOGA-II optimizer algorithm applied to rear diffuser dimensions of Ahmed body. This is a 4D bubble chart, vertical axis represents lift coefficient, horizontal axis represents drag coefficient, the bubble diameter refers to diffuser length and bubble color refers to diffuser height.

Looking for the data from the loop of optimization we can see that the more efficient algorithms were FAST-NSGA and NSGA-II, since they obtained a well-defined Pareto frontier. The only difference noted between the two cases was that FAST created the Pareto frontier quicker than NSGA-II. Because of that, the FAST-NSGA was chosen as the more efficient algorithm.

Through the results we can identify two interesting configurations: the “Low Drag” and “High Downforce”. The first is characterised by a drag that is as lower as possible (without increase in vertical load), the latter by a high value of the vertical load, with a low increase in drag.

The results for these configurations are summarised in Table 4-3.

Table 4-3 Results of the optimization considering "Low Drag" and "High Downforce" cases

	C_D	C_L
Low Drag	0.287	-0.312
High Downforce	0.336	-0.89

The difference between the standard geometry, “Low Drag” and “High Downforce” configurations are shown in Figure 4-10 and Figure 4-11.

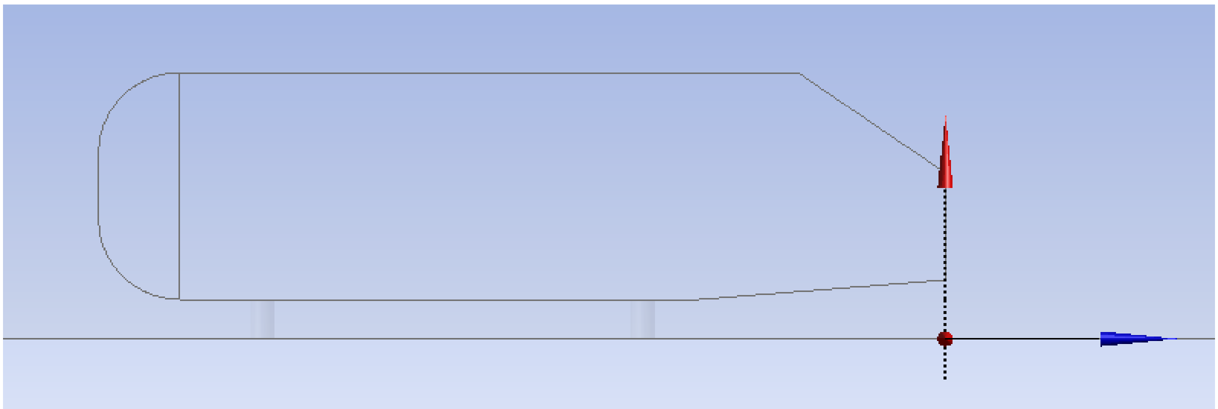

Figure 4-10 Rear diffuser dimensions for Ahmed body considering "Low Drag" configuration.

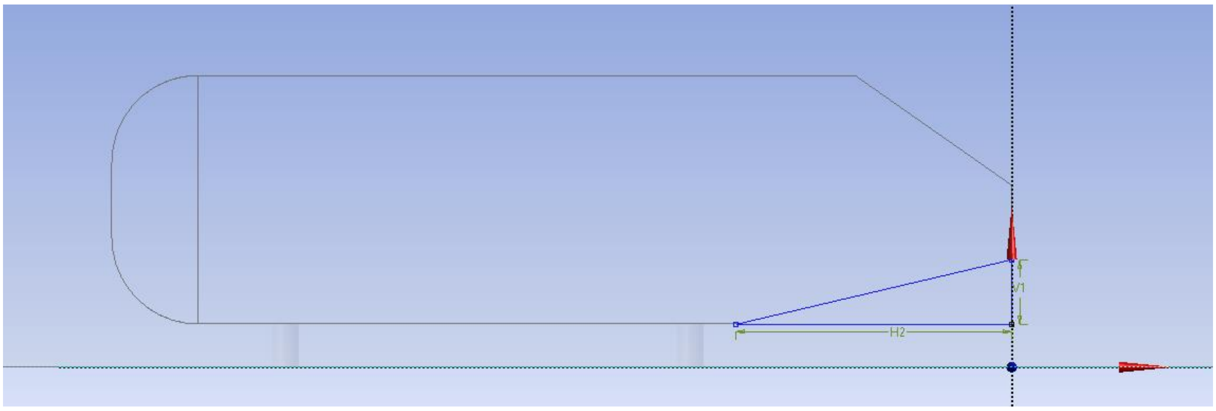

Figure 4-11 Rear diffuser dimensions for Ahmed body considering "High Downforce" configuration.

4.4 Comparison between Ahmed standard geometry and optimized geometry

In this section the flow characteristics between original and optimized case will be analysed with the aim to understanding what the geometry modifications influenced the flow characteristics to perform the improvement on downforce and drag.

The optimized case choose was a geometry with a good aerodynamic efficiency, that is, high values of downforce without the addition of excessive drag. Table 4-4 show the data of Ahmed body optimized case.

Table 4-4 Shows the data for rear diffuser optimized geometry chosen

Geometry Parameters (input)		Aerodynamic Parameters (output)		
Height	Length	C_D	C_L	Aerodynamic efficiency
0.075 m	0.32 m	0.336	-0.89	2.65

The Aerodynamic efficiency is calculated by:

$$Aerodynamic\ efficiency = \left|\frac{Lift\ Coefficient}{Drag\ Coefficient}\right| \tag{4.1}$$

Next, we present some figures to characterize the flow around the Ahmed body. Some charts are also presented, all figures and charts are always presented comparing the original geometry with optimized geometry. The flow features are discussed to understand what changes the rear diffuser can cause in the flow to improve its aerodynamic performance.

4.4.1 Contours of velocity magnitude

Looking to contour of velocity magnitude (Figure 4-12 and Figure 4-13) we can see that the behaviour at the front of the Ahmed body is the same for both cases. The frontal face is a stagnation point where velocity is close to zero, in the rounded corner the flow velocity increases. The noticeable difference is in the underneath, as the rear diffuser inlet considerably increases the flow velocity. That is result of a suction created by rear diffuser. Consequently, wake structure is completely different for optimized geometry due the flow change caused by the exit angle of the rear diffuser.

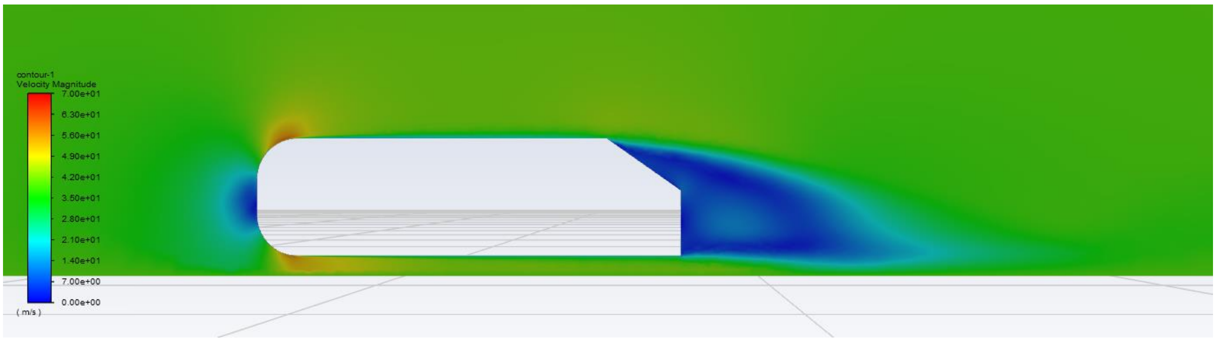

Figure 4-12 Ahmed body original geometry contours of velocity

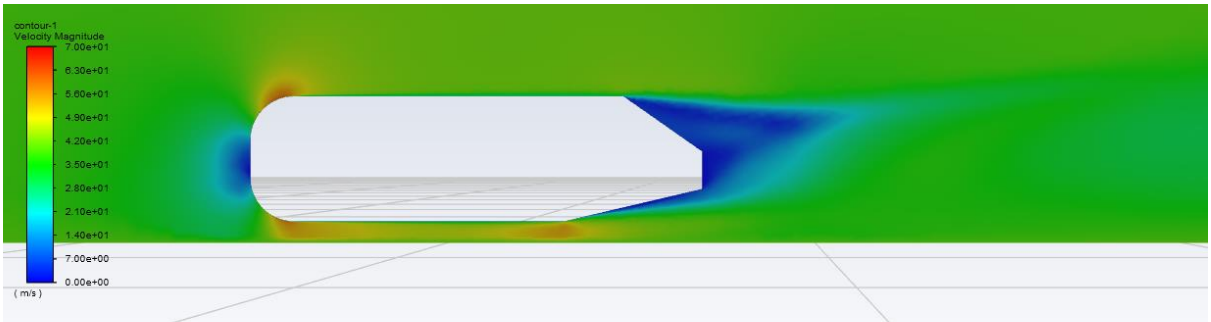

Figure 4-13 Ahmed body optimized geometry (rear diffuser) contours of velocity

4.4.2 Contours of static pressure

The main difference in pressure distribution can be noted through the Figure 4-14, and Figure 4-15. The difference is underneath: in the optimized case there is a low-pressure region, this region is responsible for the suction of the flow toward rear diffuser. Its clearer looking at Figure 4-16 and Figure 4-17, that the new green region represents the low-pressure region. There is also a slight difference in the slant angle pressure, this difference can contribute to reduce eddies in wake.

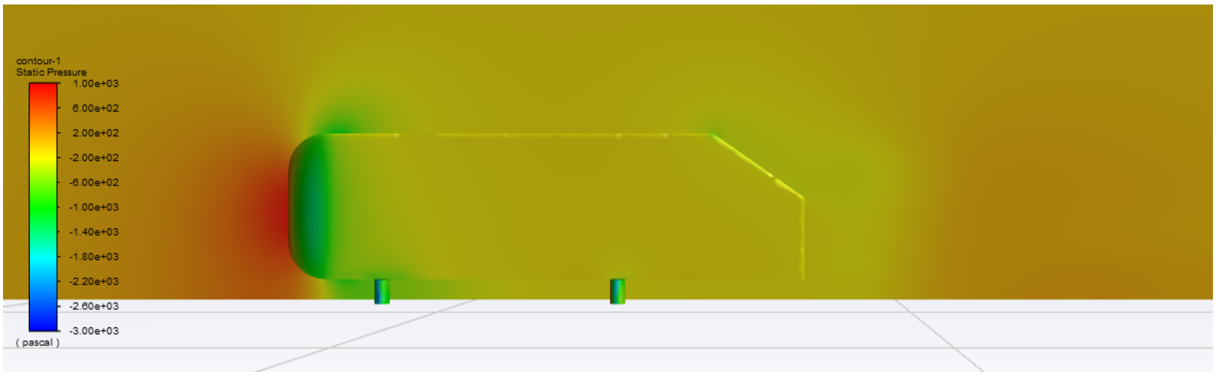

Figure 4-14 Ahmed body original geometry contours of static pressure.

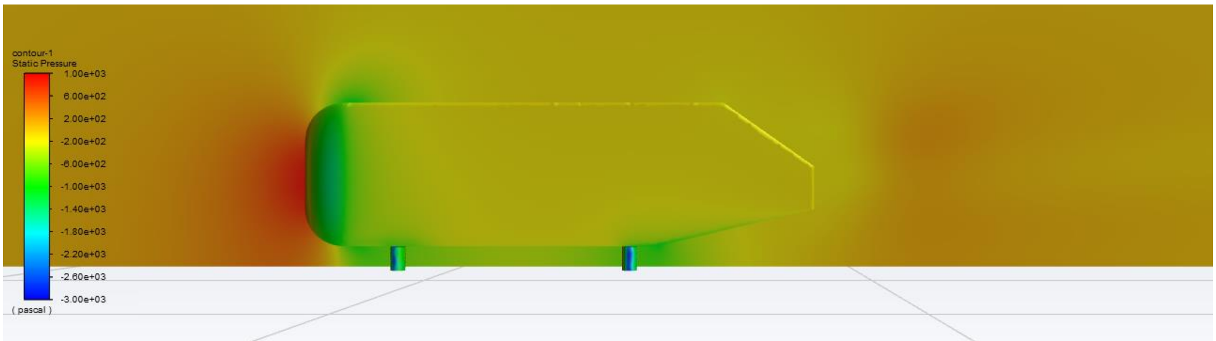

Figure 4-15 Ahmed body optimized geometry (rear diffuser) contours of static pressure.

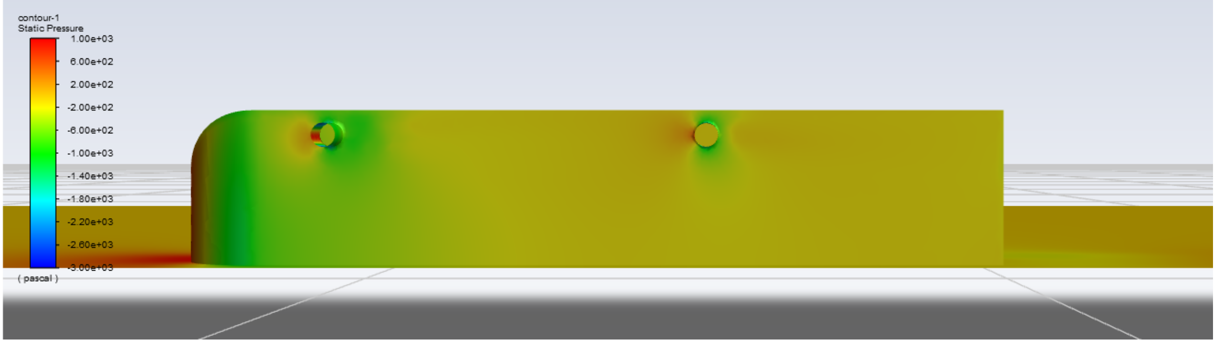

Figure 4-16 Ahmed body original geometry contours of static pressure (lower surface).

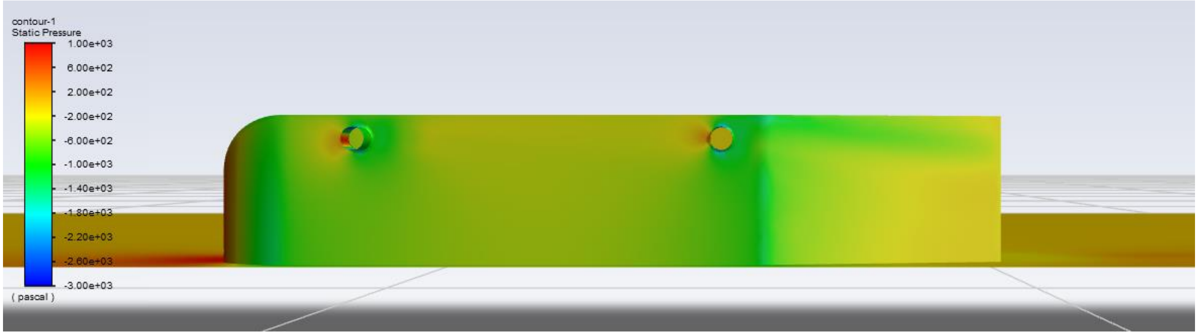

Figure 4-17 Ahmed body optimized geometry (rear diffuser) contours of static pressure (lower surface)

4.4.3 Contours of turbulent kinect energy

Figure 4-18 and Figure 4-19 show the distribution of turbulent kinetic energy for both cases, this parameter of the flow is associated with eddies. These eddies are formed in a low-pressure region and region where there is a strong separation zone. At the Ahmed body rear there is a low pressure caused by flow separation. In the optimize geometry the turbulent kinetic energy is smaller than original geometry, this is due to the change caused in the wake structure by the rear diffuser increasing the pressure at the exit flow of the diffuser.

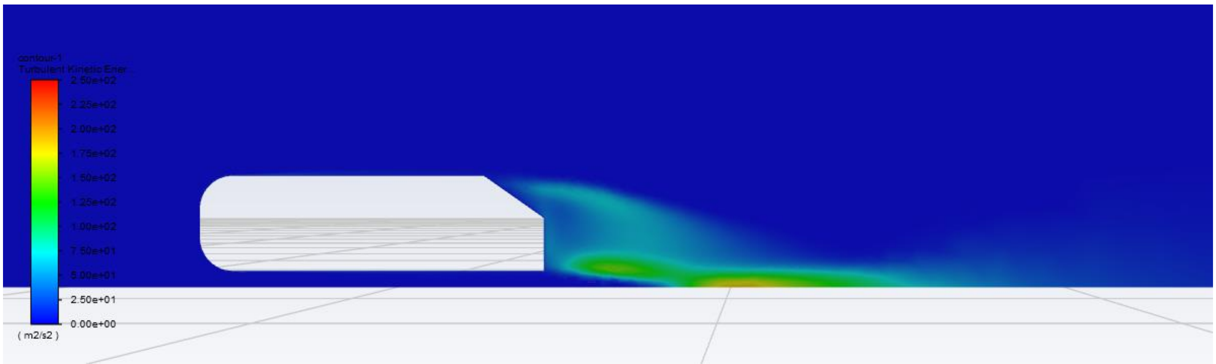

Figure 4-18 Ahmed body original geometry contours of turbulent kinetic energy

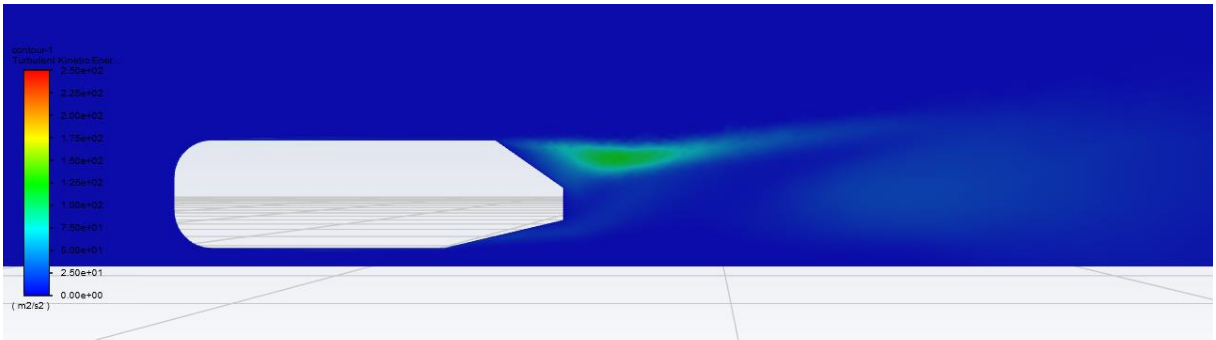

Figure 4-19 Ahmed body optimized geometry (rear diffuser) contours of turbulent kinetic energy

4.4.4 Contours of wall shear stress

Figure 4-20,Figure 4-21,Figure 4-22 andFigure 4-23, show the wall shear distribution over the Ahmed body surface. The dark blue zones can represent stagnation point (if associated a high-pressure zone) or separation zone. In both cases the blue region at front represents the stagnation point, at rear of the body and slant angle surface dark blue area means that is a separation zone for both cases. Looking at the rear diffuser (Figure 4-23), it is possible to see that the flow detaches from the surface at the end of diffuser close to symmetry plane. This can be explained by the high diffuser exit angle.

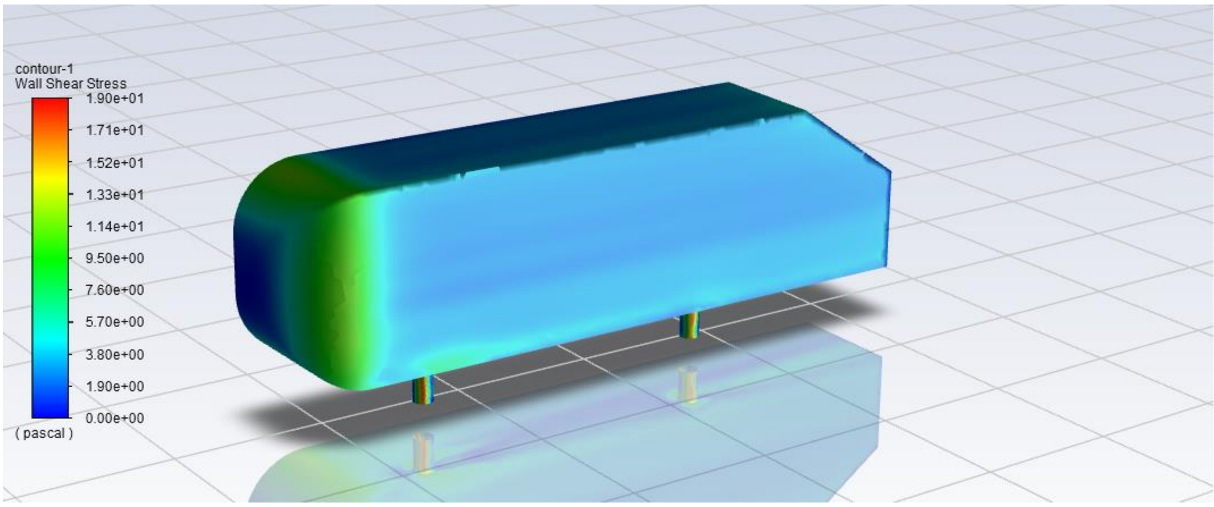

Figure 4-20 Ahmed body original geometry contours of wall sear stress

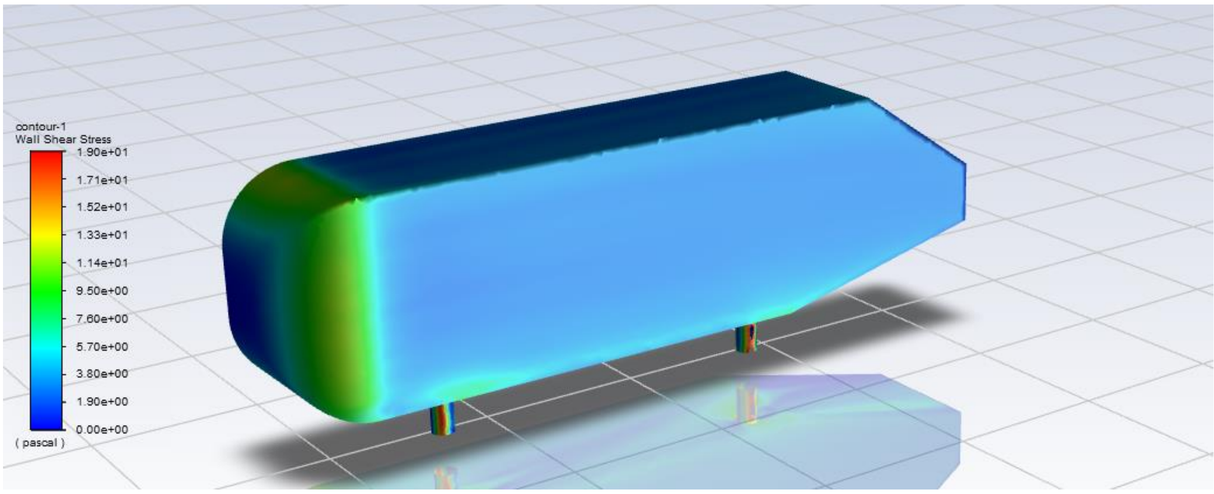

Figure 4-21 Ahmed body optimized geometry (rear diffuser) contours of wall sear stress

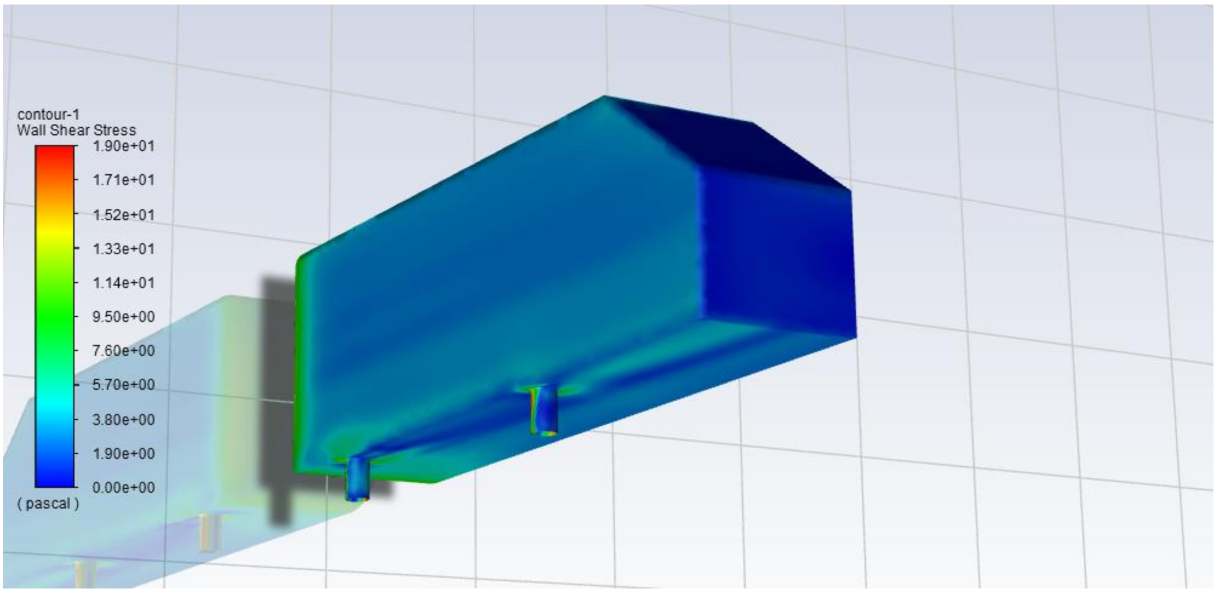

Figure 4-22 Ahmed body original geometry contours of wall sear stress

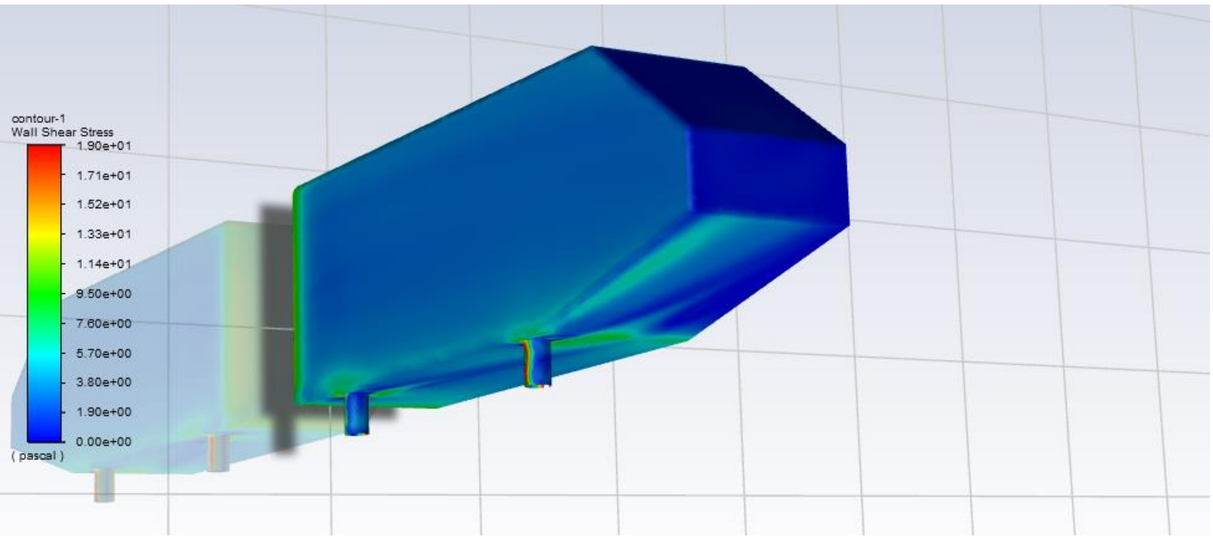

Figure 4-23 Ahmed body original geometry contours of wall sear stress

4.4.5 Velocity vectors

Analysing the velocity vectors of the flow makes it possible to see the wake structure behind the body. In the original geometry case there is a two-vortex formation in the recirculation zone, one on top of the other, leading to a small, thin wake coming from the base of the body. (Figure 4-24).

The wake structure for the optimized case is completely different being smaller than that of the original geometry (Figure 4-25). There is only one vortex near the slant angle. The second vortex is not formed due the rise of the pressure caused by the rear diffuser.

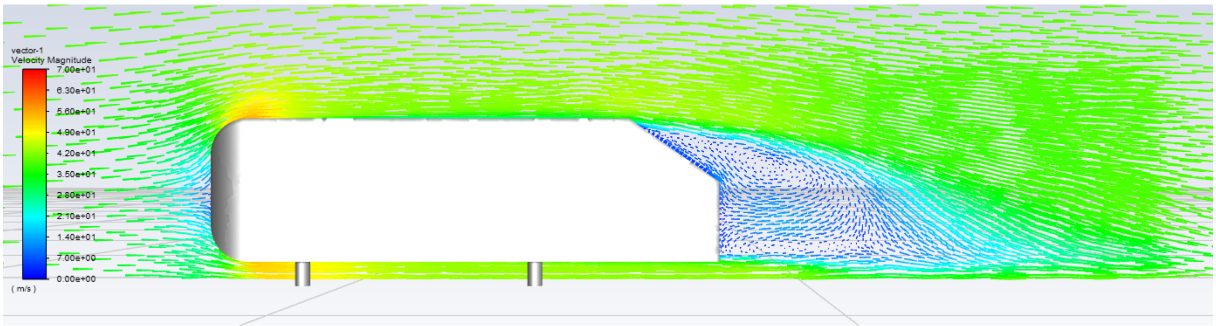

Figure 4-24 Ahmed body original geometry vectors of velocity

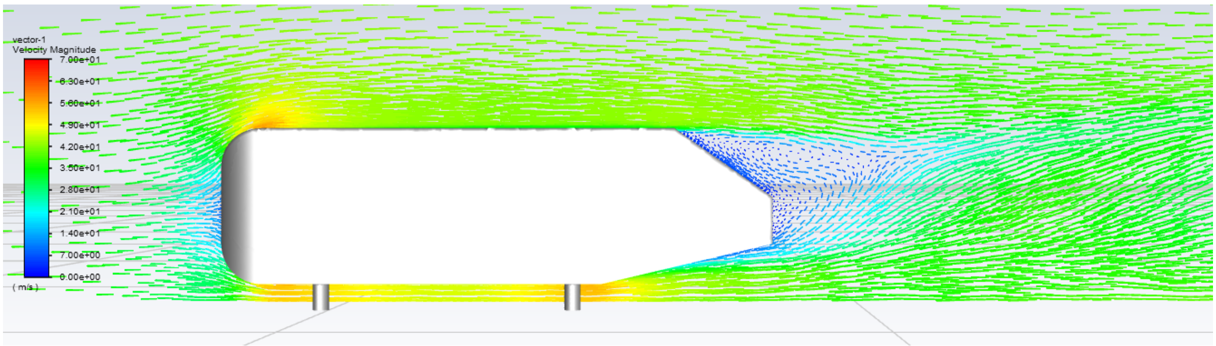

Figure 4-25 Ahmed body optimized geometry(rear diffuser) vectors of velocity

4.4.6 Pathlines

Pathlines are the trajectories that individual fluid particles follow. Figure 4-26, Figure 4-27, Figure 4-28 and Figure 4-29 show the pathlines of velocity at the bottom surface. We can see that the flow velocity increases in the rear diffuser region compared with the original geometry. It is also possible to see a vortex formation behind the “vertical foot”.

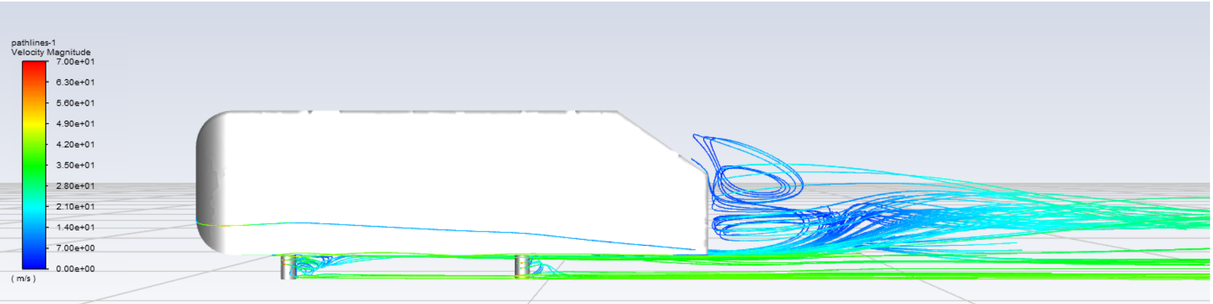

Figure 4-26 Ahmed body original geometry pathlines from lower surface

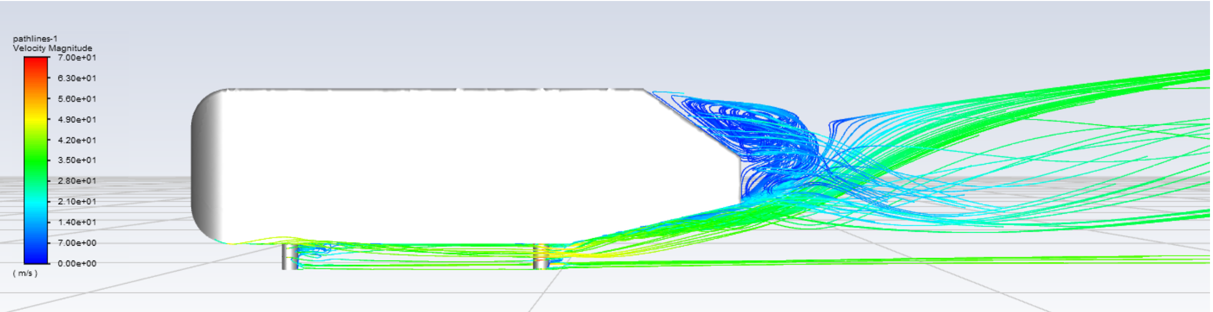

Figure 4-27 Ahmed body optimized geometry (rear diffuser) pathlines from lower surface

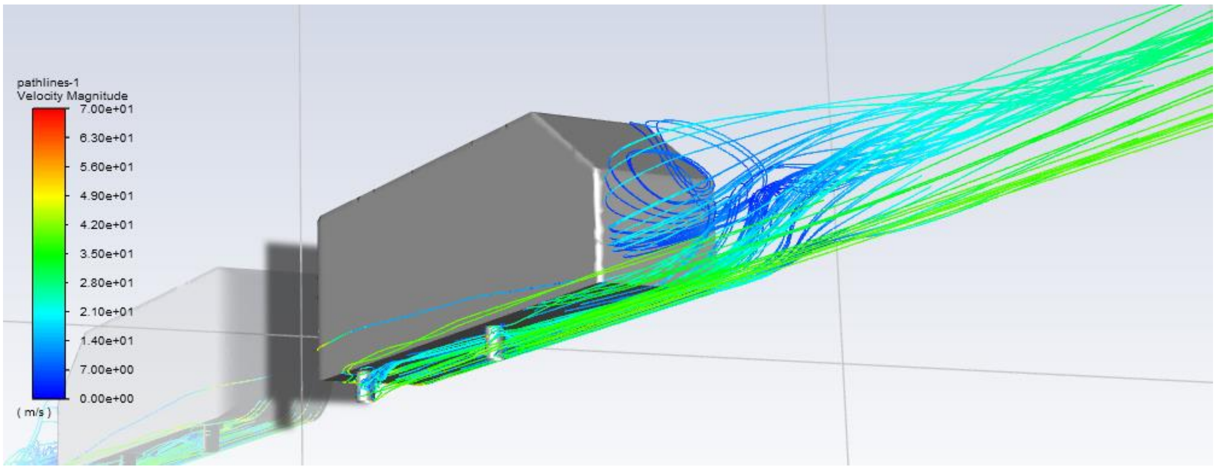

Figure 4-28 Ahmed body original geometry pathlines from lower surface

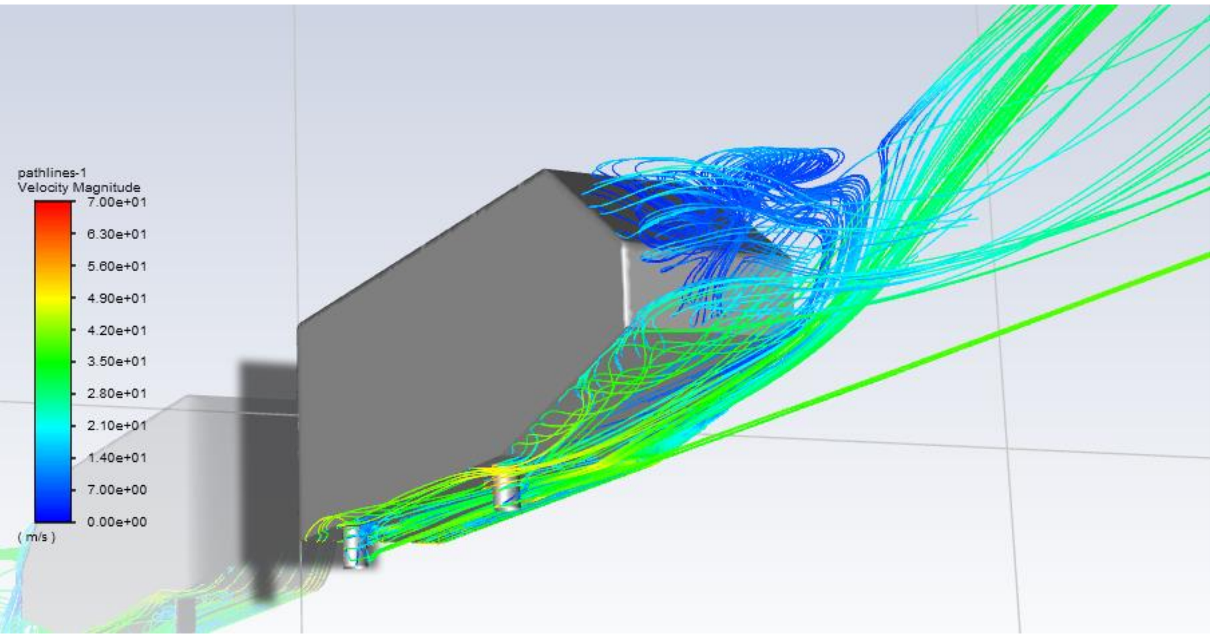

Figure 4-29 Ahmed body optimized geometry (rear diffuser) pathlines from lower surface

4.4.7 Vertical force distribution

The charts shown in Figure 4-30**,** Figure 4-31represents the distribution of vertical force along the upper surface for both cases. Basically, there is no difference between the two cases. At the front of the body the vertical force starts from zero due the completely vertical face, further up the force increases because the round corner, resulting in the largest values. Along the horizontal surface it assumes a value close to zero, at the beginning of the slant angle the vertical force increases slightly.

Looking at Figure 4-32 and Figure 4-33we can see an important difference in the vertical force at the bottom surface when we compare the original geometry with optimized geometry. That is due the rear diffuser that creates a suction underneath of the body. This point is easy to identify, because this is where we find the lowest values of vertical force. The suction caused by the inlet of the diffuser accelerates the flow increasing the negative vertical force along all the bottom surface.

As we have a mean positive vertical force at upper surface and negative vertical force at bottom surface, it results in more downforce in the optimized geometry.

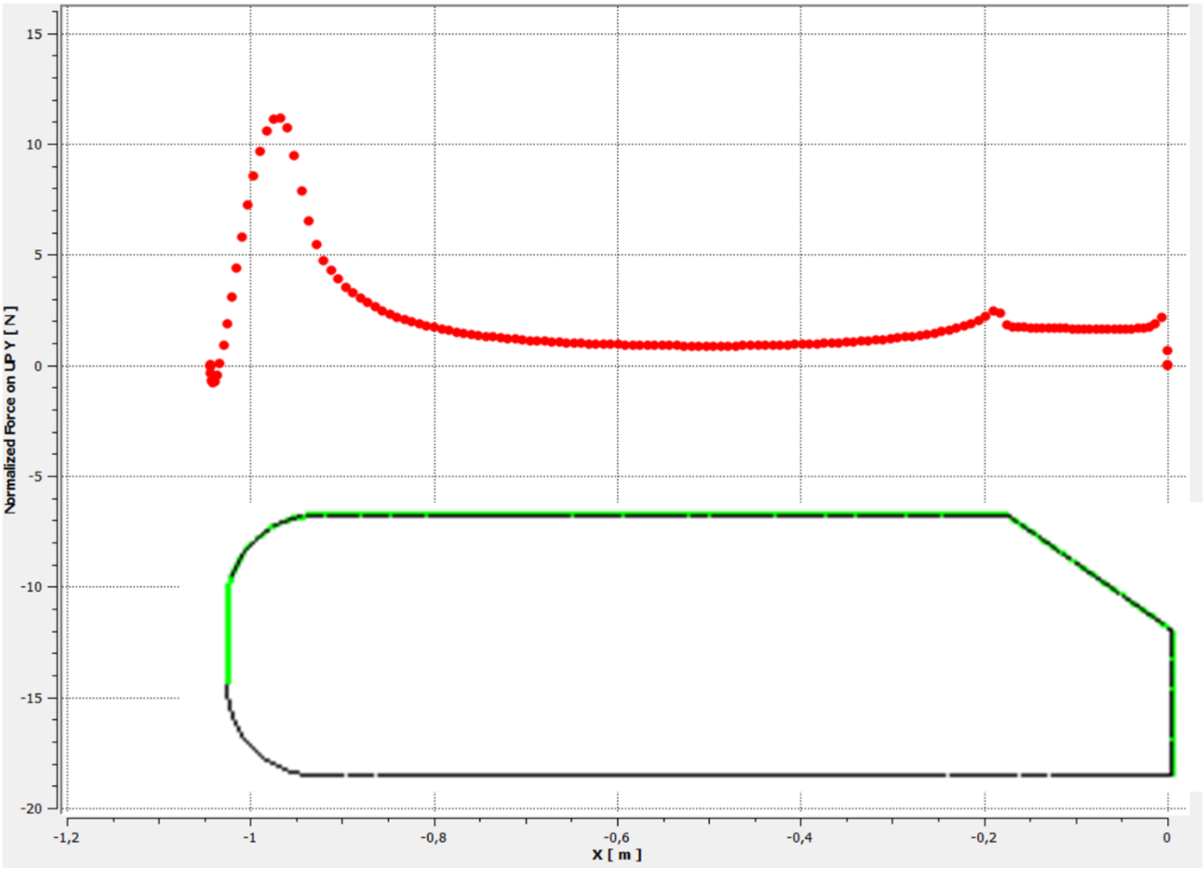

Figure 4-30 Vertical force distribution at the upper surface (original geometry).

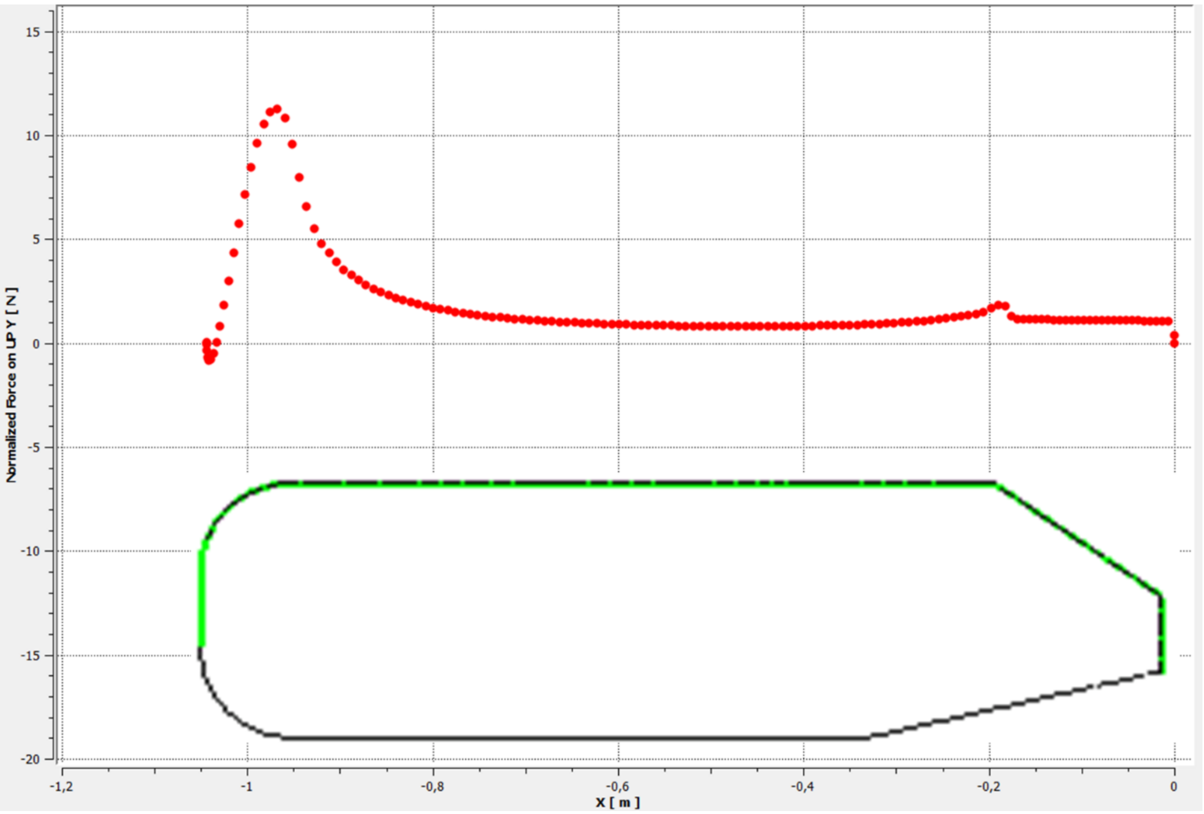

Figure 4-31Vertical force distribution at the upper surface (optimized geometry).

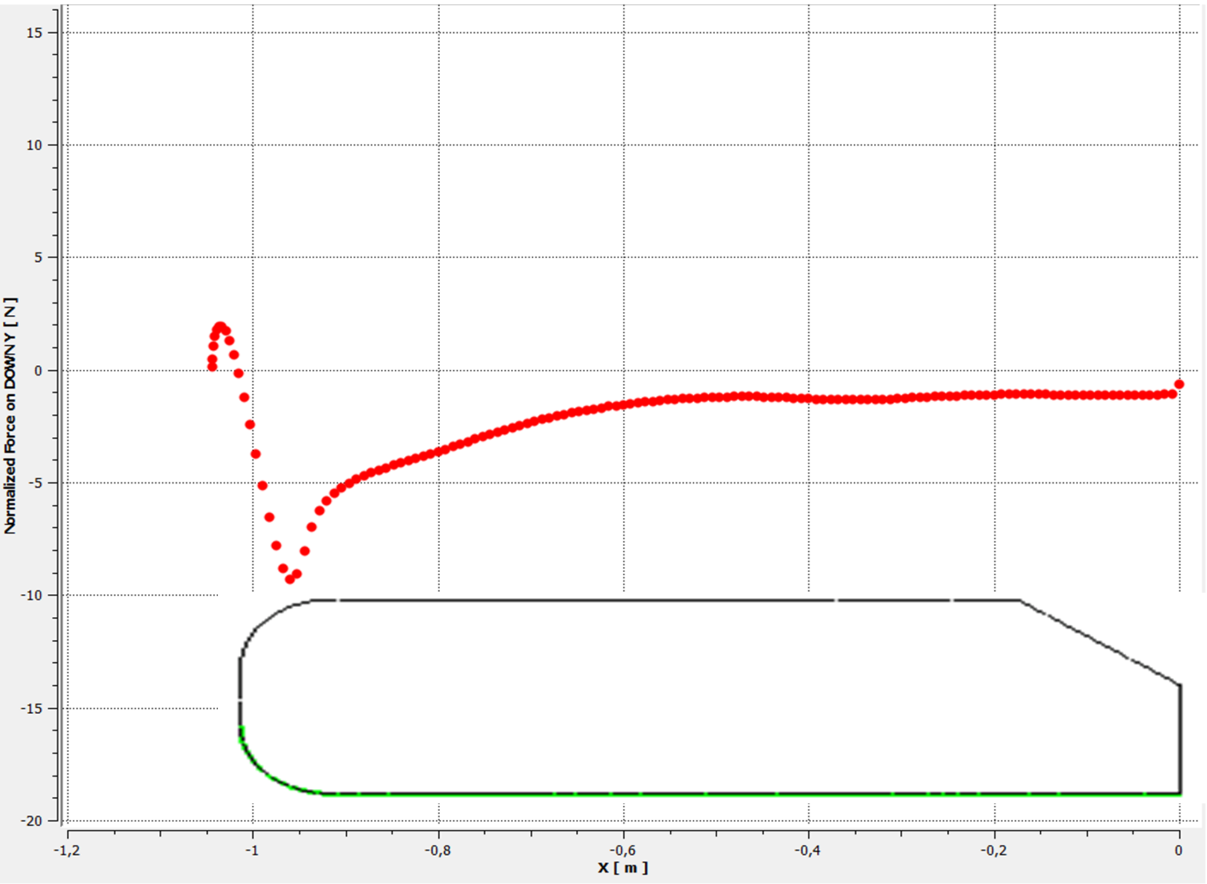

Figure 4-32Vertical force distribution at the bottom surface (original geometry).

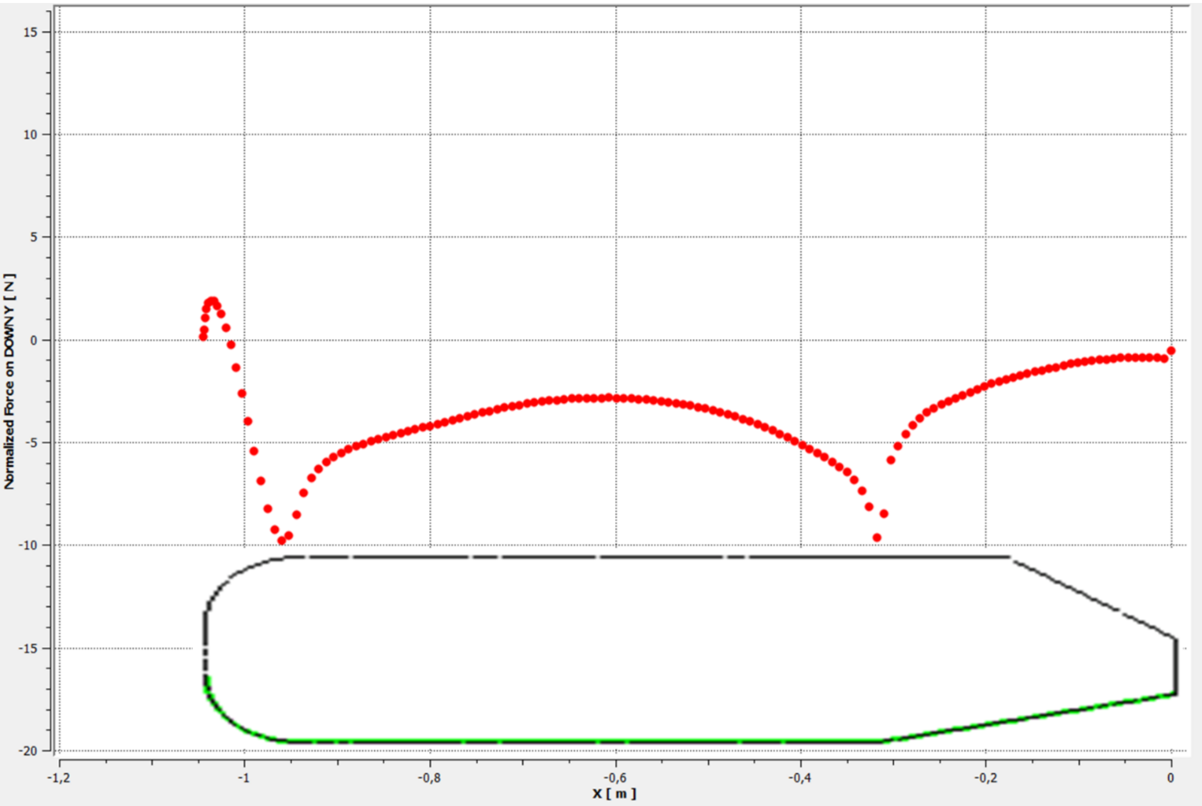

Figure 4-33Vertical force distribution at the bottom surface (optimized geometry).

4.4.8 Horizontal force distribution

By examining the horizontal force distribution, it is possible to identify regions that contribute to drag. Looking at Figure 4-34 and Figure 4-35 we cannot see differences between the two situations. In both cases the vertical surface at the front has the highest value of horizontal force, which contributes more to drag. Further up, the round corner is responsible for decreasing the force due to velocity increase at this region. In the horizontal surface the force constant and a little bigger than zero, this is due the low shear stress at the surface.

The behaviour of horizontal force at the bottom surface (Figure 4-36, Figure 4-37) for both cases is well close. For the optimized geometry there is an increase of the force at the inlet of the rear diffuser probably due the low pressure at this region.

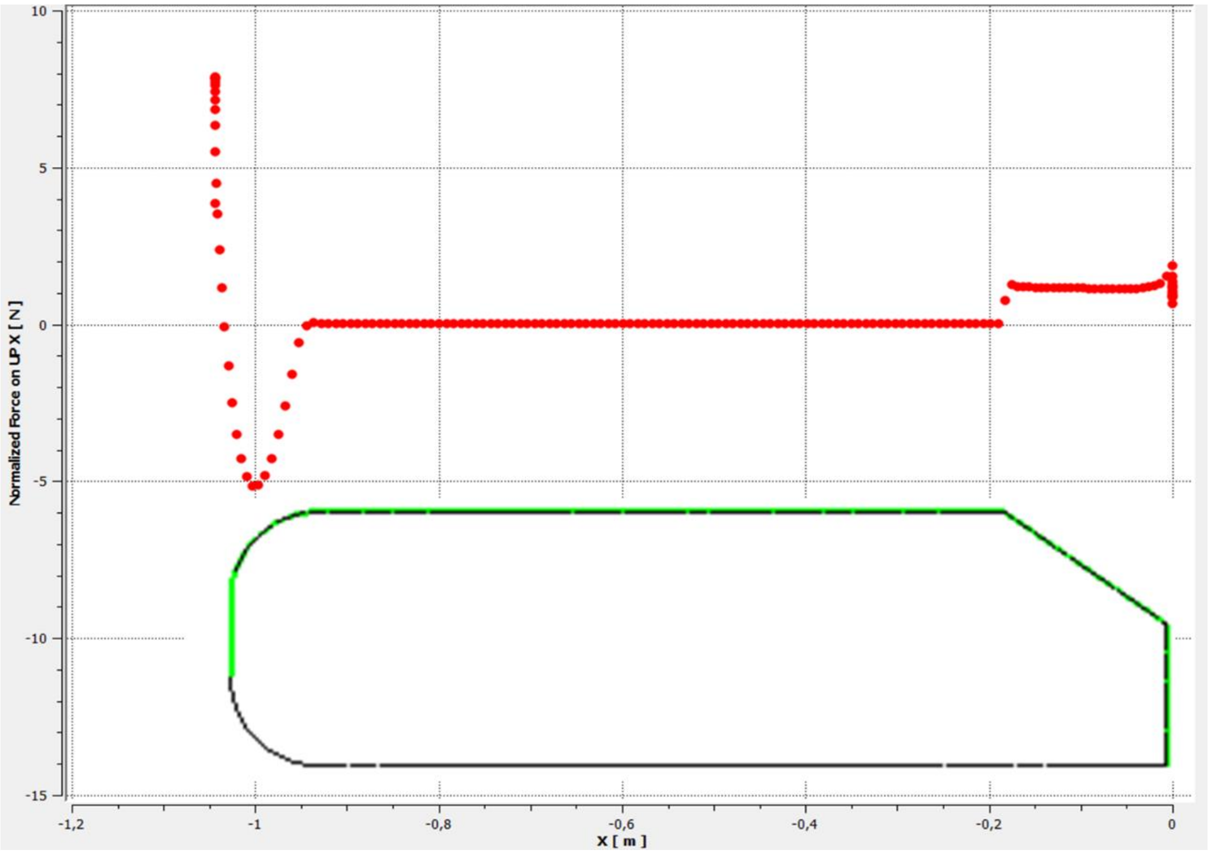

Figure 4-34 Horizontal force distribution at the upper surface (original geometry).

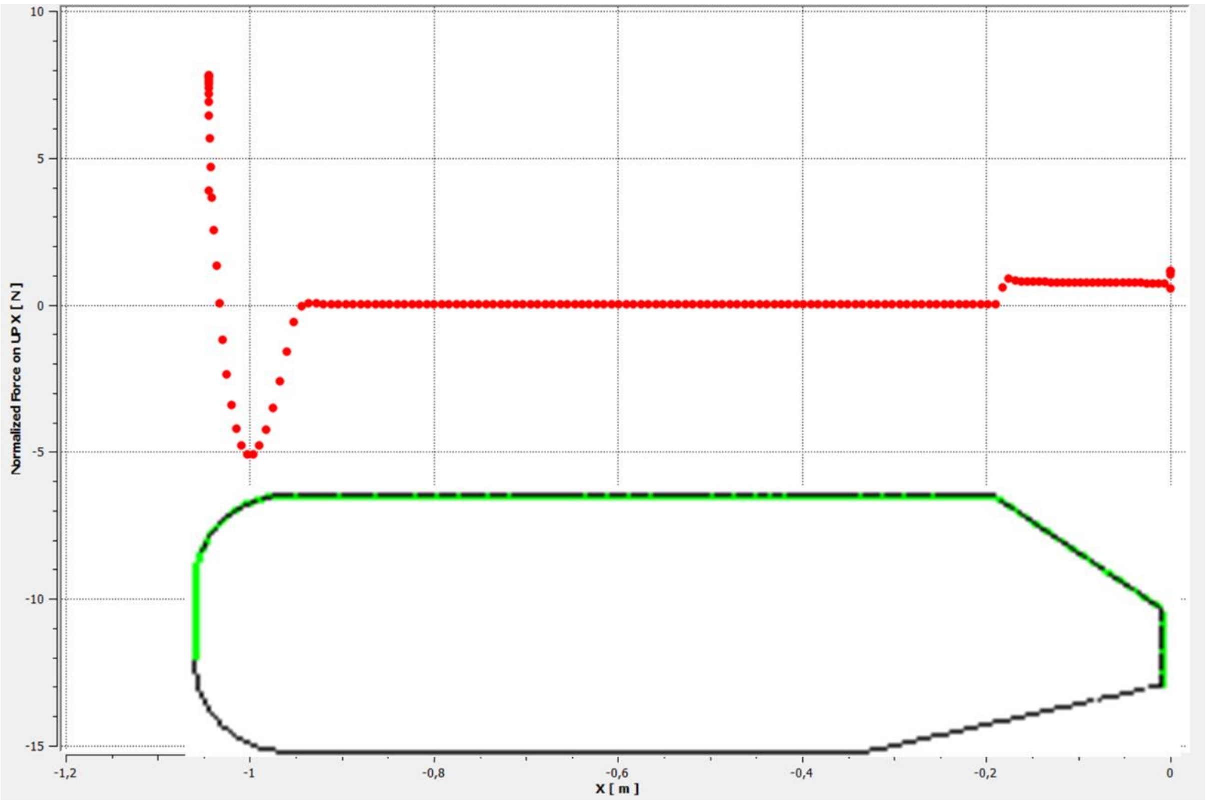

Figure 4-35 Horizontal force distribution at the upper surface (optimized geometry).

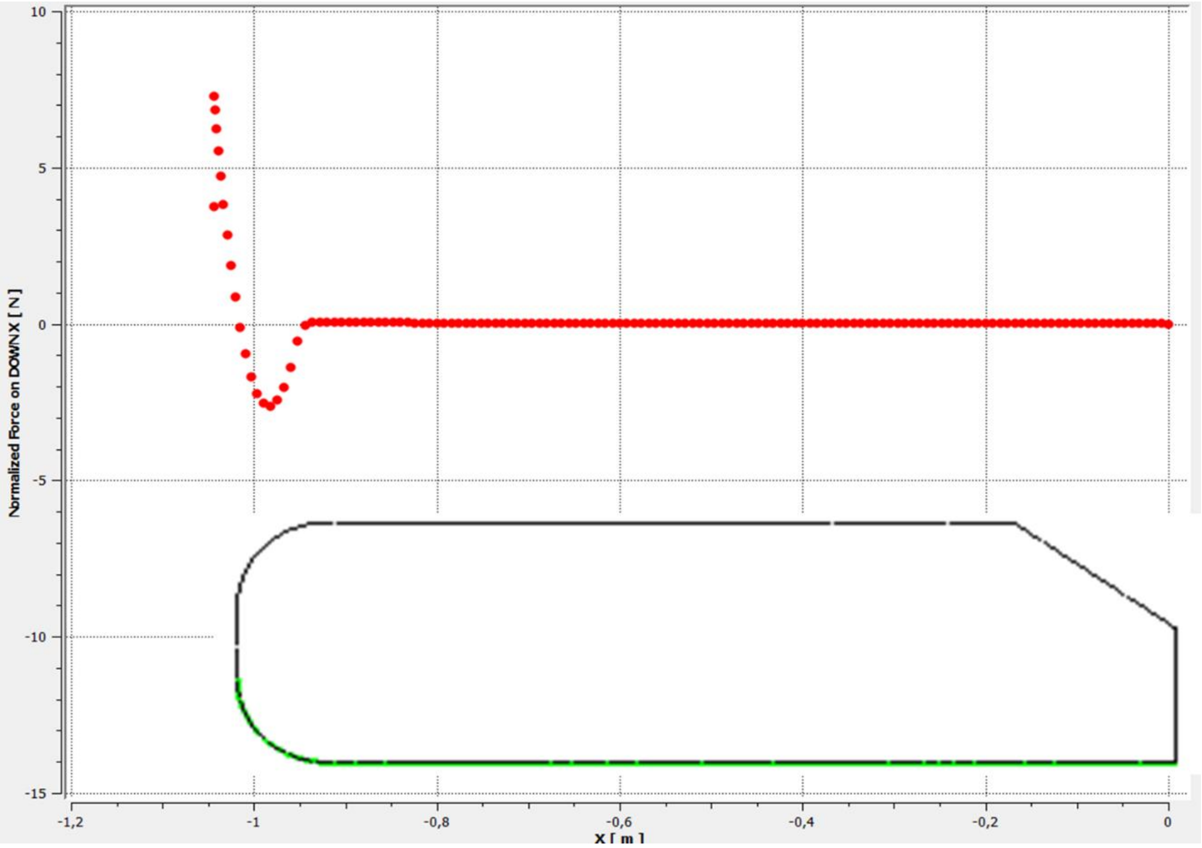

Figure 4-36 Horizontal force distribution at the bottom surface (original geometry).

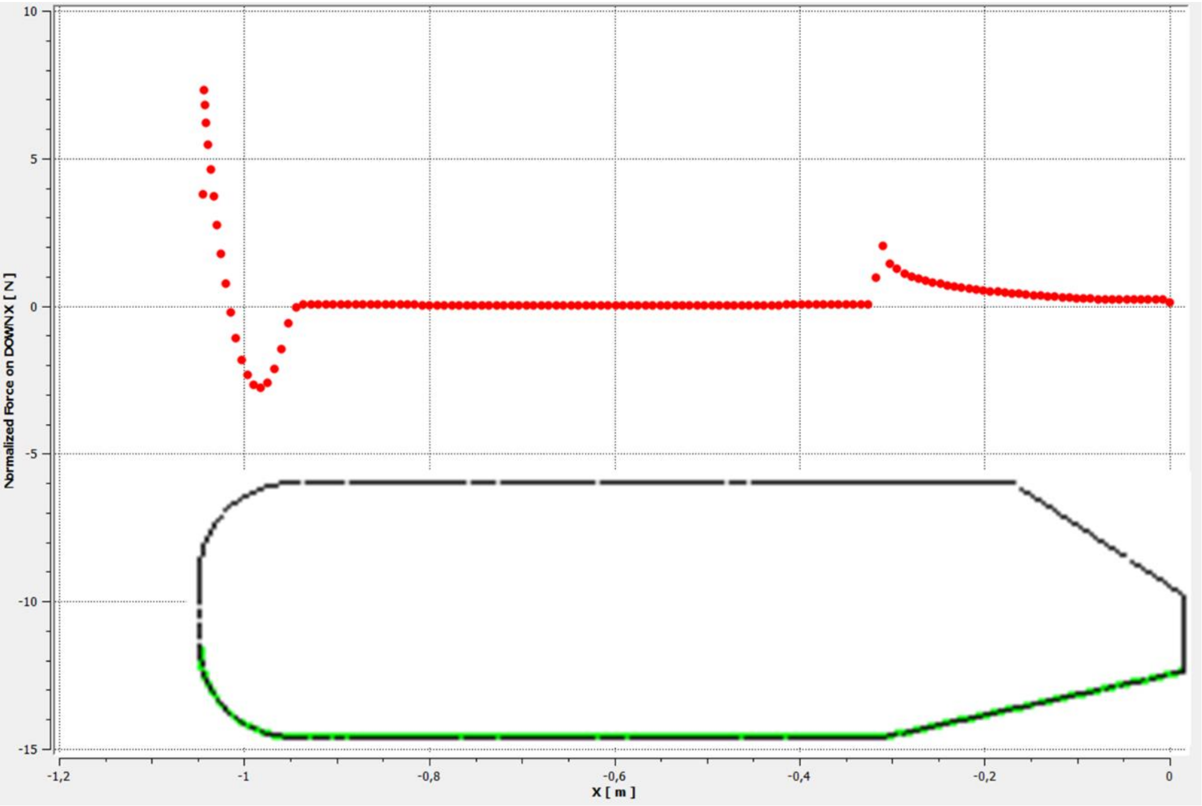

Figure 4-37 Horizontal force distribution at the bottom surface (optimized geometry).

4.4.9 Wall shear stress distribution

Looking to upper surface, both geometries have the same behaviour for wall shear distribution. The separation regions are characterized by zero wall shear stress. Through the chart present in Figure 4-38 and Figure 4-39, we can see that the wall shear assumes a value equals zero at the front face. This is due the stagnation point. At the rear slant angle the value is zero because of the flow separation.

At the bottom surface (Figure 4-40, Figure 4-41) there is an increase of the wall shear in the round corner region, because the flow accelerates at this point. The same happens at the inlet point of the rear diffuser. After this, the wall shear reduces gradually until zero.

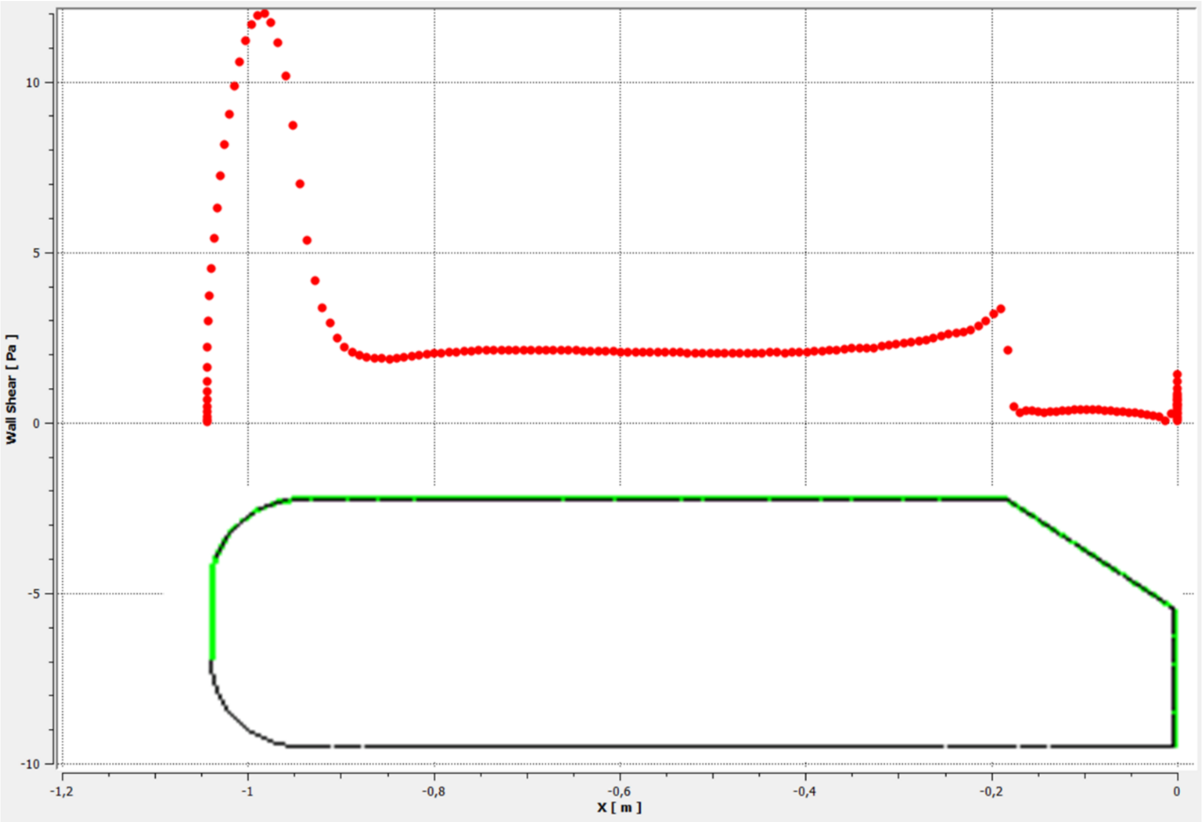

Figure 4-38 Wall shear stress distribution at the upper surface (original geometry).

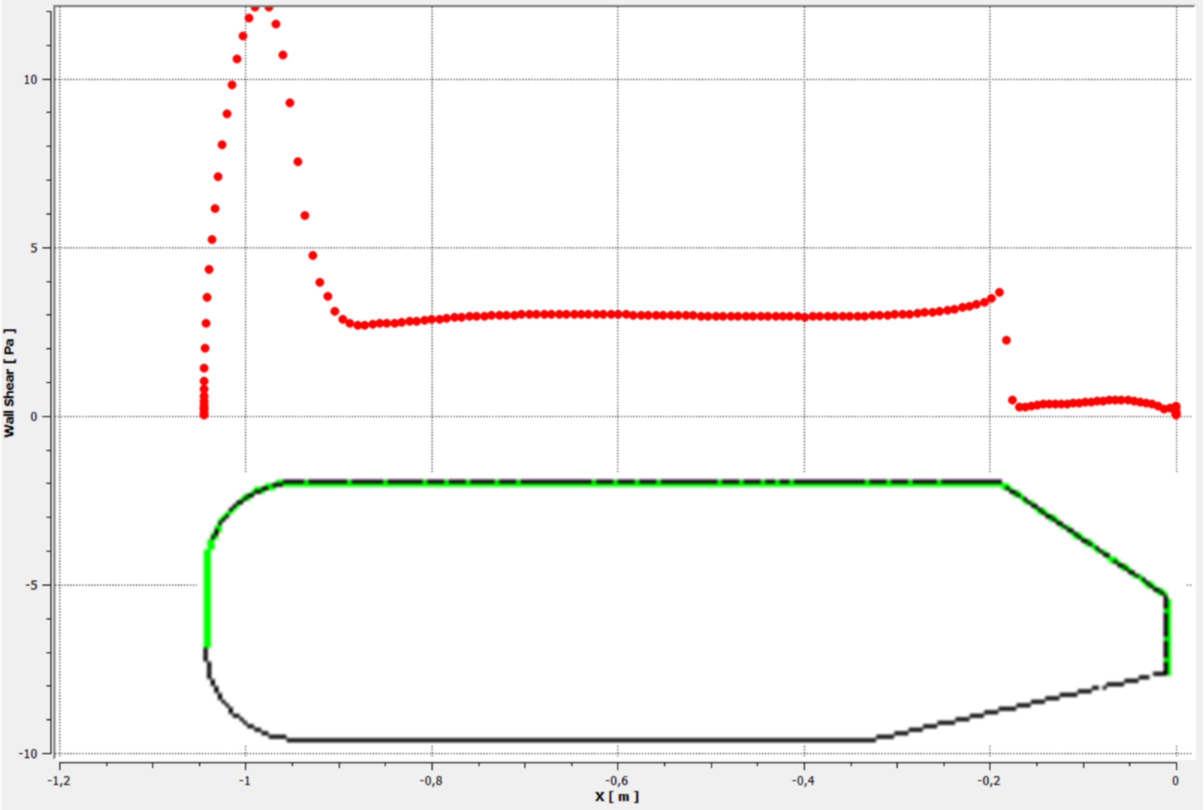

Figure 4-39 Wall shear stress distribution at the upper surface (optimized geometry).

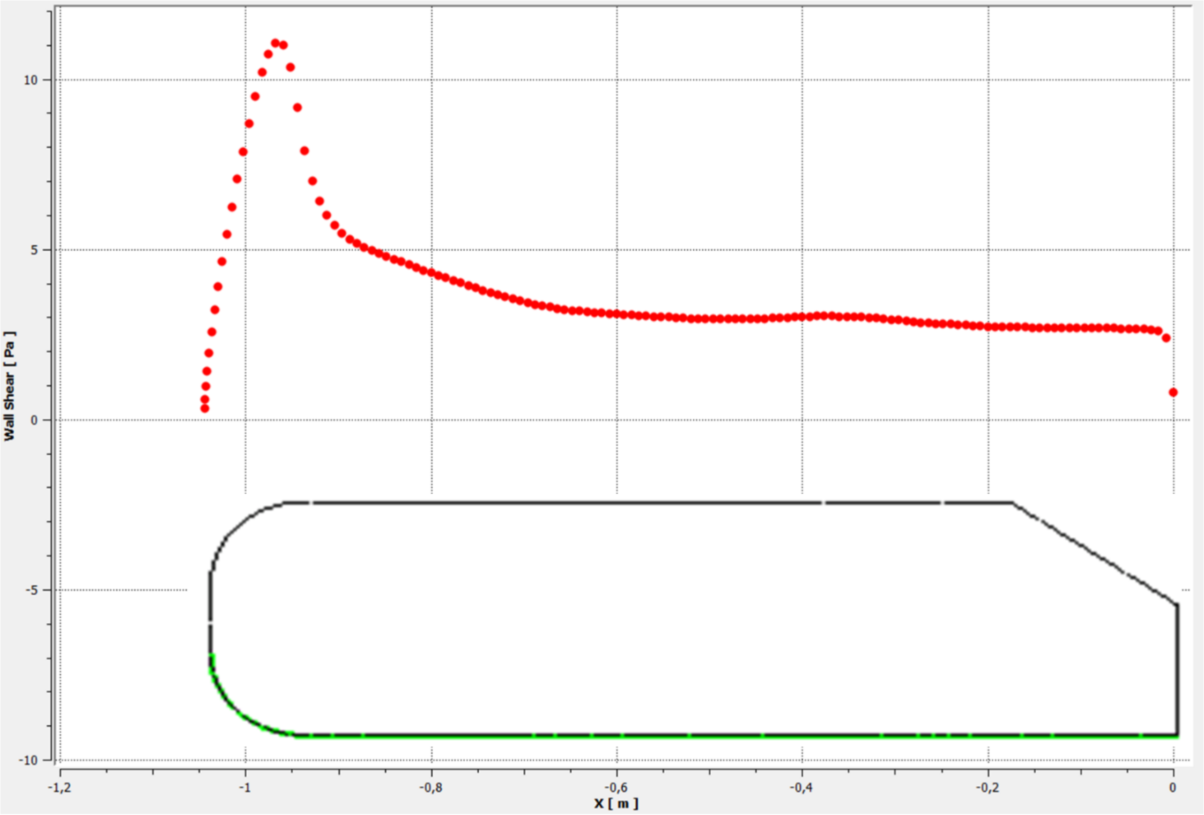

Figure 4-40 Wall shear stress distribution at the bottom surface (original geometry).

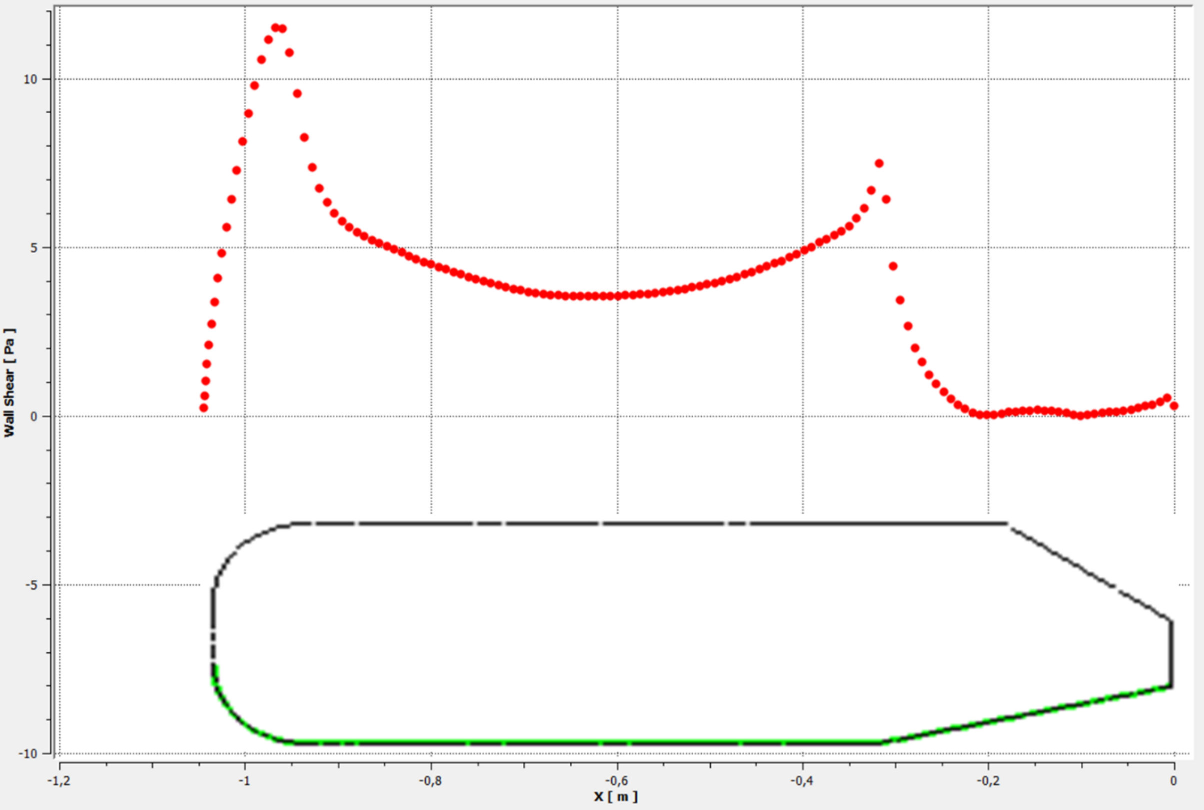

Figure 4-41 Wall shear stress distribution at the bottom surface (optimized geometry).

After we analyse the features of the flows around the original geometry and around the optimized geometry of the Ahmed body, we can see the amount vertical force and horizontal force the rear diffuser added. Table 4-5 shows the forces at upper and bottom surfaces of original geometry and optimized geometry.

The rear diffuser implementation had a strong impact at the downforce increasing the negative vertical force by around 810%, due the flow changes (analysed before). However, it also caused an increase in the drag represented by horizontal force. That increase corresponded to 5% compared with the geometry without rear diffuser.

Table 4-5 Shows the force contribution for drag and lift at upper and bottom surfaces.

	Surface	Vertical force (N)	Horizontal force (N)
Original geometry	Top	51.73	12.63
	Bottom	-51.18	4.48
	Total	0.55	17,11
Optimized geometry	Top	46.78	7,09
	Bottom	-91.31	10,85
	Total	-44.53	17,94
% Difference		810%	5%

4.5 Car GCI study

Just like in the Ahmed body case, we started by conducting studies to make sure that we have an appropriate mesh, considering accuracy and computational time. To ensure that, we performed a GCI study considering three successively finer grids.

Table 4-6 shows the results of the three simulations, for C_D and C_L coefficients associated to each grid size. The constant refinement ratio used was $r = 2$; that is, the next finer mesh should have half of the grid space of the previous one. The third column show the grid size normalized to be used for the GCI study.

Table 4-6 Car geometry GCI study results.

Grid	N° Elements	Grid Spacing (normalized)	C_D results	C_L results
A	$8x10^6$	1	0.123	-0.367
B	$4x10^6$	2	0.124	-0.370
C	$2x10^6$	4	0.128	-0.418

The results from Table 4-6 were used to make to different studies, one considering C_D and other considering C_L results. The two results were compared to understand how accurate the simulations were for both parameters.

4.5.1 GCI study from C_D results

Firstly, we determined the order of convergence:

$$P = 2.157$$

We then applied Richardson extrapolation using the two finest grids to obtain an estimate of the value of the C_D at zero grid spacing:

$$Cd_{h=0} = 0.122$$

The grid convergence index for the fine grid solution can now be computed. A safety factor of **FS**=1.25 was used since three grids were used to estimate **p**. The **GCI** for grids 1 and 2 was:

$$GCI_{12} = 0.272$$

The **GCI** for grids 2 and 3 was:

$$GCI_{23} = 1.207$$

We can now check whether the solutions were in the asymptotic range of convergence:

$$\frac{GCI_{23}}{r^p * GCI_{12}} = 0.992$$

which is approximately one and indicates that the solutions are well within the asymptotic range of convergence.

Based on this study we could say that the C_D (drag coefficient) for the car geometry is estimated to be $\boldsymbol{C_D}$ **= 0.122** with an error band of **0.272%**.

4.5.2 GCI study from C_L results

We employed the same procedure as for the GCI study from C_D results. The order of convergence was:

$$p = 3.687$$

The result of the Richardson extrapolation using the two finest grids to obtain an estimate of the value of the C_L at zero grid spacing was:

$$Cl_{h=0} = -0.366$$

The grid convergence index for grids 1 and 2, considering **FS**=1.25, was

$$GCI_{12} = 1.349$$

The **GCI** for grids 2 and 3 was:

$$GCI_{23} = 0.105$$

The solution is in asymptotic range of convergence, because

$$\frac{GCI_{23}}{r^p * GCI_{12}} = 0.990$$

Based on this study we could say that the C_L (lift coefficient) for the car geometry is estimated to be $\boldsymbol{C_L}$ **= -0.366** with an error band of **0.105%**.

From the results obtained in the GCI study we considered Grid 2 the best option. This option gives an acceptable error and reasonable computational time.

4.6 Car geometry optimization

The optimization loop was made in the same way as for the Ahmed body, using modeFRONTIER and Ansys Workbench. The aim of this simulation was test different combinations of height and length of the rear diffuser in order to get the minimum values of C_D and C_L.

The interval of height was 0.2 – 0.4 m and length 0.85 – 2.2 m. This value was chosen based on the original geometry and the previously study conducted which Ahmed body, also was taking into account geometry restrictions that a real car have, that can cause some interference in systems like powertrain and suspension, or needing to redesign these systems depending the priority of aerodynamic under the other systems. We start the simulation with 5 DOE (Design of experiments). We ran the loop for 10 generations, and each generation had 5 individuals. Therefore, we performed 50 simulations in the optimisation study. Based on the tests made with the Ahmed body, we employed the FAST algorithm for the optimisation. Figure 4-42 shows the optimization loop results.

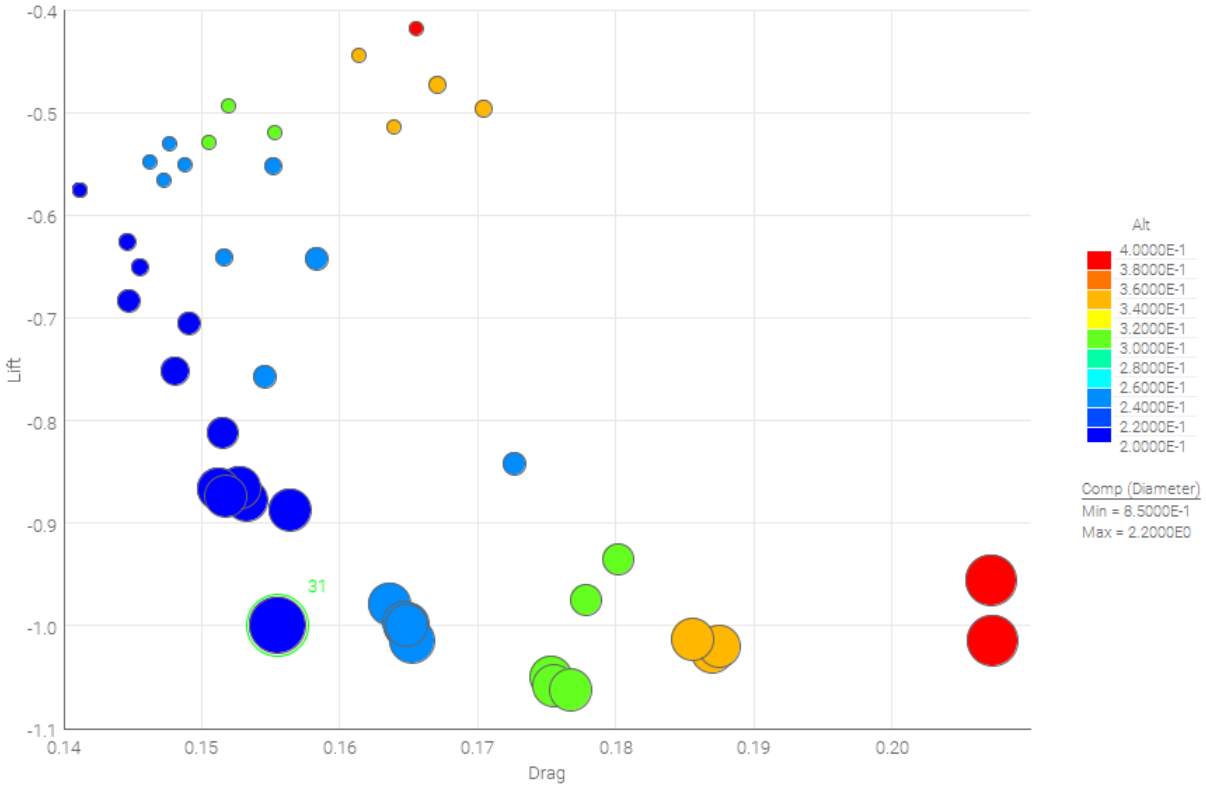

Figure 4-42 Shows the results of FAST optimizer algorithm applied to rear diffuser dimensions applied to Car Geometry. This is a 4D bubble chart, vertical axis represents lift coefficient, horizontal axis represents drag coefficient, the bubble diameter refers to diffuser length and bubble color refers to diffuser height.

During the simulations we can notice that the FAST algorithm converged quick for this case, since after few simulations it was already possible to see the Pareto frontier formation. At the end of 10 generations and 50 simulations we obtained a well-defined Pareto frontier.

We can see that both the Low drag and High downforce cases exhibit a limit of efficiency; if the rear diffuser height increased more than 370 mm the drag increased and downforce decreased. That could happen because the angle the flow exits is so hight that the flow detaches from the surface and creates a separation zone. Point 31 is the more efficient, we can see the details in Table 4-7.

Table 4-7 Data for rear diffuser optimized geometry chosen.

Geometry Parameters (input)		Aerodynamic Parameters (output)		
Height	Lenght	C_D	C_L	Aerodynamic efficiency
0.20 m	2.2 m	0.155	-0.998	6.44

Compared with the original geometry results, the optimized case with rear diffuser proved satisfactory. Table 4-8 shows a percentual difference between C_D and C_L for both cases.

Table 4-8 Comparison between drag and lift coefficients for optimized and original geometry.

	Original Geometry	Optimized Geometry	% difference
C_D	0.146	0.155	6%
C_L	-0.378	-0.998	164%

We could not minimize both parameters simultaneously, because they are inversely proportional quantities. However, considering a race car, the aim is to increase the performance and decrease the lap time, and to do that the more effective mechanism is create downforce. The differences between original geometry and optimized geometry are shown in Figure 4-43, Figure 4-44Figure 4-45 and Figure 4-46.

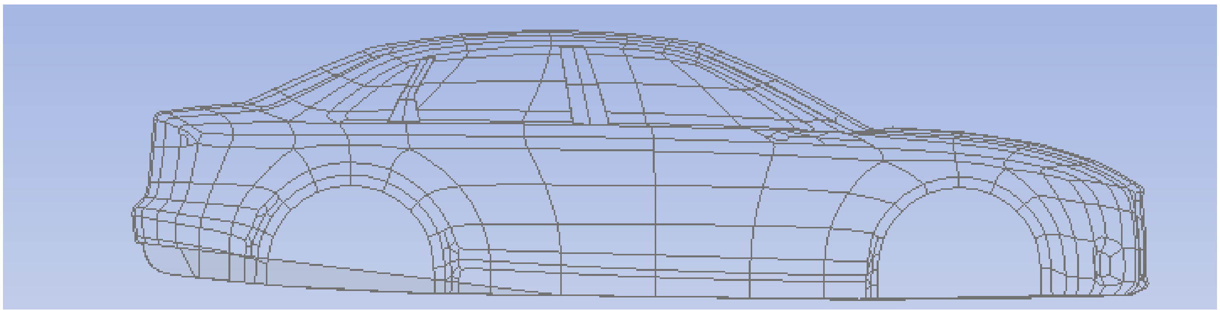

Figure 4-43 Car optimized geometry (rear diffuser).

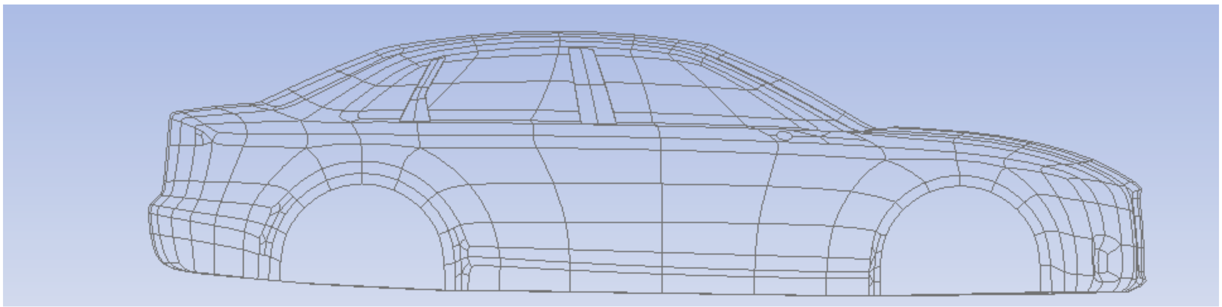

Figure 4-44 Car original geometry.

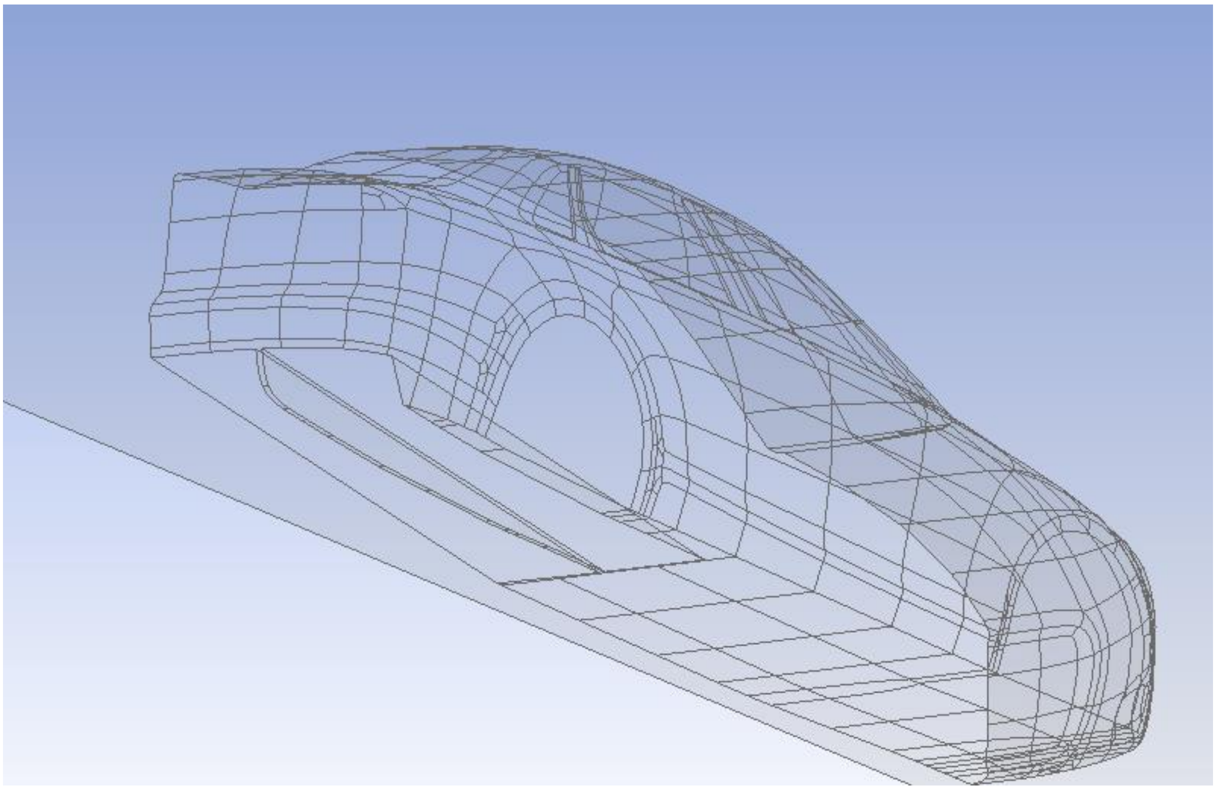

Figure 4-45 Car optimized geometry (rear diffuser).

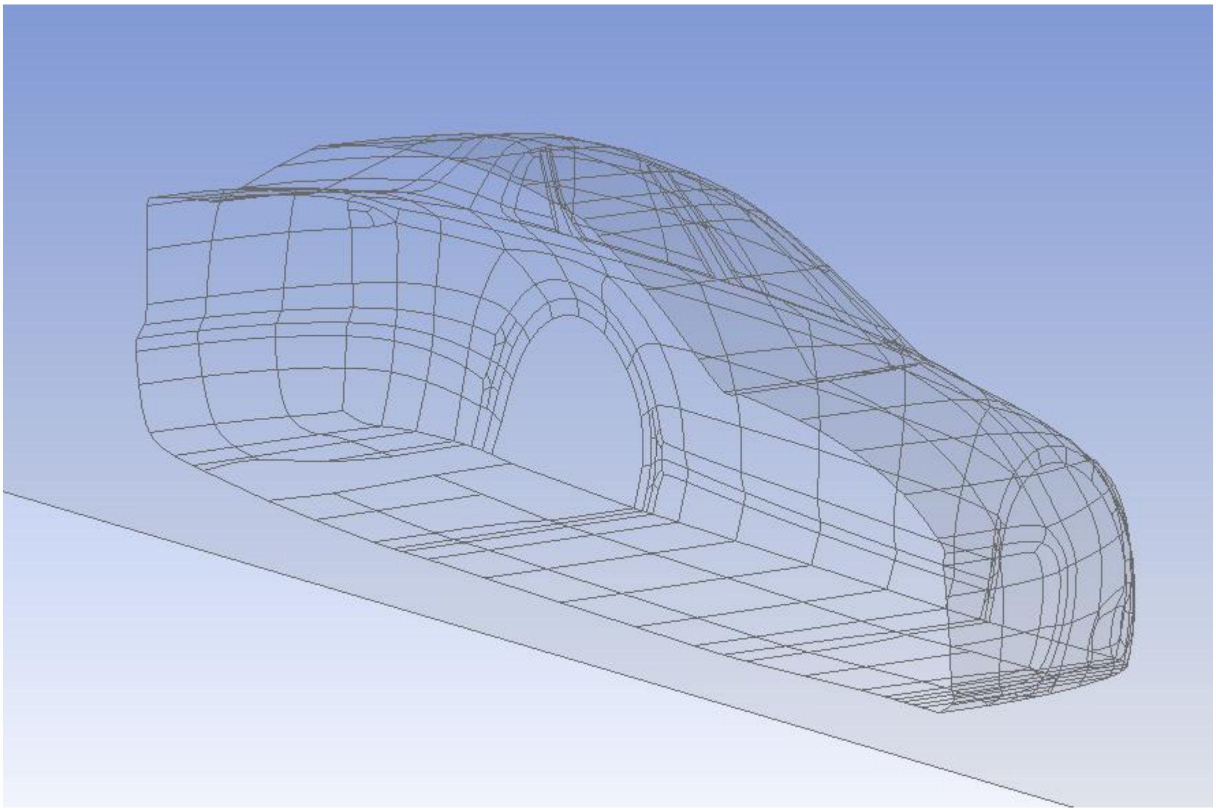

Figure 4-46 Car original geometry.

4.7 Comparison between Car standard geometry and optimized geometry

In this section the flow characteristics of rear diffuser will be presented and discussed from different points of view. The original and optimized case will be analysed with the aim to understanding what geometry modifications influenced the flow characteristics to result in the improvement in downforce and drag.

The optimized case chosen was the most efficient geometry in terms of downforce without a large drag penalty. Considering that the first concerns the improvement of the car grip and consequently reduction of lap time, in this scenario the lift coefficient plays a very important role.

The results are displayed using tables, charts and scalar scenes, followed by discussions.

4.7.1 Contours of velocity magnitude

The car geometry presents a behaviour in many ways similar to that of the Ahmed body. Looking at the contours of velocity magnitude (Figure 4-47 and Figure 4-48), we can notice a stagnation point at the front (Bumper). Looking to where windshield meets the roof there is an acceleration of the flow for both cases. However, when we look underneath it is possible to see that the flow accelerates more in the optimized than the original case, this is due the suction created by the rear diffuser. This suction is responsible for the creation of downforce.

There is an important difference in the wake structure between the two cases: in the optimized geometry looks that the flow separated too early compared to the original case. This can be responsible for the increase in drag and reduces the efficiency of rear diffuser.

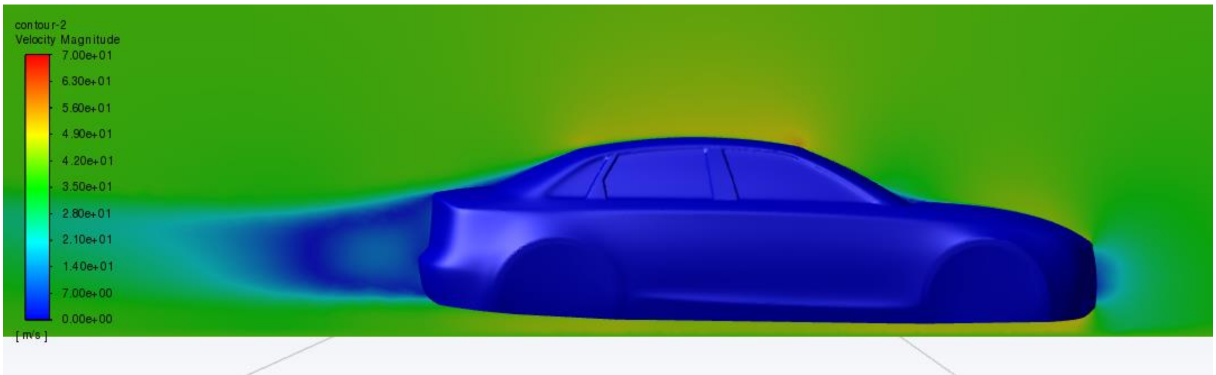

Figure 4-47 Contours of velocity of the car original geometry.

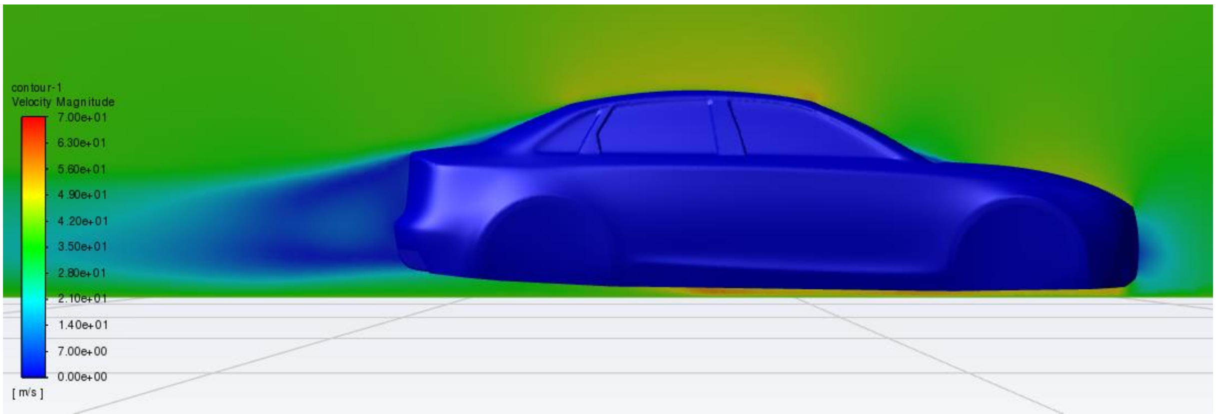

Figure 4-48 Contours of velocity of the car optimized geometry.

4.7.2 Contours of static pressure

The car presents a high pressure point at the front bumper, and another expressive high pressure point at the junction of the hood with the windshield (Figure 4-49 and Figure 4-50). These regions have a strong contribution in the total amount of drag for both cases.

Looking at underneath the car we can see the differences in the pressure distribution for the two geometries. Figure 4-51 shows a low-pressure zone underneath the front bumper, this zone is responsible for accelerating the flow towards the car floor. In Figure 4-51 we can see the same behaviour at the front bumper, the car floor has greener region than the original geometry. This is because the rear diffuser accelerates the flow in the car bottom surface. This flow acceleration is created due a low-pressure zone formed at the inlet of the diffuser. The low pressure generated in the bottom surface by the rear diffuser has a significant contribution to increase the downforce and minimize the lift coefficient.

Figure 4-49 Contours of static pressure of the car original geometry.

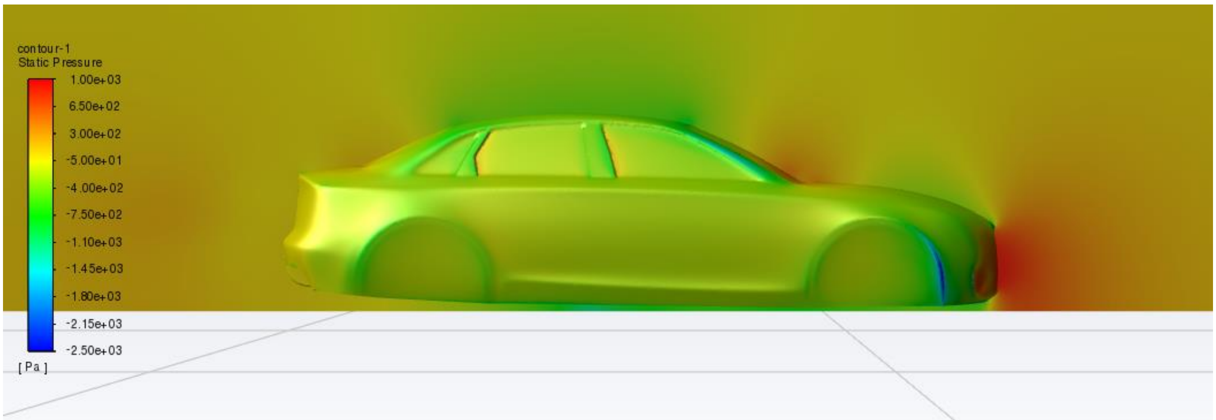

Figure 4-50 Contours of static pressure of the car optimized geometry.

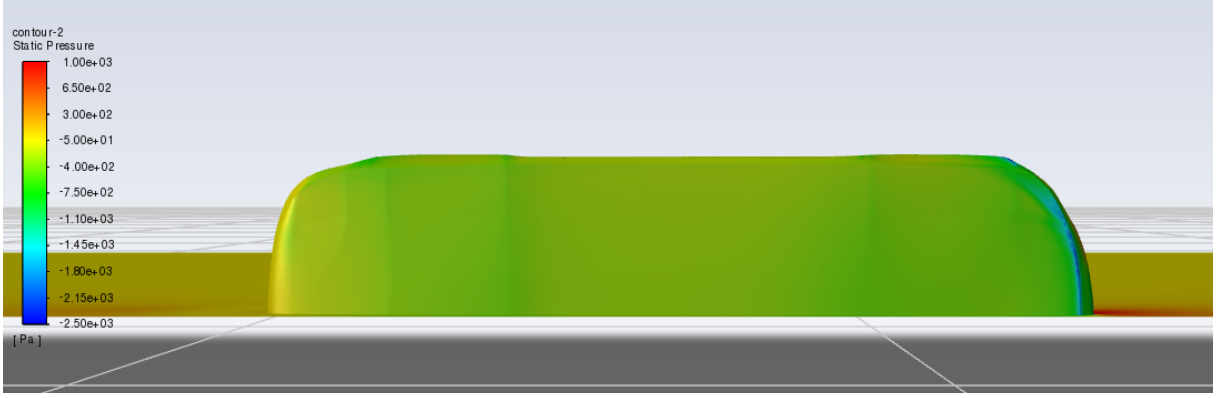

Figure 4-51 Contours of static pressure of the car original geometry bottom surface.

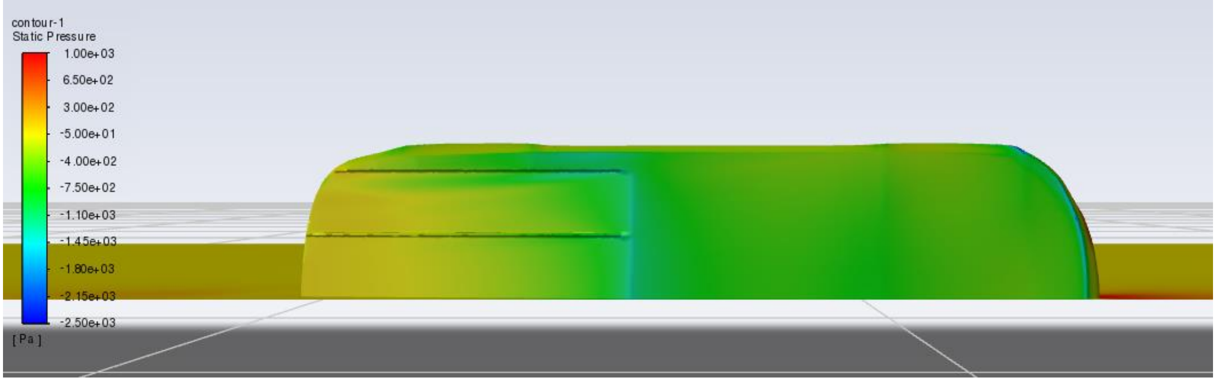

Figure 4-52 Contours of pressure of the car optimized geometry bottom surface.

4.7.3 Contours of turbulent kinetic energy

In Figure 4-53 and Figure 4-54 we can see the distribution of turbulent kinetic energy for both cases. In the original geometry we can notice more turbulent kinetic energy at the wake, this is due strong recirculating flow created behind the car favoring the eddies formation. This recirculation flow happens because of the low-pressure zone created behind the car. In the optimized geometry, the turbulent kinetic energy is lower due to the increase of pressure created by the rear diffuser behind the car. This increase of pressure changes completely the wake structure, accelerating the flow towards the exit of the rear diffuser.

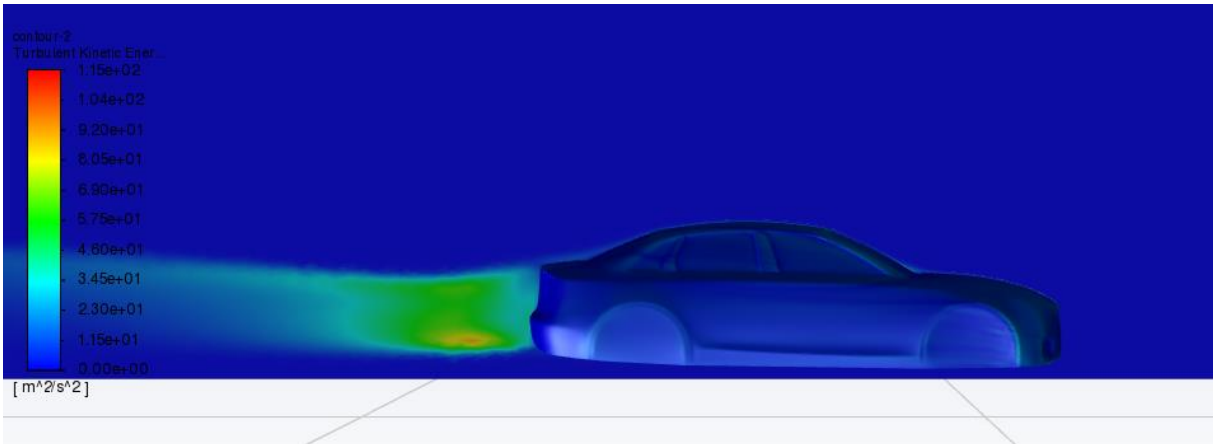

Figure 4-53 Contours of turbulent kinetic energy of the car original geometry.

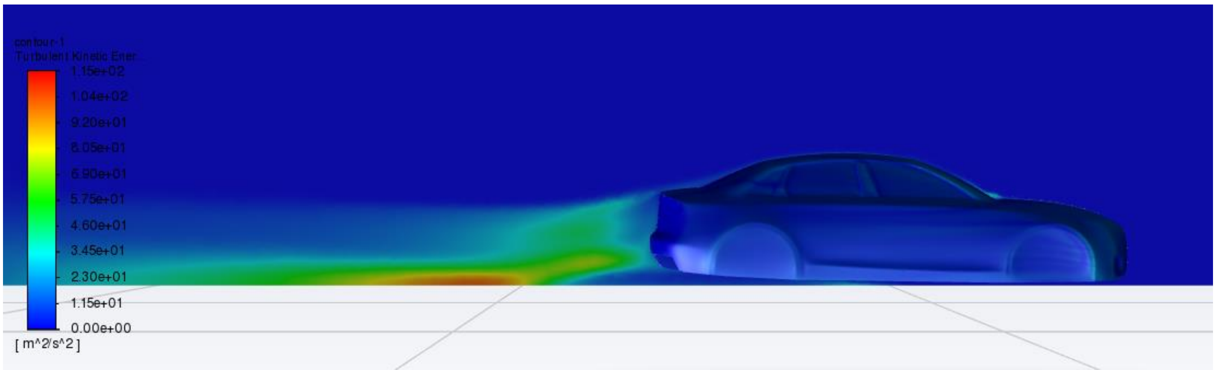

Figure 4-54 Contours of turbulent kinetic energy of the car optimized geometry.

4.7.4 Contours of wall shear stress

Looking at the upper surface, we can notice some blue regions. These regions are characterized by flow separation (Figure 4-55, Figure 4-56, Figure 4-57, Figure 4-58). At the front bumper the dark blue point represents the stagnation point. However, the dark blue zone on the windshield means that this region has a strong recirculation flow. Behind the car the there is a low-pressure region, which is a region with large flow separation as we can notice by the dark blue regions.

In the rear diffuser we can see a large dark blue region closes to the symmetry plane (Figure 4-59). This means that the flow detached from the surface, and it could happen because of the strong three-dimensional flow at this region. However, comparing with the original case (Figure 4-59), we can see that the floor flow is more attached in the optimized geometry (characterized by green and yellow region at the car floor). This is due to the suction that the rear diffuser creates.

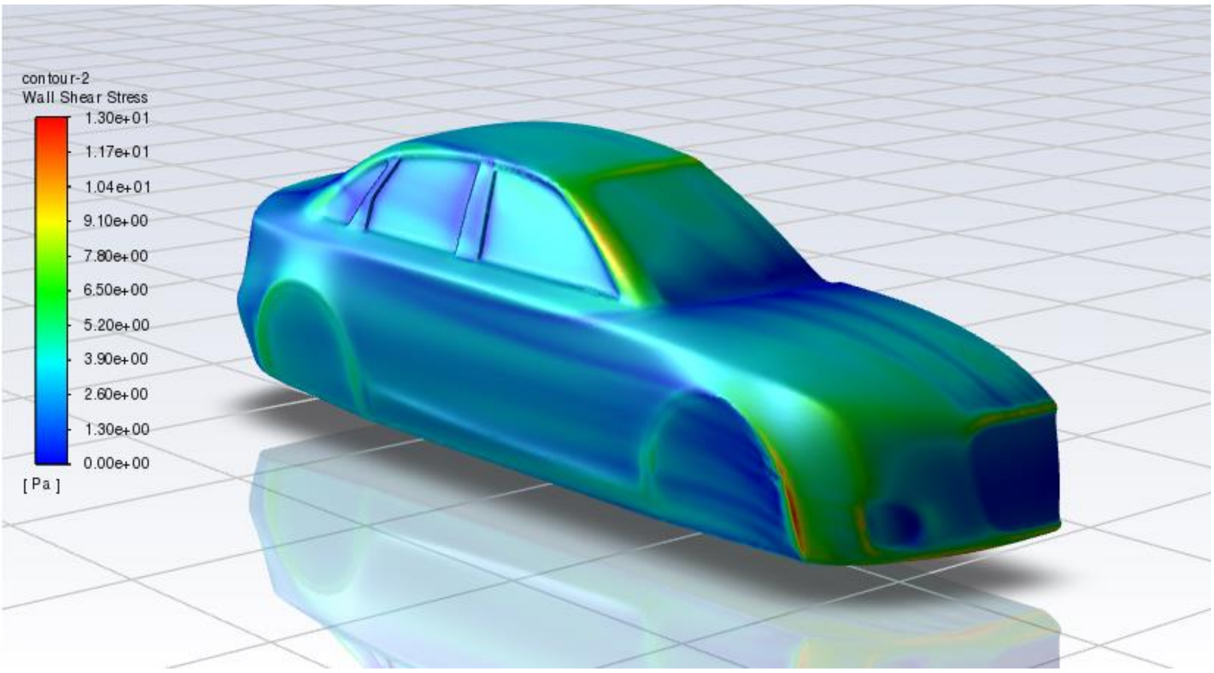

Figure 4-55 Contour of wall shear stress around the original car geometry.

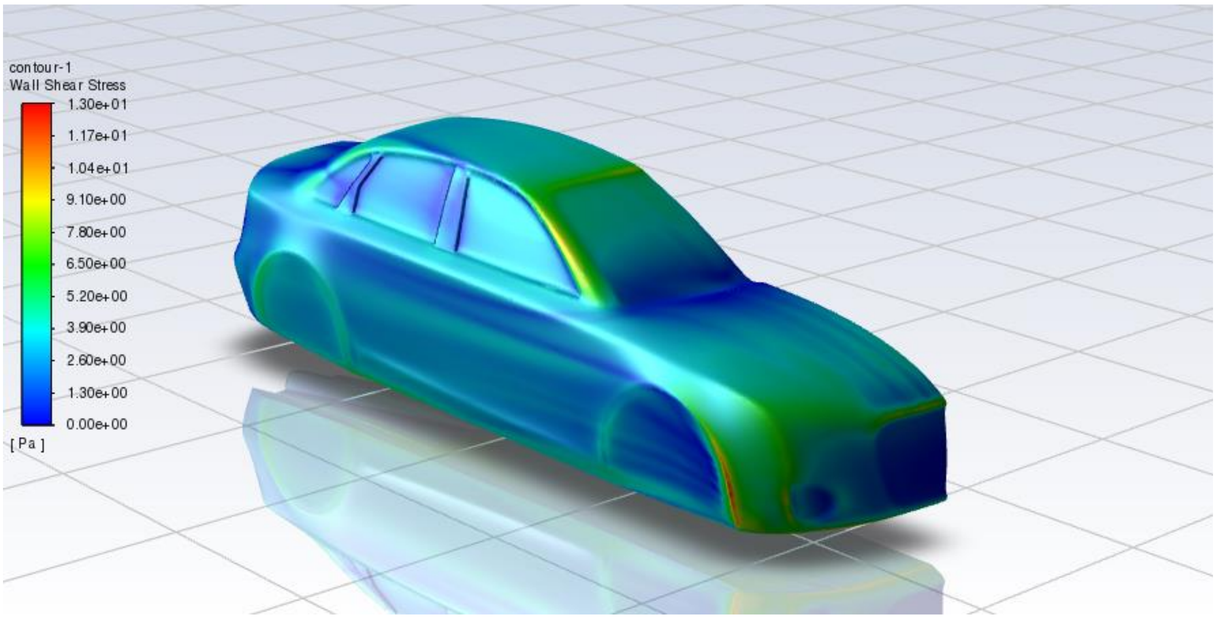

Figure 4-56 Contour of wall shear stress around the optimized car geometry.

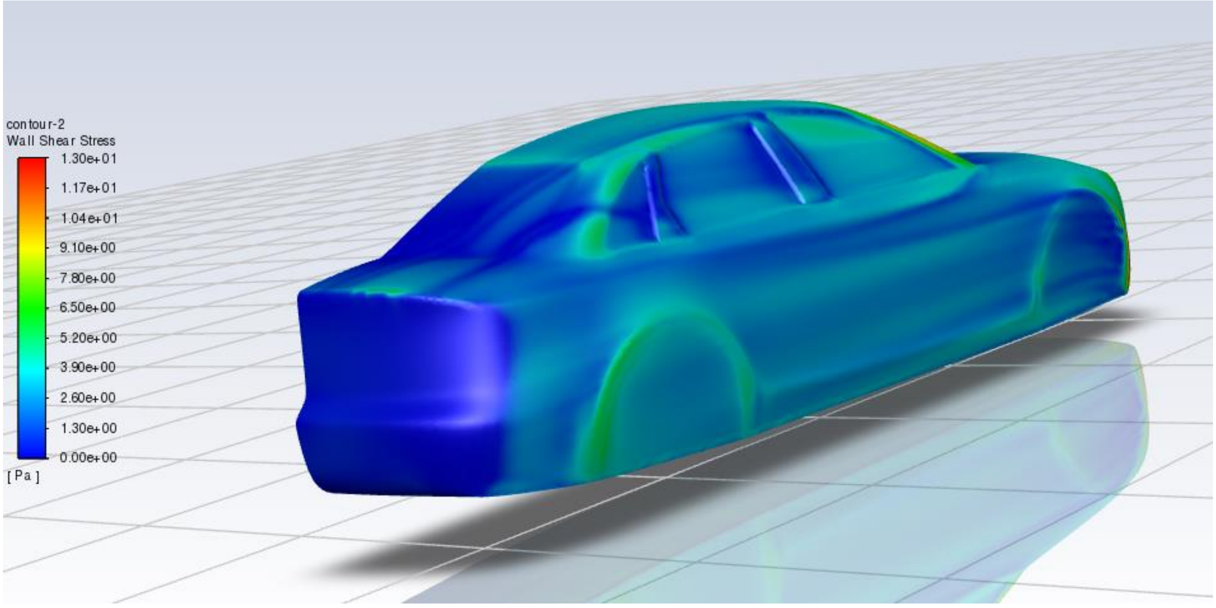

Figure 4-57 Contour of wall shear stress around the rear of the original car geometry.

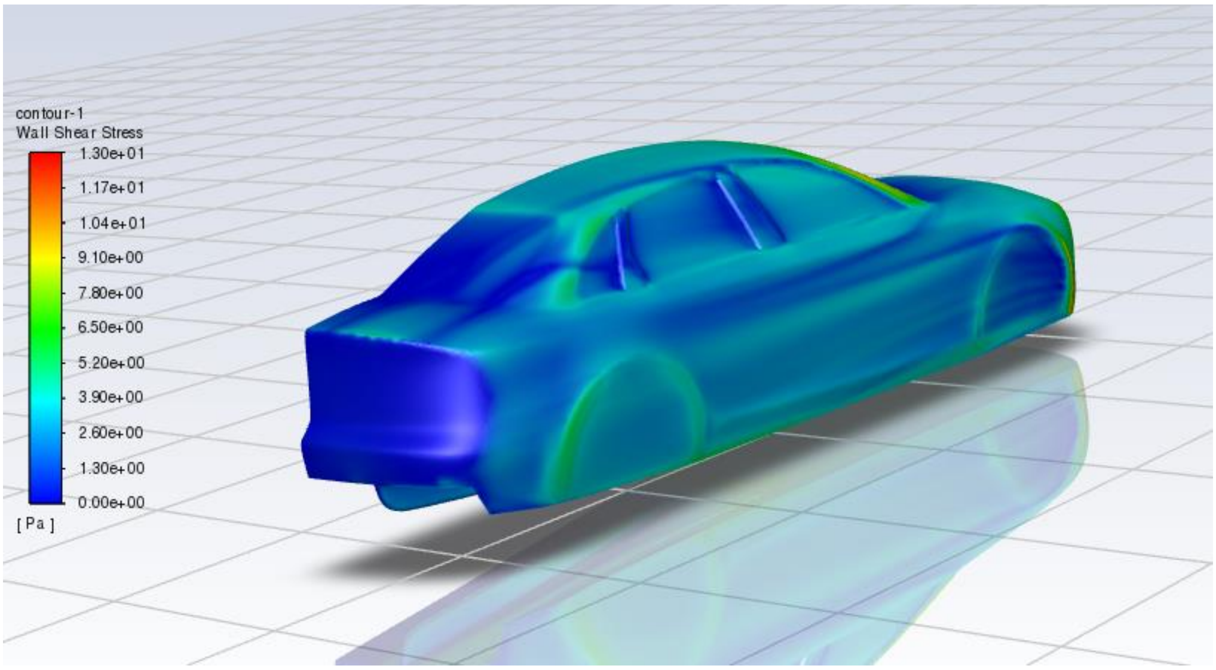

Figure 4-58 Contour of wall shear stress around the rear of the optimized car geometry.

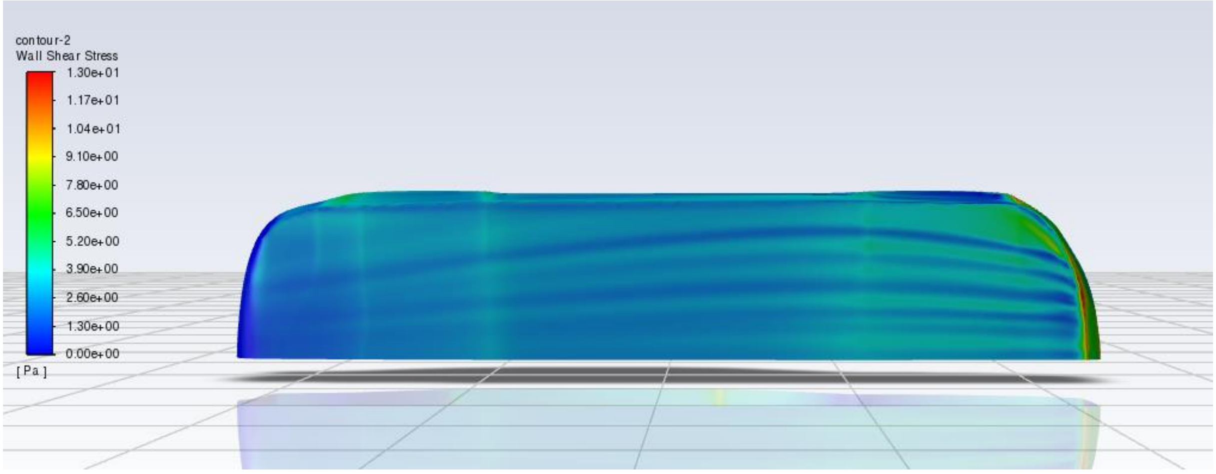

Figure 4-59 Contour of wall shear stress around the bottom surface of the original car geometry.

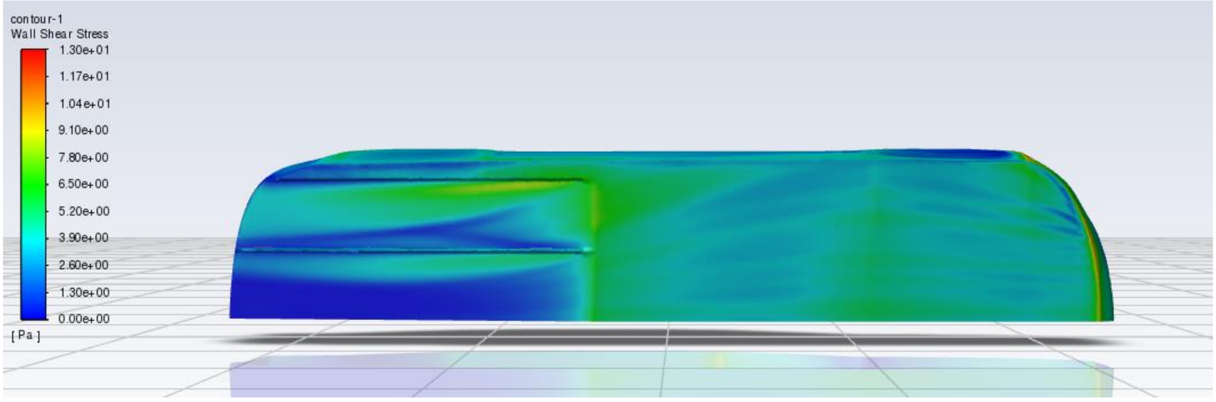

Figure 4-60 Contour of wall shear stress around the bottom surface of the optimized car geometry.

4.7.5 Velocity vectors

Velocity vectors make it possible to analyse the wake structure behind the car. When Figure 4-61 and Figure 4-62 are compared, we can see an important difference between the two cases. In original geometry case there is a two-vortex formation in the recirculation zone (Figure 4-63 and Figure 4-64). The wake structure for optimized case is completely different, being smaller than the original geometry. This has a positive effect in the drag coefficient, it can be responsible for not increasing a lot the drag force keeping a good aerodynamic efficiency of the rear diffuser.

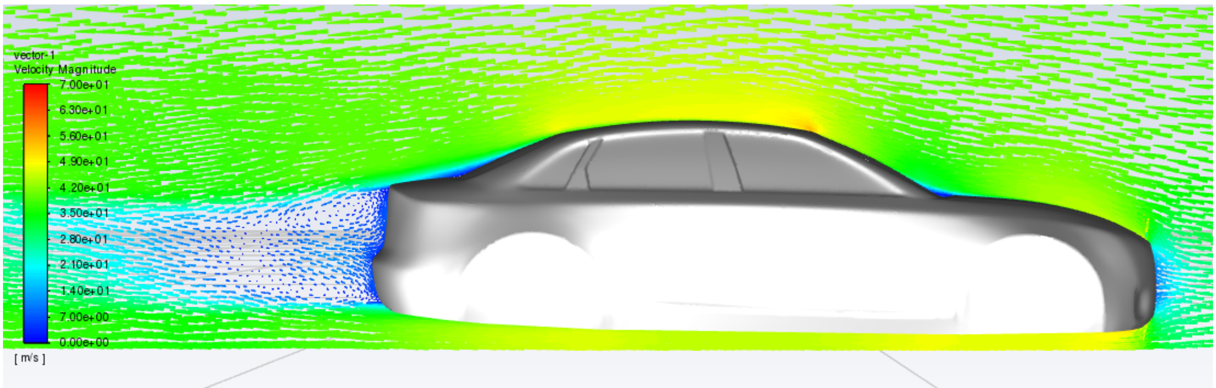

Figure 4-61 Velocity vectors around the car original geometry.

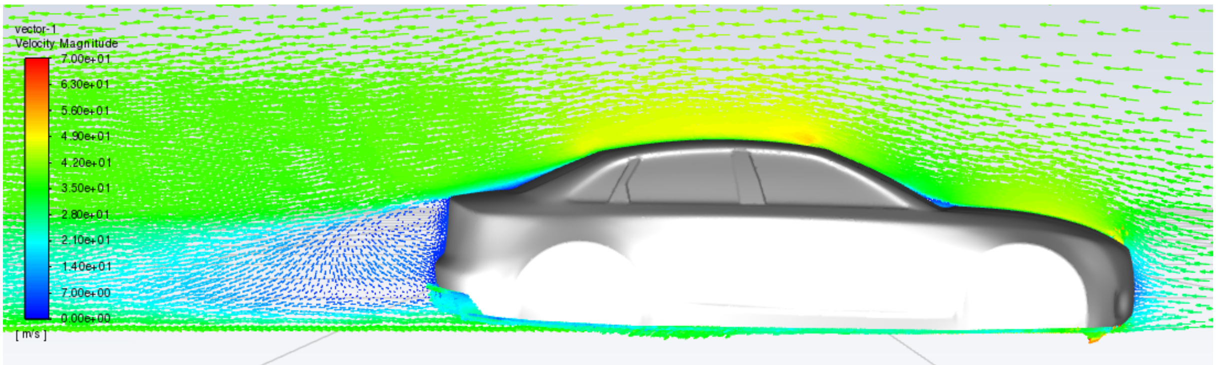

Figure 4-62 Velocity vectors around the car optimized geometry.

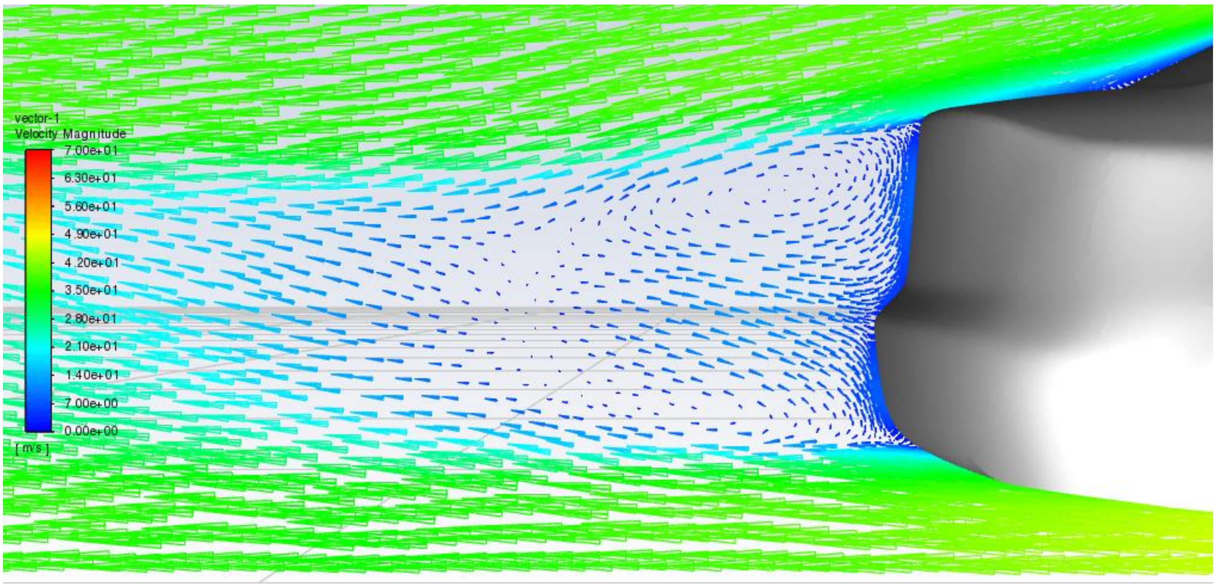

Figure 4-63 Velocity vectors in the near wake of the car original geometry.

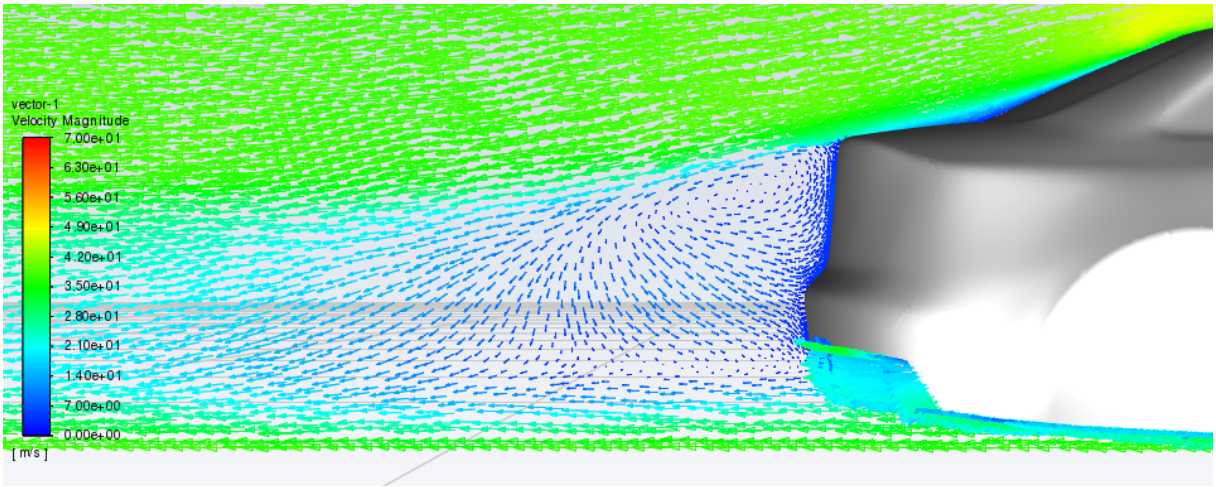

Figure 4-64 Velocity vectors in the near wake of the car optimized geometry

4.7.6 Pathlines

Looking at Figure 4-66, Figure 4-67, Figure 4-68, Figure 4-69 and Figure 4-70, we can see the changes in the wake flow caused by the rear diffuser. The floor flow is higher in optimized geometry it is due the higher exit angle of the rear diffuser and the high flow velocity caused by the rear diffuser suction. However, we can notice that at the end of the rear diffuser flow separation occurs. This contributes to increasing the drag force. This separation happens close to the symmetry plane because the strong three-dimensional flow at this region, which favours the formation of vortices. Looking at the figure we can clearly see the increase of velocity generated at the diffuser inlet.

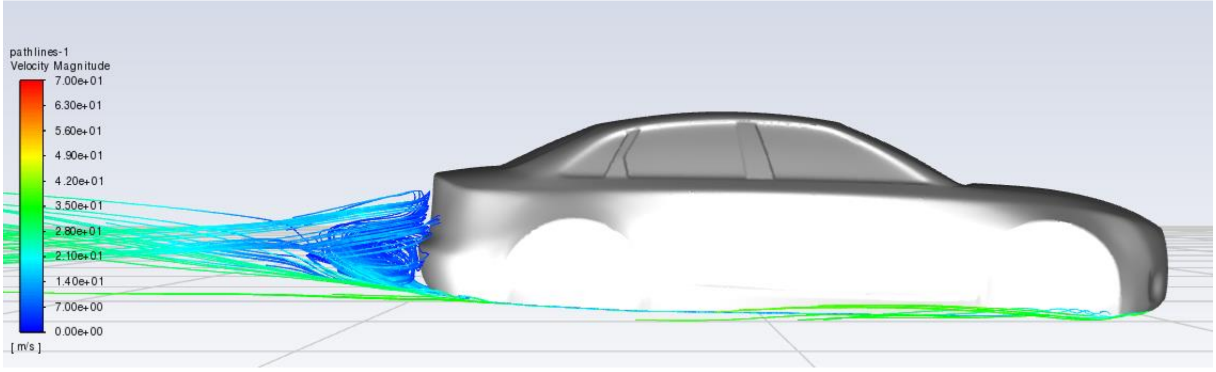

Figure 4-65 Pathlines around the original geometry originated from the bottom surface.

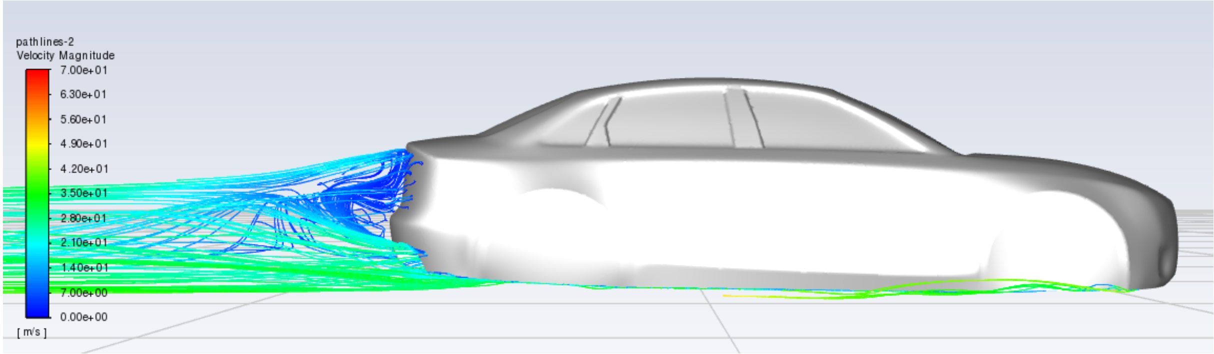

Figure 4-66 Pathlines around the optimized geometry originated from the bottom surface.

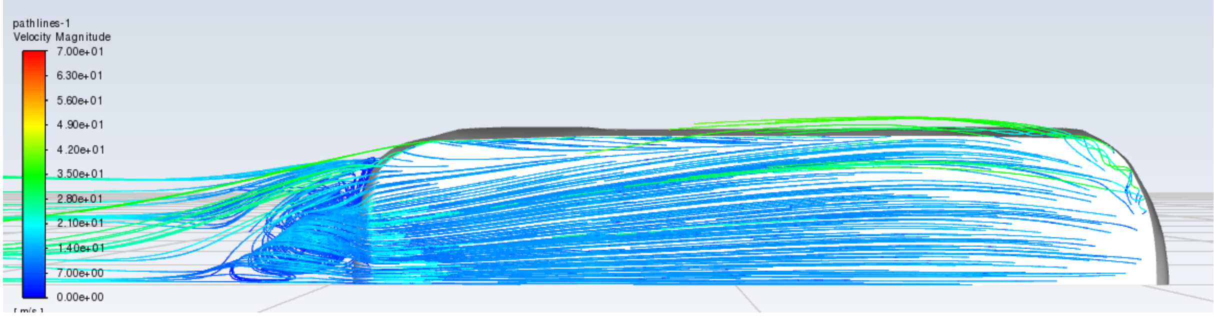

Figure 4-67 Pathlines around the original geometry floor.

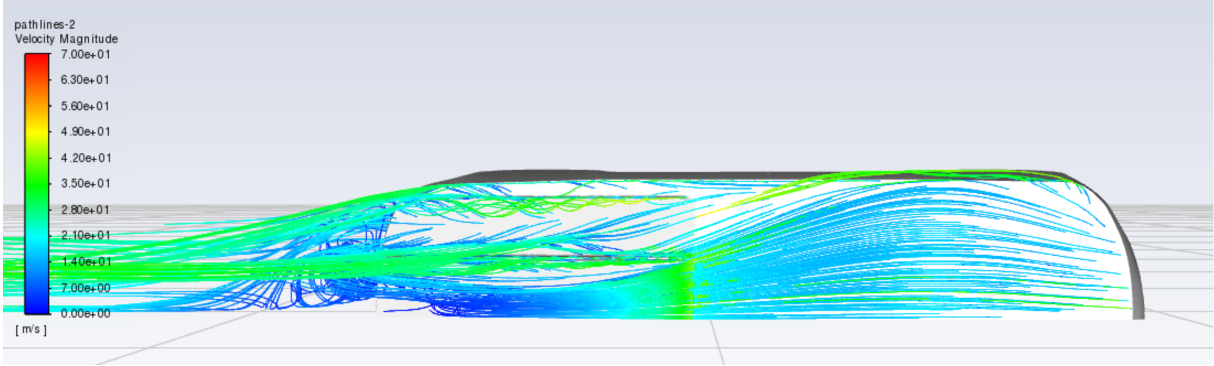

Figure 4-68 Pathlines around the optimized geometry floor.

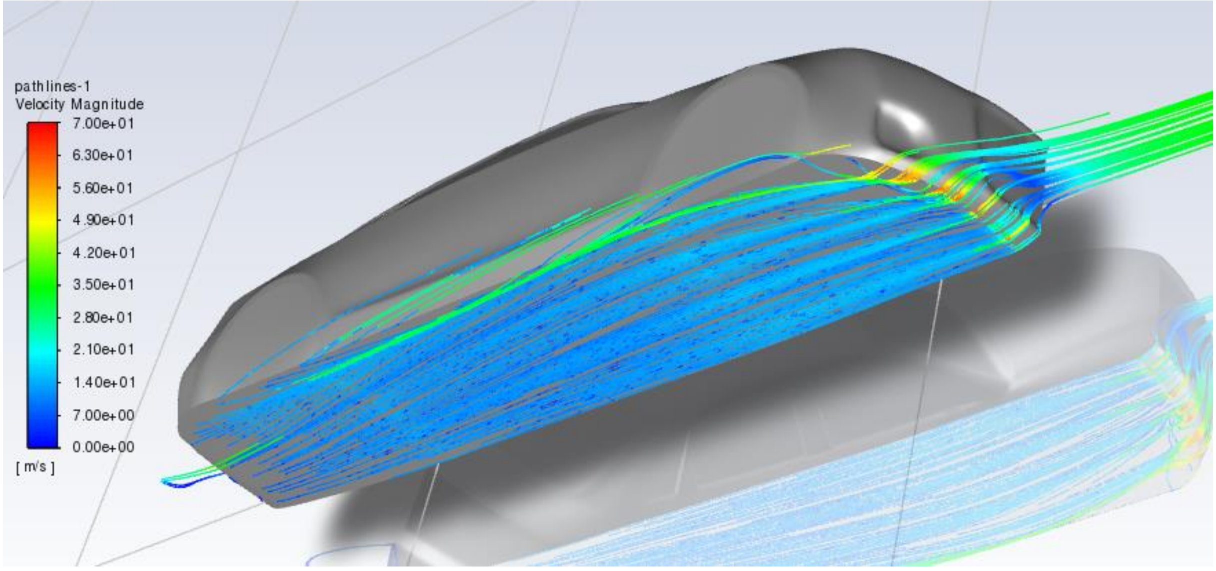

Figure 4-69 Pathlines around the original geometry floor.

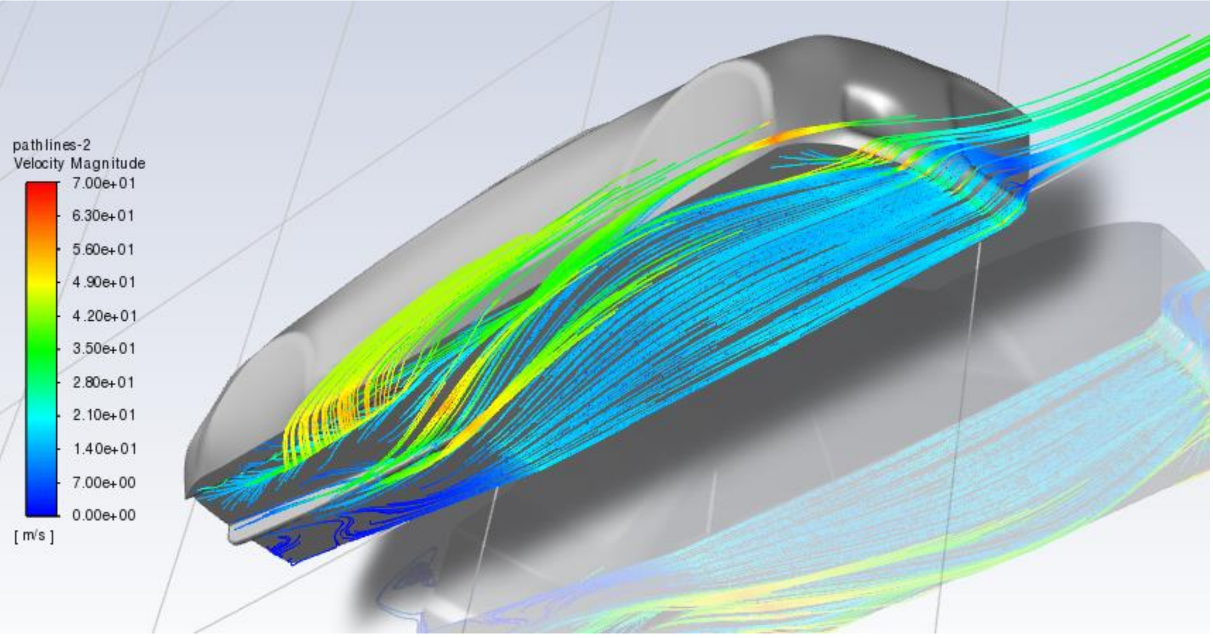

Figure 4-70 Pathlines around the optimized geometry floor.

4.7.7 Vertical force distribution

The distribution of vertical force along the upper surface is the same for both cases (it starts close to zero at the front bumper, increases across the hood according with the hood curvature, and decreases until negative values when this curvature changes). At the roof the vertical force was predominant positive, at the rear windshield the vertical became negative.

The negative values of vertical force happen in the separation zones. However, the vertical force in the upper surface is predominantly positive and that contributes to increase downforce.

The charts in Figures, shows a big difference in the vertical force distribution between the original geometry and optimized geometry. The implementation of rear diffuser creates a suction in car underneath doing the vertical force distribution assumes high negative values compared with original geometry. The peak of negative force happens in the rear diffuser inlet this increase the downforce improving the car performance.

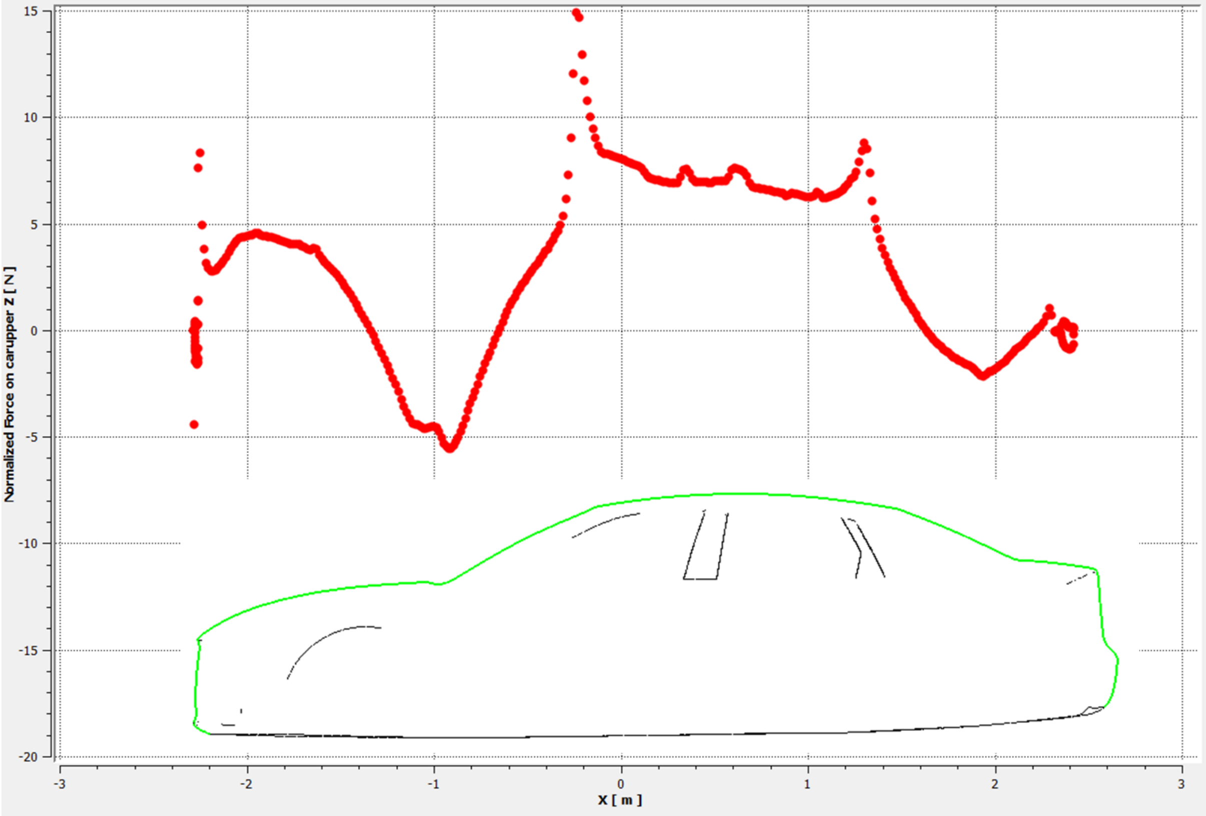

Figure 4-71 Vertical force distribution at the upper surface (original geometry).

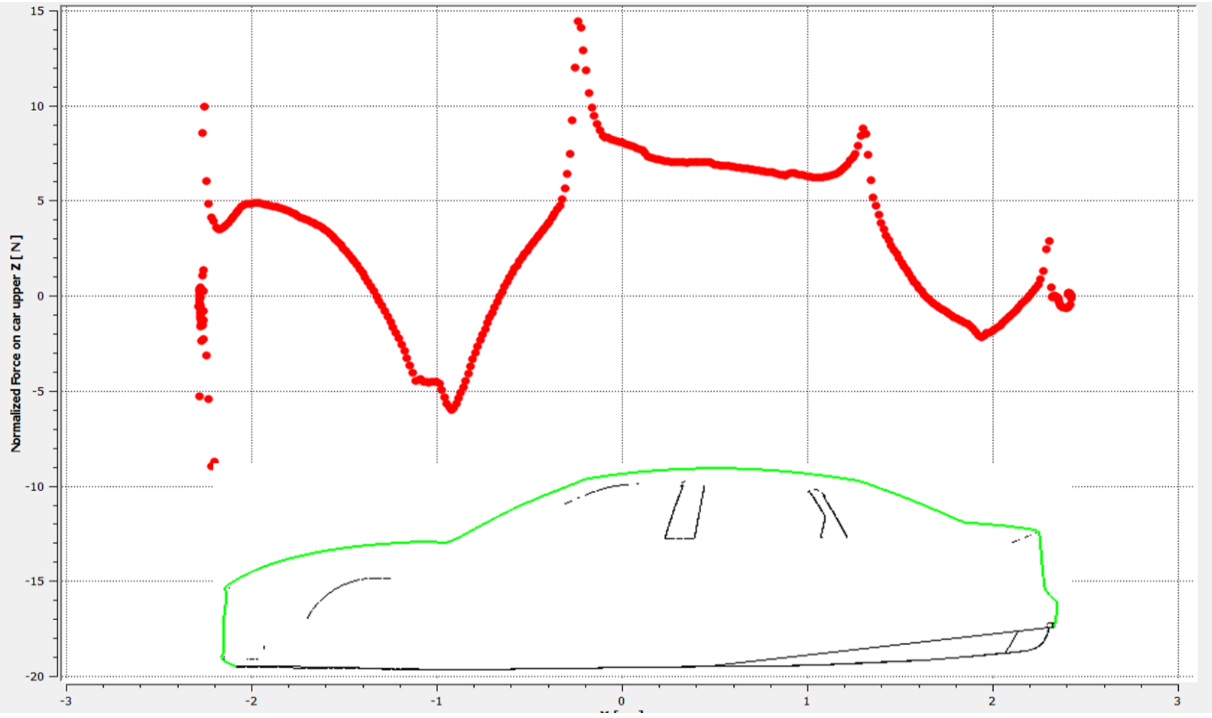

Figure 4-72 Vertical force distribution at the upper surface (optimized geometry).

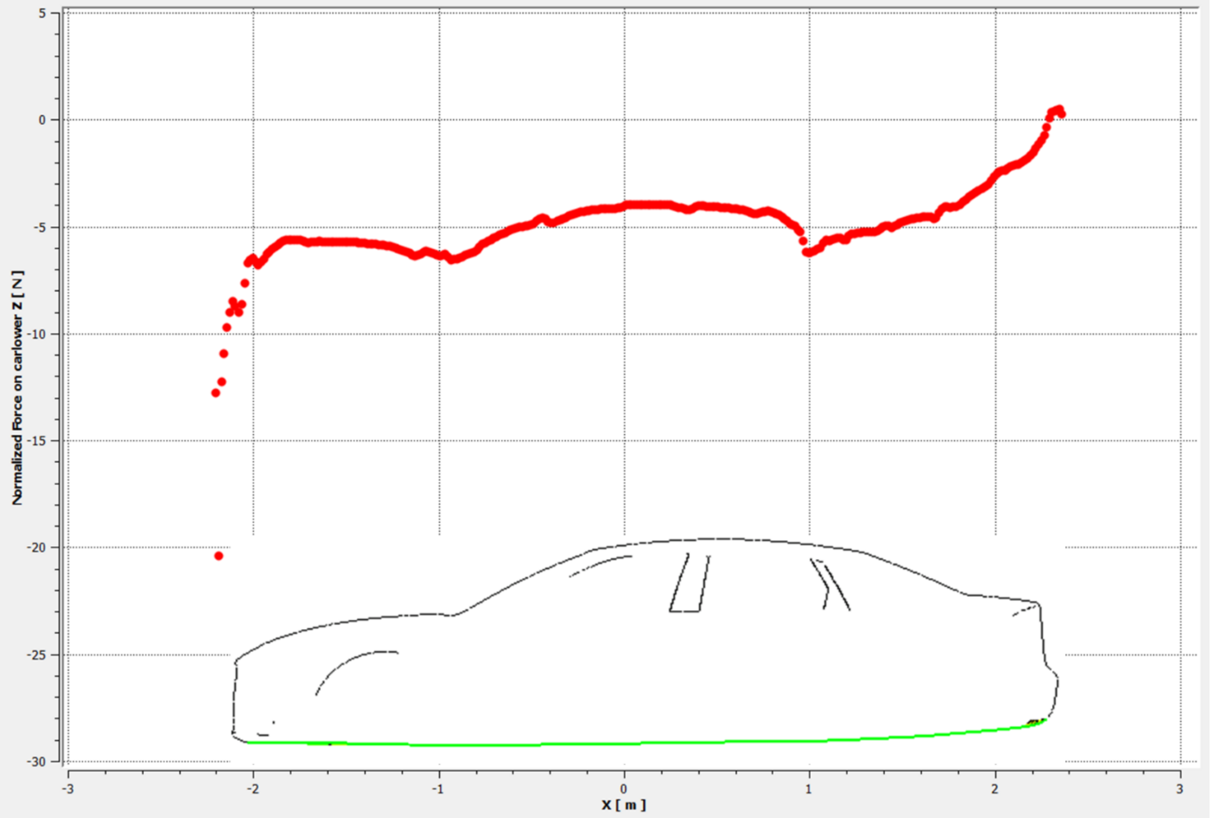

Figure 4-73 Vertical force distribution at the bottom surface (original geometry).

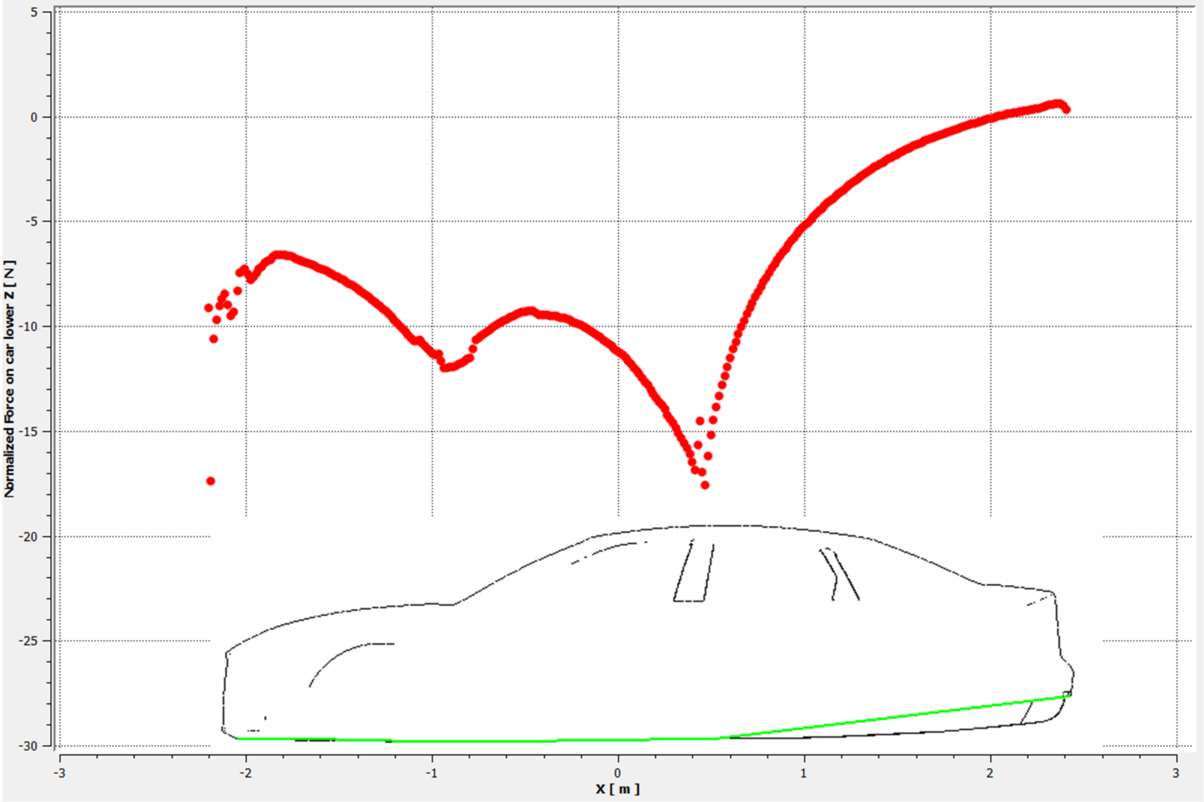

Figure 4-74 Vertical force distribution at the bottom surface (optimized geometry).

4.7.8 Horizontal force distribution

Through the horizontal force distribution, it is possible to identify the regions that are more relevant to increase the drag. Looking at Figure 4-75 and Figure 4-76, we see that there are no relevant differences between two geometries. The horizontal force reaches its highest value at the front bumper, that is due the stagnation point. The next region with high horizontal force values is the junction of the hood with the wind shield that can be explained by the high pressure seen in the pressure contours (Figure 4-49 and Figure 4-50). The junction between roof and rear windshield presents a slightly higher value of horizontal force due to the high wall shear stress at this point.

Figure 4-77 and Figure 4-78 show that both cases exhibit the same horizontal force distribution until the entrance of diffuser, the value is very close to zero. The force increases at the rear diffuser entrance reaching its maximum value, and decreases slightly until zero. This behaviour contributes to increasing the drag.

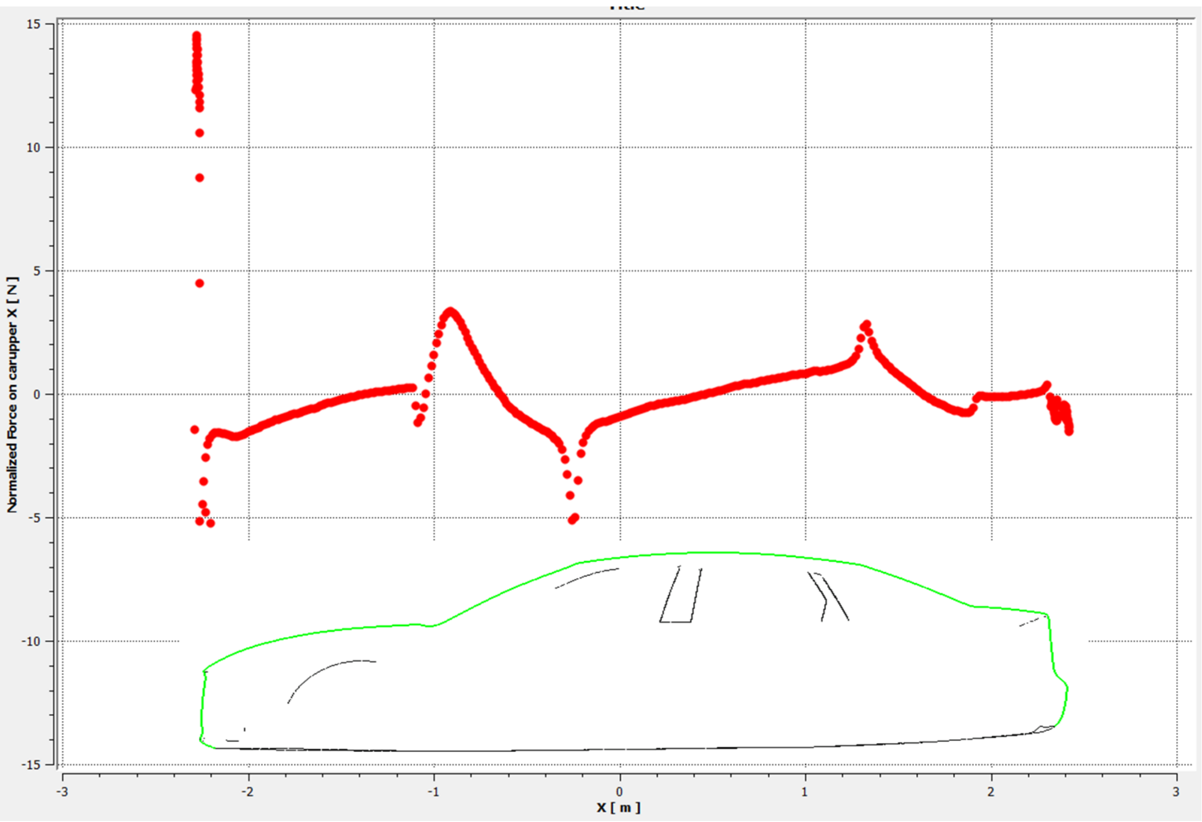

Figure 4-75 Horizontal force distribution at the upper surface (original geometry).

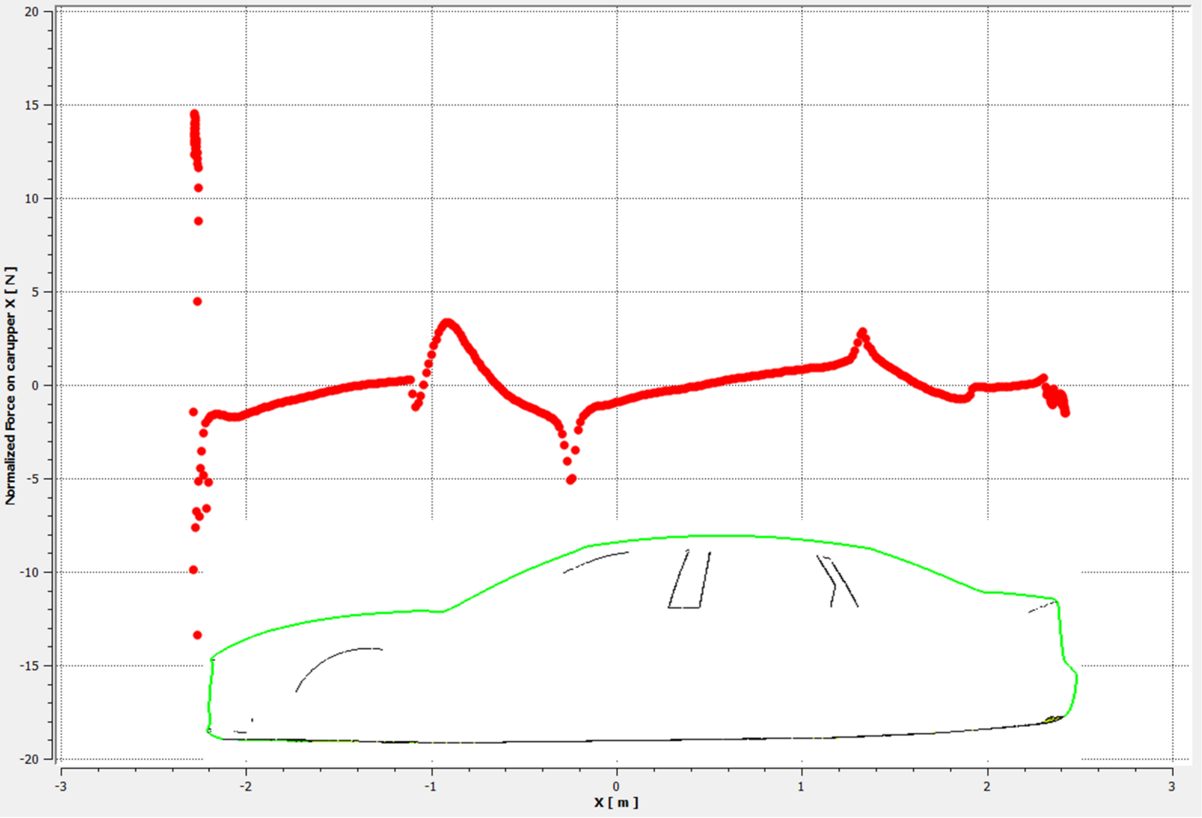

Figure 4-76 Horizontal force distribution at the upper surface (optimized geometry).

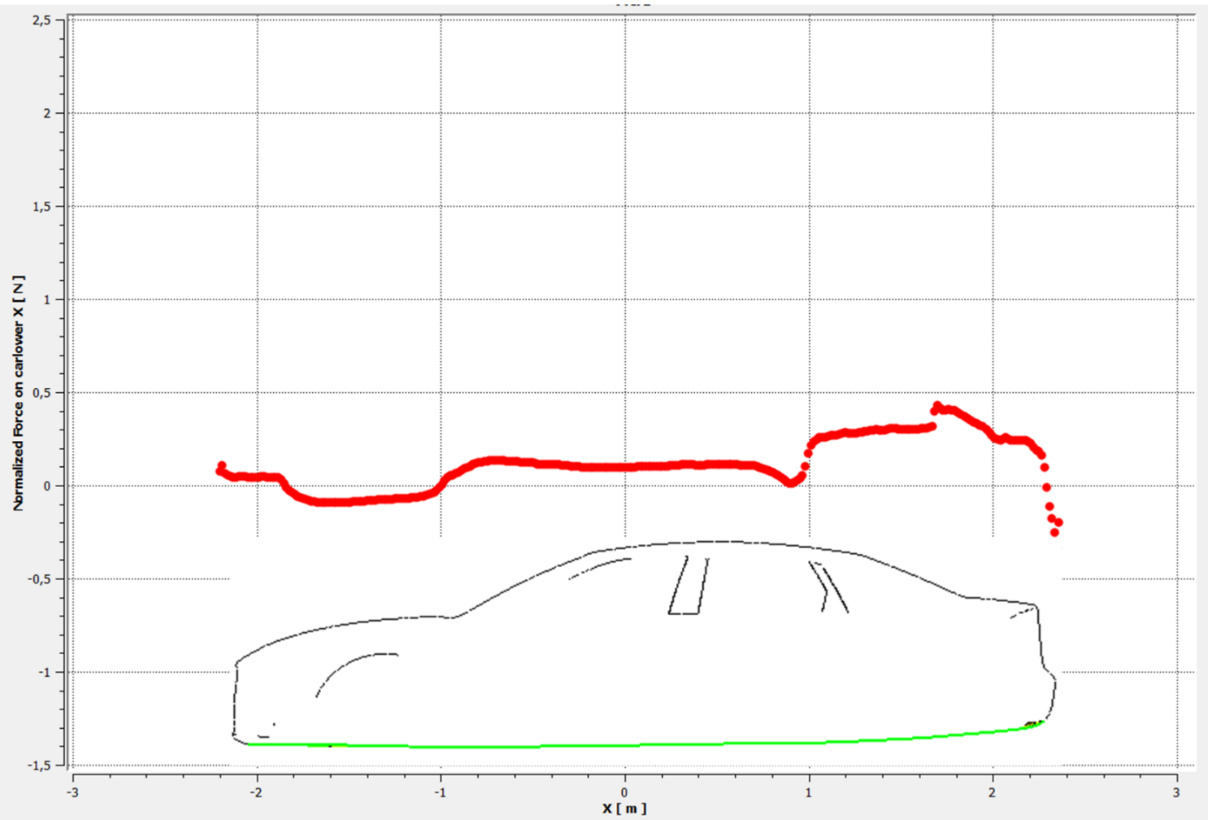

Figure 4-77 Horizontal force distribution at the bottom surface (original geometry).

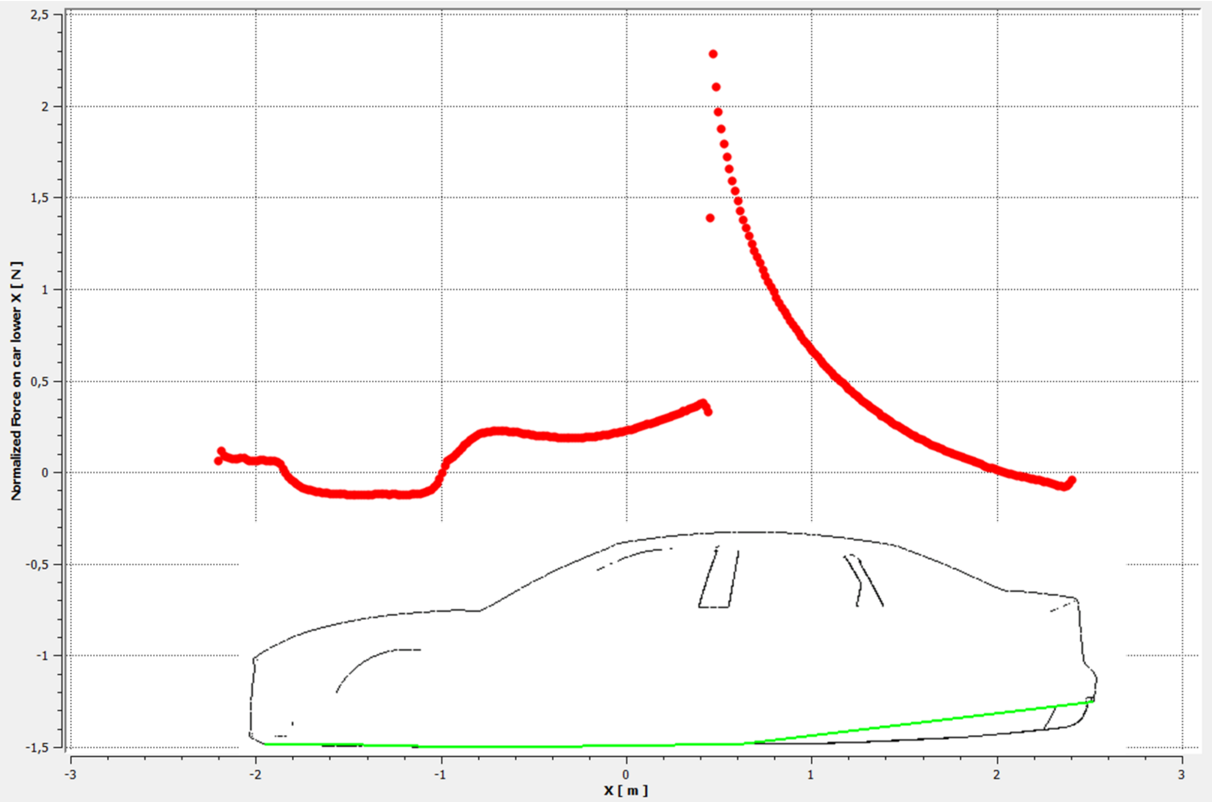

Figure 4-78 Horizontal force distribution at the bottom surface (optimized geometry).

4.7.9 Pressure distribution

The pressure distribution in the upper surface is the same for original geometry and optimized geometry. Figures Figure 4-79 and Figure 4-80 show that a high-pressure zone appear at the front bumper, which is an evidence of the existence of a stagnation point. In the hood the pressure starts negative and become positive close to the windshield, which is itself a high-pressure zone. Pressure distribution is predominantly negative at the roof changing gradually to zero at the rear end.

The same difference between original and optimized case seen before in the vertical force distribution is seen here. The implementation of rear diffuser creates a suction in car underneath doing the vertical force distribution assumes high negative values compared with original geometry. The peak of negative force happens in the rear diffuser inlet this increase the downforce improving the car performance. After this pressure reduces gradually until zero because the unsteady flow pattern a separation zone is formed.

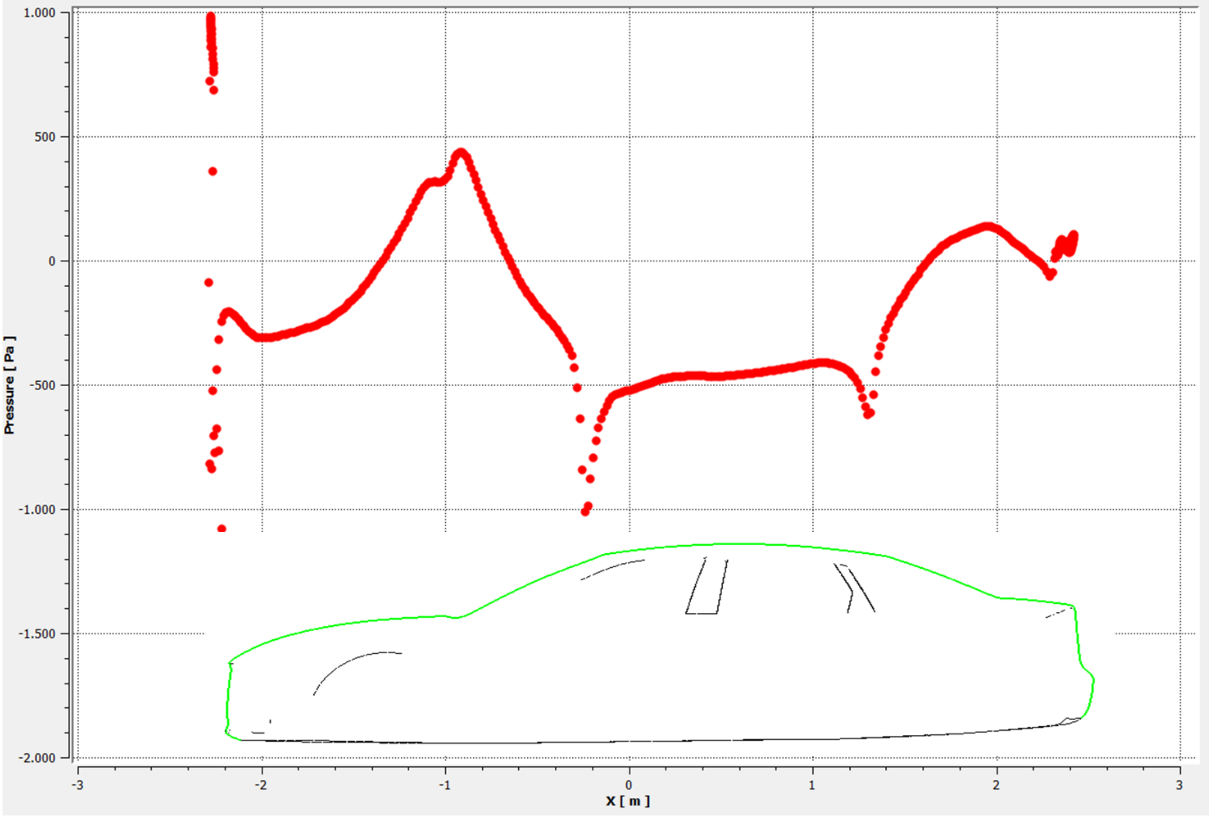

Figure 4-79 Pressure distribution at the upper surface (original geometry).

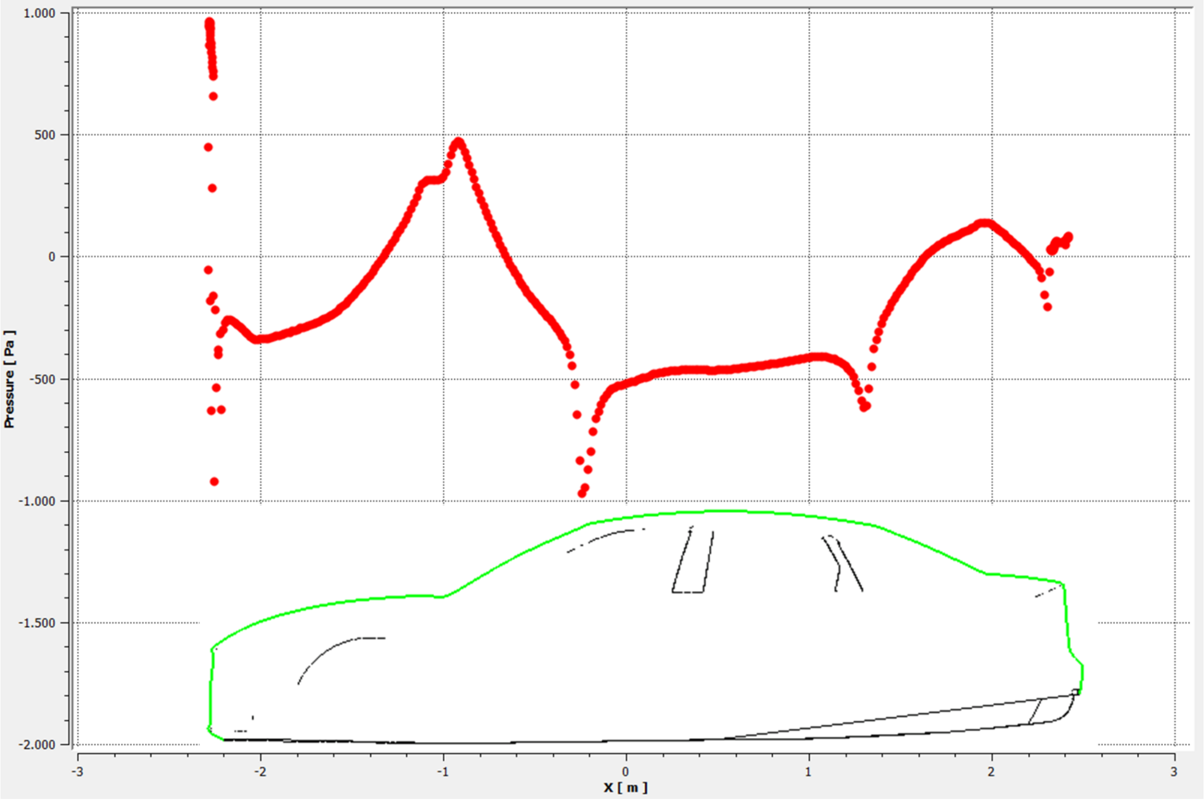

Figure 4-80 Pressure distribution at the upper surface (optimized geometry).

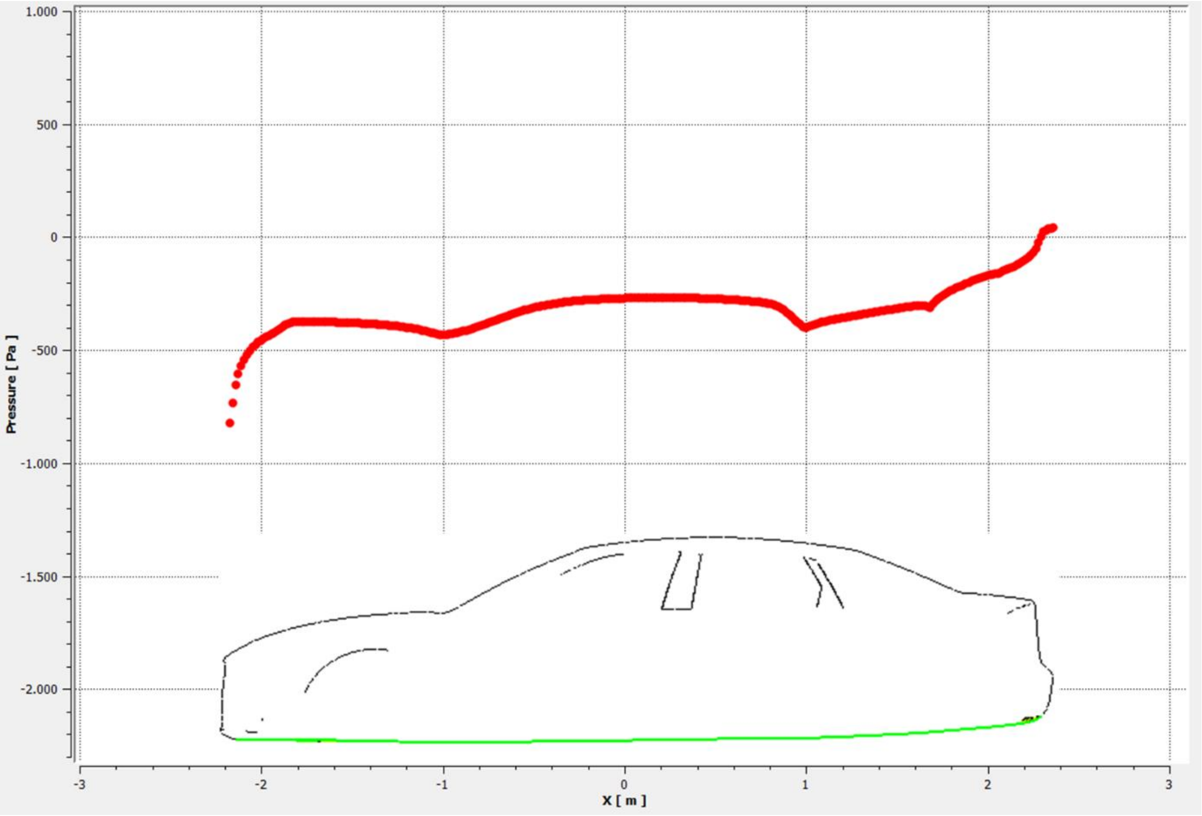

Figure 4-81 Pressure distribution at the bottom surface (original geometry).

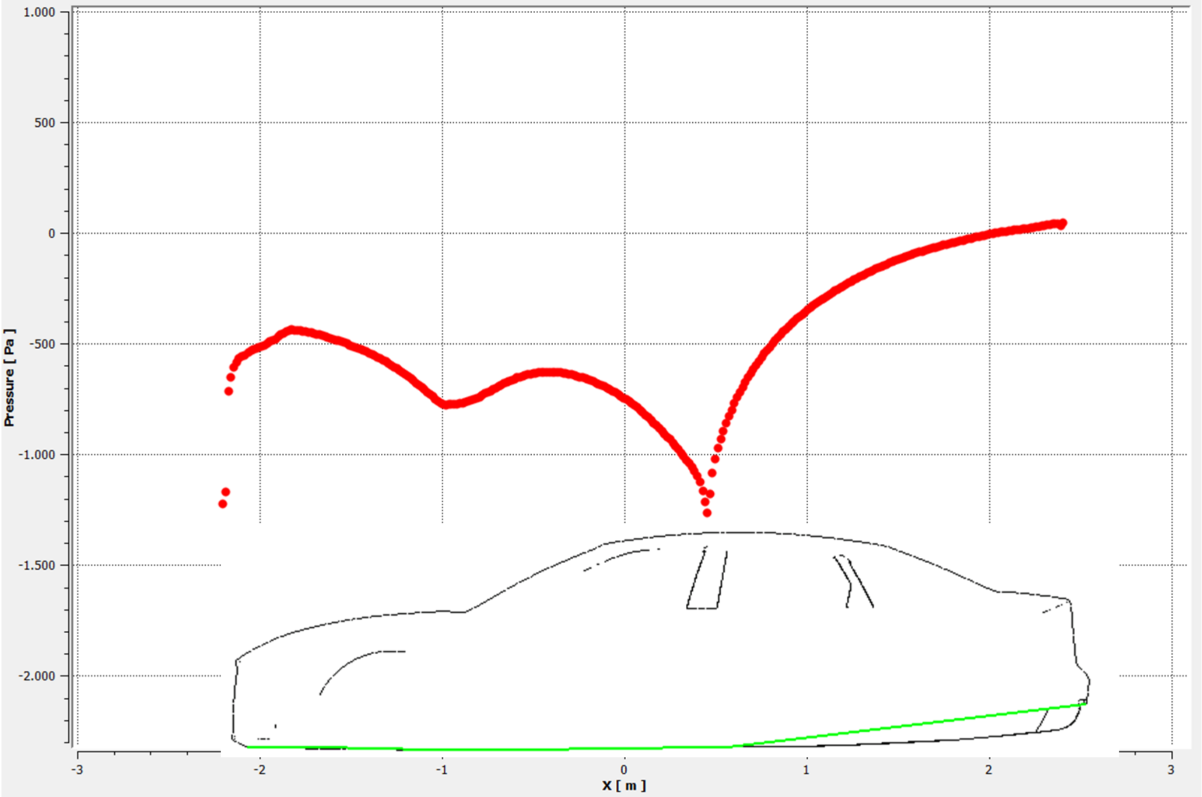

Figure 4-82 Pressure distribution at the bottom surface (optimized geometry).

4.7.10 Wall shear stress distribution

Like in the analysis of the Ahmed body, the wall shear stress distribution presents the same behaviour for both cases (Figure 4-83 and Figure 4-84). We can see four regions where the wall shear stress assumes values close to zero. These regions are the front bumper, the bottom part of the front windshield, the bottom part of the rear windshield and the rear end. All these zones present wall shear stress equal zero because the flow detaches from the surface at these points.

At the bottom surface, the wall shear stress distributions for the original and optimized geometry (Figure 4-85 and Figure 4-86) are completely different. For the optimized geometry the flow accelerates underneath the car due the rear diffuser. This increase in the flow velocity also increases the wall shear stress. After the diffuser inlet, the wall shear stress decreases gradually until zero. This happens because the flow detached from the rear diffuser surface. This behaviour contributes to the increase of drag.

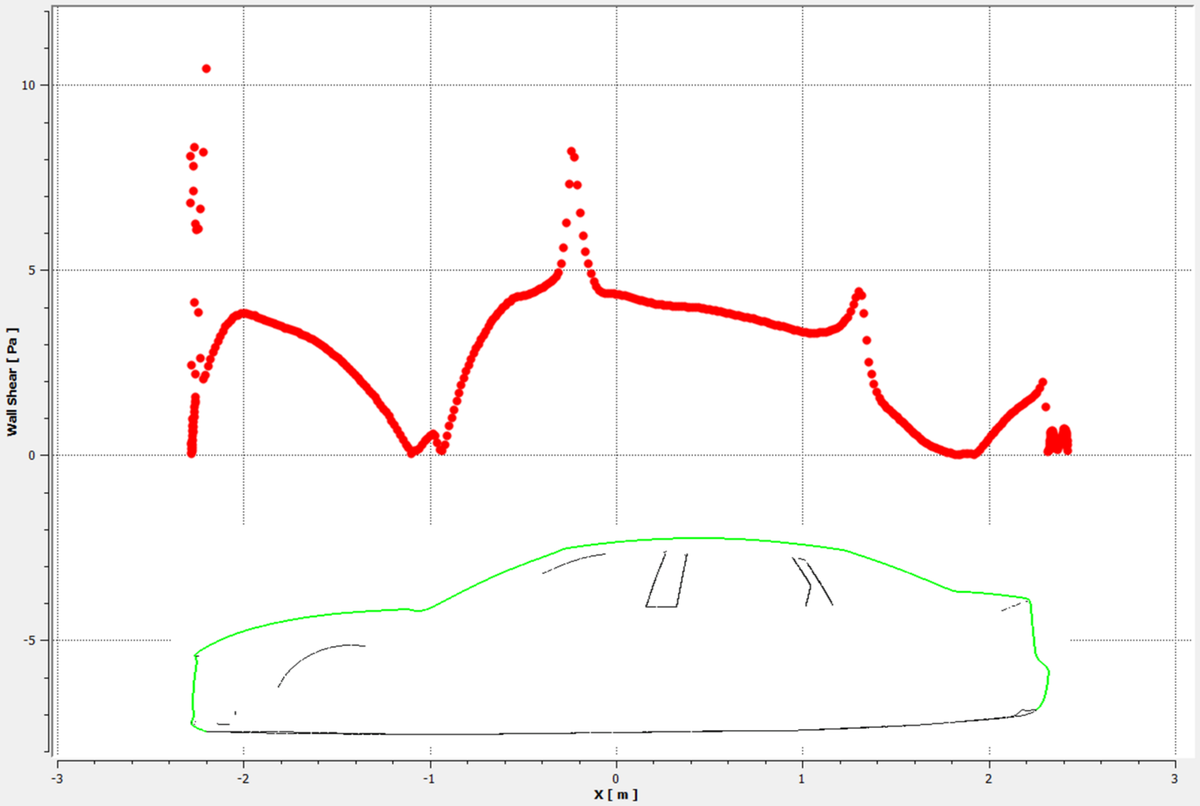

Figure 4-83 Wall shear stress distribution at the upper surface (original geometry).

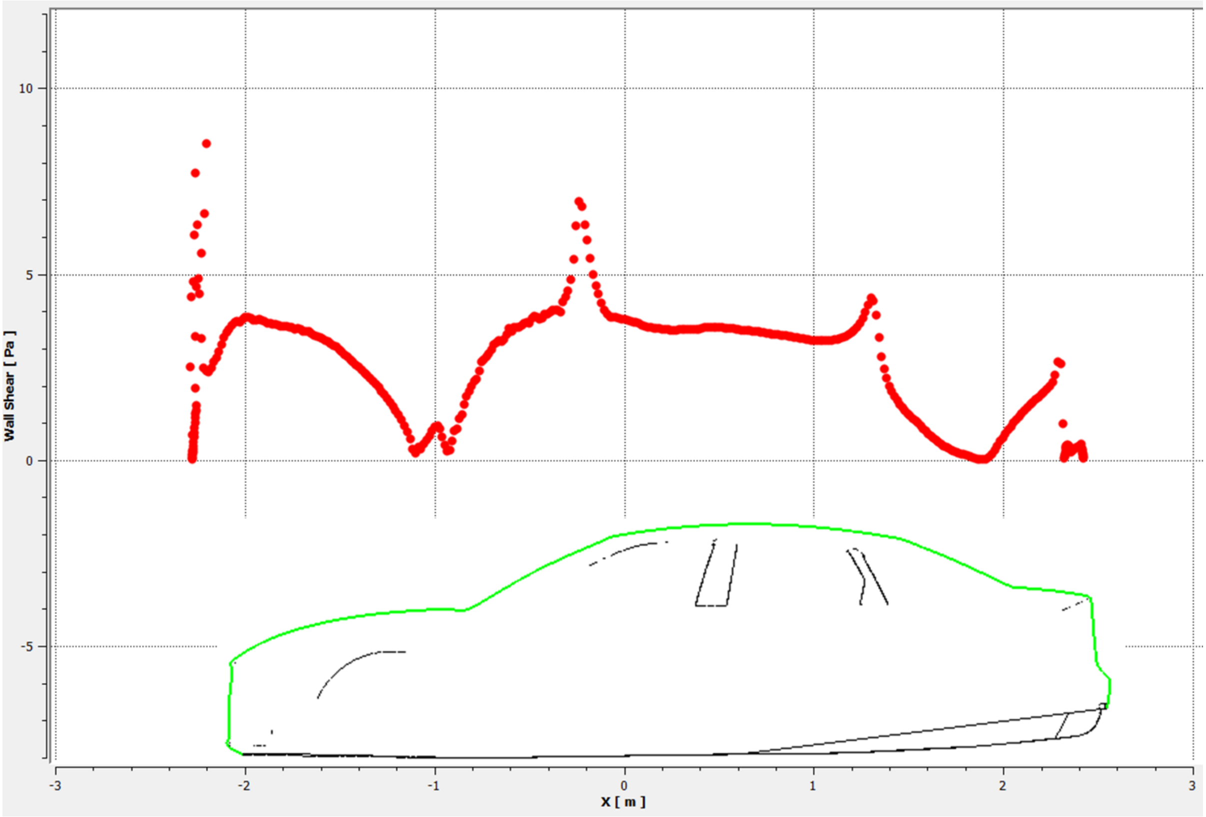

Figure 4-84 Wall shear stress distribution at the upper surface (optimized geometry).

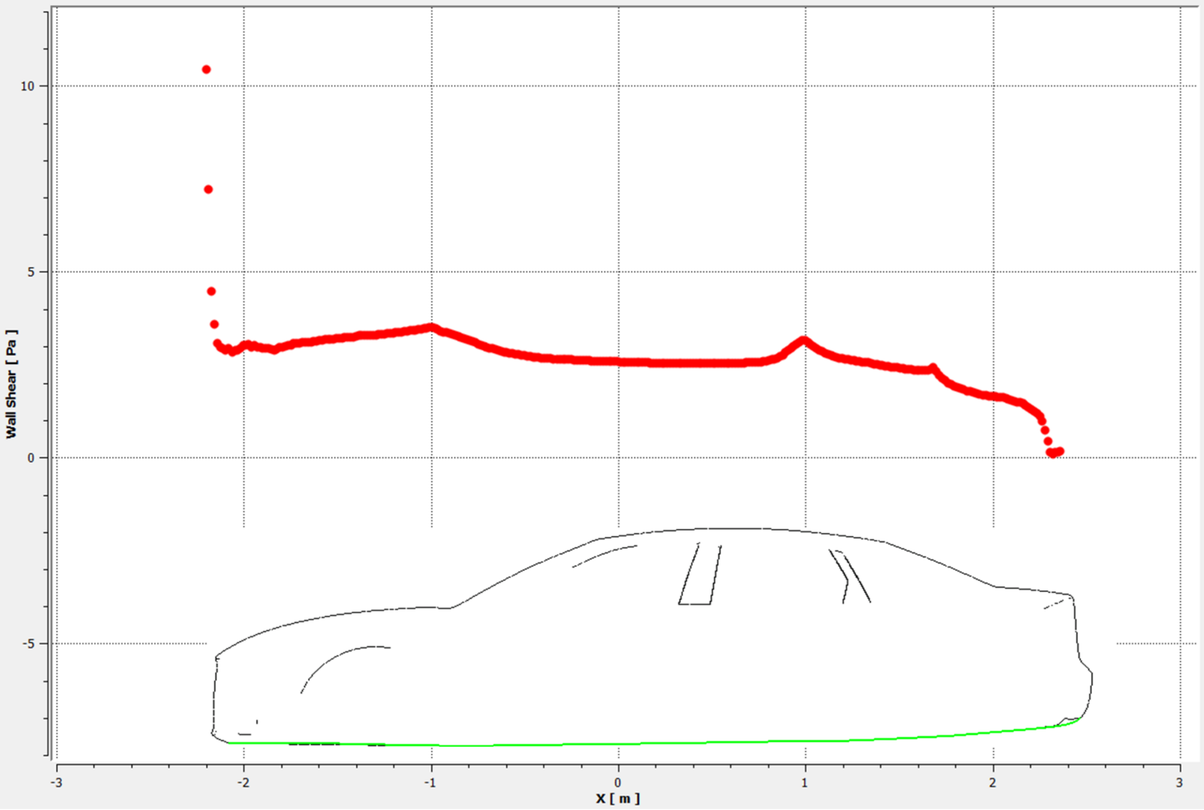

Figure 4-85 Wall shear stress distribution at the bottom surface (original geometry).

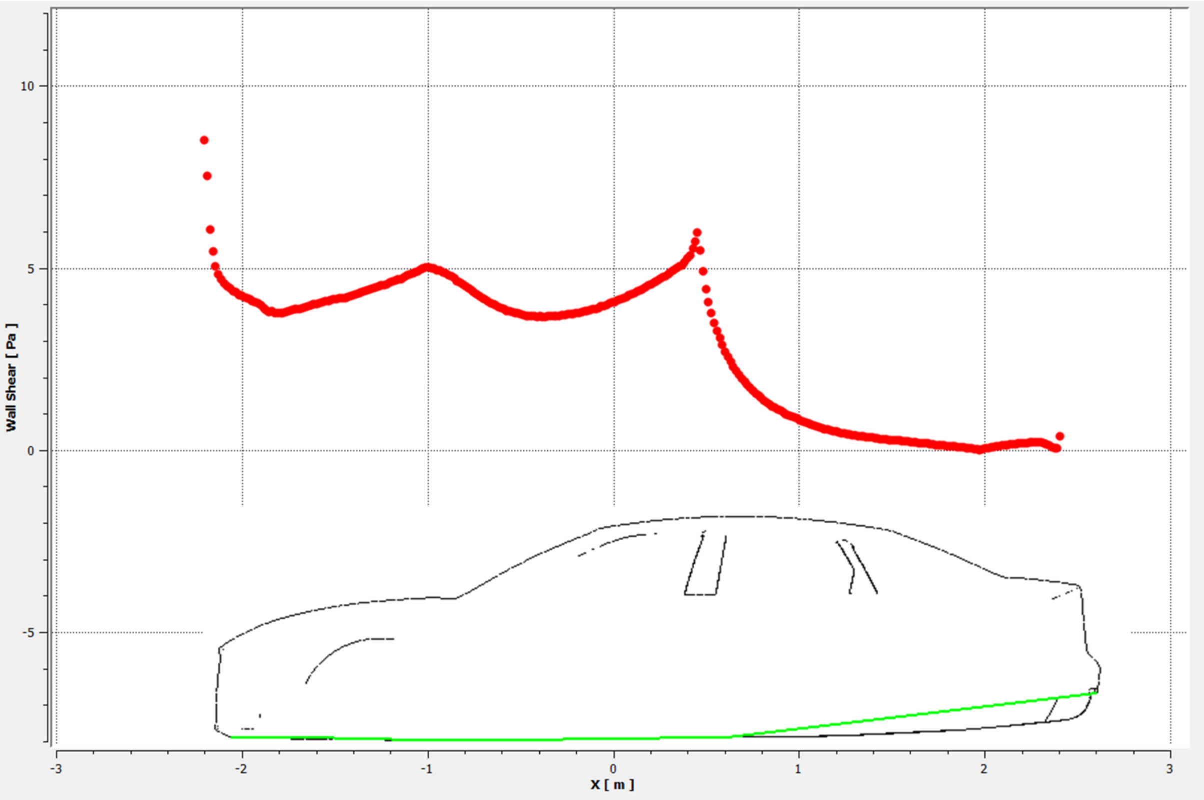

Figure 4-86 Wall shear stress distribution at the bottom surface (optimized geometry).

The charts presented before made it possible to understand the changes in the flow caused by the rear diffuser implementation. Table 4-9 presents some values of vertical and horizontal forces integrated along the upper and bottom surfaces of the original geometry and optimized geometry (rear diffuser). From this table it is possible to see the percentual difference of the values for both cases.

Table 4-9 Shows the force contribution for drag and lift at upper and bottom surfaces.

	Surface	Vertical force (N)	Horizontal force (N)
Original geometry	Top	857.37	103.15
	Bottom	-1437.58	34.91
	Total	-580.21	138.06
Optimized geometry	Top	842.16	85.14
	Bottom	-1966.70	75.38
	Total	-1124.54	160.52
% Difference		-94%	+16%

Finally, we can measure the changes caused by the rear diffuser implementation. It had a strong impact in the downforce, increasing the negative vertical force around 94%. However, it also increases the drag by 16% compared with the geometry without rear diffuser.

5 Conclusions

The purpose of this thesis was to develop knowledge in the field of high-performance automobile aerodynamic devices, in particular rear diffuser, which have crucial effects on vehicles performance. Such expertise was focused on the comparison of two different geometries, through a Multi Objective optimization integrated with a CFD-Simulation, developing an automated approach making the study fast and reliable.

Among the various ways of analysing race car aerodynamic efficiency presented (Track tests, wind tunnel and CFD), CFD was a great alternative in prediction of the race car aerodynamic, being fast, relatively cheap and presenting good accuracy. Also being completely virtual can be used at any stage of vehicle development.

The Ahmed body presented as a great alternative to aerodynamic analysis because it presents a relatively simple geometry compared to a race car but as it has main features involved in a vehicle flow such as: flow separations, vortex flows and boundary-layer transition.

From the studies performed in this thesis an of optimization considering MOO processes and CFD-Simulation for an optimal preliminary design was developed for a rear diffuser, but it can also be applied to any other automotive aerodynamic components. As in almost every high-performance vehicle manufacturer, the use of CAE tools proved to be an efficient simulation platform to assure the accuracy towards feasible products in a relatively short time frame. The MOO approach linked with optimization algorithms proved to be a fast and reliable alternative in search of the better solution, was notable the efficiency of RSM methods like FAST, since they use virtual optimization techniques, which decreases the number of simulations of low-quality individuals.

Based on the data presented in this research it was possible to see that aerodynamics analysis associated to race cars is a very complex task considering the concern with not only the reduction of drag but also the improvement of the negative lift. The generation of downforce and its effect on lateral stability has a major effect on race car performance, particularly when high-speed turns are involved. Ground effect elements are the most efficient in terms of lift / drag generated, providing expressive levels of downforce with minimal drag. Although the rear diffuser improves the overall downforce of the car, it also increases the drag. Nevertheless, the increase in drag coefficient was just 6% compared with original model, while the lift coefficient reduces 164%. The rear diffuser proved to be an efficient aerodynamic device in a way to improve the aerodynamic performance of a race car providing high levels of downforce adding a relatively low drag.

5.1 Future work

Regarding the complexity involved in a car CFD simulation, for future work we suggest performing some scale wind tunnel test to confront directly the numerical results with experimental results in order to validate the overall approach.

Another point for future research is to study more deeply the geometry of the rear diffuser. The results presented in this thesis showed some separations zones in the rear diffuser surface; one suggestion is to try to reduce these separation zones by implementing more vertical fins to keep the flow attached. It would be interesting to try more complex geometries for the rear diffuser like implementing a double angle, or a curved geometry.

Thinking about the overall car geometry, the same optimization loop approach used for rear diffuser can be used to improve another car device. Looking the contours of velocity, pressure, wall shear stress and etc, we can see other regions that can be possible candidates for optimization, like front and rear wind shield, front bumper, among others.

6 References

Ahmed, S.R., 1998. “Computational Fluid Dynamics”, Chapter XV in Hucho, W.H (Ed.), Aerodynamics of Road Vehicles, 4th Edition, SAE International, Warrendale, PA, USA.

Ahmed, S.R., Ramm, G., Faltin, G., 1984. “Some salient features of the time-averaged ground vehicle wake”, SAE Technical Paper 840300.

Aittokoski, T., and Miettinen, K., 2008. Efficient evolutionary method to approximate the Pareto optimal set in multiobjective optimization. EngOpt, 25(6), 1–10.

Aka, H., 2003. Study on Aerodynamic Characteristics of a Passenger Car in a Wind Tunnel. MSc Thesis, Gazi University, Ankara.

Alam, F., 2000. “The Effects of Car A-Pillar and Windshield Geometry and Yaw Angles on Local Flow and Noise”, Ph.D. Thesis, Department of Mechanical and Manufacturing Engineering, RMIT University, Melbourne, Australia.

Barnard, R. H., 1996 . Road vehicle aerodynamic design: An introduction. In R. H. Barnard, Road vehicle aerodynamic design: An introduction (pp. 264-265). St Albans: MechAero.

Casiraghi C., 2010. Race Car Aerodynamics, Royal Institute of Technology. http://www2.mech.kth.se/ courses/5C1211/Casiraghi.

Clarich A., Rigoni E., Poloni C., 2004. A new Algorithm based on Game Theory for Robust and Fast Multi-Objective Optimisation

Cooper, K. R. 1993. Bluff body aerodynamics as applied to vehicles. Journal of Wind Engineering and Industrial Aerodynamics, 49, pp. 1-22.

Cooper, K. R., Bertenyi, T., Dutil, G., Syms, J., and Sovran, G., 1998, “The Aerodynamic Performance of Automotive Underbody Diffusers,” Technical Report SAE Paper 98-0030, Society of Automotive Engineers, Warrendale, PA, USA

Cooper, K. R., Sovran, G., and Syms, J., 2000, “Selecting Automotive Diffusers to Maximise Underbody Downforce,” SAE Paper 2000-01-0354.

Coulliette C. and Plotkin A., 1995. Airfoil ground effect revisited. In 13th Applied Aerodynamics Conference.

Deb, K., Pratap, A., Agrawal, S., and Meyarivan, T., 2000. A Fast Elitist Non-Dominated Sorting Genetic Algorithm for Multi-Objective Optimization: NSGA-II, KanGAL Report No. 200001

Discetti S. and Ianiro A., 2017. Experimental Aerodynamics. CRC Press.

Dominy, R.G., 1992, “Aerodynamics of Grand Prix cars”, Proceedings of the institution of Mechanical Engineers, Part D: Journal of Automobile Engineering, 206:267-274.

Farabee, T.M., 1986. “An Experimental Investigation of Wall Pressure Fluctuations Beneath Non-Equilibrium Turbulent Flows”, Ph.D dissertation, The Catholic University of America, 1986, and/or David W. Taylor Naval Ship Research and Development Centre, Betheada, Maryland, USA.

Ferziger, J. H., 1999 “Computational methods for fluid dynamics.” Springer Verlag, March.

George, A. R., 1981, “Aerodynamic Effects of Shape Camber, Pitch, and Ground Proximity on Idealized Ground Vehicle Bodies,” ASME J. Fluids Eng., 103, pp. 631–638.

George, A. R., and Donis, J. E., 1983, “Flow Patterns, Pressures, and Forces on the Underside of Idealized Ground Effect Vehicles,” Proceedings of the ASME Fluids Engineering Division Symposium on Aerodynamics of Transportation-II, Vol. 7, pp. 69–79.

George, A.R.,1997. “Automotive Wind Noise and its Measurement”, An Information Report of the SAE Wind Noise Measurement Committee.

Gillieron, P., Samuel, S. and Chometon, F., "Potential of CFD in Analysis of Under-Bonnet Airflow Phenomena", SAE paper 1999-01-0802, 1999

Guilmineau, E., 2007. “Computational study of flow around a simplified car body”, Journal of Wind Engineering, and Industrial Aerodynamics, Vol. 96 (6-7), p. 1207-1217.

Hall, J., 2013. 'Ground Effect'. Its history and Theory explained. Retrieved 03 15, 2014, from The Judge 13

Happian-Smith, J.,2004. An introduction to Moden Vehicle Design. Warrendale: SAE

Houghton E. L. and Carpenter P. W., 2003. Aerodynamics for Engineering Students. Butterworth- Heinemann, 5th edition, 2003.

Hucho, W.H. 1998. “Aerodynamics of Road Vehicles”, 4th Edition, SAE International, Warrendale, PA, USA.

Kalyan, D. K., Paul, A. R., 2013. “Computational Study of Flow around a Simplified 2D Ahmed Body”, International Journal of Engineering Science and Innovative Technology, Vol. 2 (3), p. 148-153

Karim M. M., Rahman M. M. and Alim M. A., 2009, “Computation of Axisymmetric Turbulent Viscous Flow Around Sphere”, Journal of Scientific Research, vol. 1(2), pp. 209-219. mechanics. 25(1), 485-537.

Katz J. and Dykstra L., 1992. Effect of wing/body interaction on the aerodynamics of two generic racing cars. Technical Report 920349, SAE International, 1992.

Katz J. and Largman R., 1989. Experimental study of the aerodynamic interaction between an enclosedwheel racing-car and its rear wing. Journal of Fluids Engineering, 111(2):154–159.

Katz J., 1985. Calculation of the aerodynamic forces on automotive lifting surfaces. Journal of Fluids Engineering, 107(4):438–443.

Katz J., 1995. Race Car Aerodynamics: Designing for Speed. Bentley publishers.

Katz J., 2006. Aerodynamics of race cars. Annual Review of Fluid Mechanics, 38:27–63.

Katz J., 2016. Automotive Aerodynamics. Wiley.

Kiffer W., Moujaes S. and Armbya N., 2004. CFD study of section characteristics of Formula Mazda race car wings, Elsevier Ltd, Las Vegas.

Lanfrit, M., 2005. “Best practice guidelines for handling Automotive External Aerodynamics withFLUENT”.https://www.southampton.ac.uk/~nwb/lectures/GoodPracticeCFD/Articles/Ext_Aero_Best_Practice_Ver1_2.pdf

Lee S, Landman D, Jordan J, Watkins A, Leighty B, et al. 2002. Performance auto- motive applications of pressure-sensitive paint in the Langley full-scale tunnel. SAE 2002-01-3291

Liang, C. 2009, “Turbulent Flow Simulations Around The Front Wing of A Racing Car”, MSc THESIS, Cranfield University

Lis A. 2002. Buyers Guide,Wind Tunnels. Race Tech. 43(Aug./Sept.):75–78. Provides the world a comprehensive list + a short description of race car oriented wind tunnels in

Menter, F. R., 1994. “Two-equation eddy-viscosity turbulence models for engineering applications”, AIAA Journal, Vol 32 (8), p. 1598-1605.

Mokhtar W. A. and Lane J., 2008. Racecar Front Wing Aerodynamics, SAE International, Sault Ste Marie, Mi.

Mokhtar W. A., 2005. A Numerical Study of High-Lift Single Element Airfoils With Ground Effect For Racing Cars, SAE International, Norfolk, PA.

Morelli, A. 2000. A New Aerodynamic Approach to Advanced Automobile Basic Shapes. SAE Technical Paper 2000-01-0491.

Myose R., Papadakis M., and Heron I., 1998. Gurney flap experiments on airfoils, wings and reflection plane model. Journal of Aircraft, 35(2):206–211.

Nazar Baker, Ger Kelly & Paul D. O'Sullivan, 2019: A grid convergence index study of mesh style effect on the accuracy of the numerical results for an indoor airflow profile, International Journal of Ventilation.

Nye, Doug, 1985, Autocourse History of the Grand Prix car 1966 - 1985, Hazleton publishing, ISBN 0-905-138-37-6

Passmore, M. A. & Le Good, G. M., 1994 , "A Detailed Drag Study Using The Coast- Down Method", SAE paper 940420

Price T. A., 2011. 3D CFD on an Open Wheel Race Car Front wing in Ground Effect, California Polytechnic State University, San Luis Obispo.

Raghu, S., Heil, F. and Santamarina, A., 1999. "Windshield Spray Performance at High Vehicle Speeds", SAE paper 1999-01-0803,

Ranzenbach R. and Barlow J. B.,1994. Two-Dimensional Airfoil in Ground Effect, An Experimental and Computational Study, in Motorsport Engineering Conference Proceedings Vol. 1, SAE paper no. 942509, pp. 241-249.

Raymond, A.E., 1921, “Ground influence on aerofoils”, Technical Report, NACA- TN-67, NACA.
Rigoni E., Turco A., Montrone T., 2014. Technical Report 2014-001, FAST Optimizers: General Description.

Roache, P.J., 1998. Fundamentals of Computational Fluid Dynamics, Hermosa Publishers, Albuquerque, New Mexico.

Screbrinsky, Y.M. and Biachuev, S.A., 1946, “Wing tunnel investigation of the horizontal motion of a wing near the ground”, Technical Report NASA-TM-1095, NACA.

Senior, A. E., and Zhang, X., 2001, “The Force and Pressure of a Diffuser- Equipped Bluff Body in Ground Effect,” ASME J. Fluids Eng., 123_1_, pp. 105–111.

Sharma R. B. and Bansal R., 2013. Cfd simulation for flow over passenger car using tail plates for aerodynamic drag reduction. IOSR Journal of Mechanical and Civil Engineering, 7(5):28–35.

Tastan, Umur, 2011. Investigation of Turbulence Models Used in Automotive Industry. 134p. MSc Thesis Middle East Technical University.

Toet W., 2018. Race Tech Motorsport Engineering. Willem Toet Explains - Motorsport Diffusers. www.racetechmag.com/2017/08/willem-toet-explains-motorsport-diffusers/

Watkins, S., and Vino, G., 2008. The effect of vehcile spacing on the aerodynamics of a representative car shape. Journal of Wind Engineering and Industirial Aerodynamics 96, 1232-1239.

Wiedemann J., 1989. Some basic investigations into the principles of ground simulation techniques in automotive wind tunnels. Technical Report 890369, SAE International,

Wordley S. and Saunders J., 2006. Aerodynamics for formula sae: A numerical, wind tunnel and on-track study. Technical Report 2006-01-0808, SAE International.

Wright P., 2001. Formula 1 Technology. Premiere Series Books. Society of Automotive Engineers Inc. ISBN 978-0768002348

Zahm, A.F. and Bear, R.M., 1921, “Ground plane influence on airplane wings”, Journal of the Franklin Institute, pages 687-693, May 1921

Zerihan J. and Zhang X., 2000. Aerodynamics of a single element wing in ground effect. Journal of Aircraft, 37(6):1058–1064.

Zerihan, J. and Zhang, X., 2001, "A single element wing in ground effect - Comparisons of experiments and computation ", Aerospace Sciences Meeting and Exhibit, 39th, Reno, NV, Jan. 8-11

Zhan X. and Zerihan J., 2003. Aerodynamic of a Double-Element Wing in Ground Effect, AIAA Journal, pp. 1007-1016.

Zhang X., Toet W., and Zerihan J., 2006. Ground Effect Aerodynamics of Race Cars. Applied Mechanics Reviews, vol. 59, pp. 33-49.